Anisotropy of Arrival Direction of Primary Cosmic Rays from 10^14.8 to 10^18ev Observed at Akeno

Nishijima, Kyoshi

(Degree)
博士（理学）

(Date of Degree)
1986-11-28

(Date of Publication)
2014-03-12

(Resource Type)
doctoral thesis

(Report Number)
乙1048

(URL)
https://hdl.handle.net/20.500.14094/D2001048

神戸大学博士論文

ANISOTROPY OF ARRIVAL DIRECTION OF PRIMARY COSMIC RAYS FROM $10^{14.8}$ TO 10^{18} EV OBSERVED AT AKENO

昭和６１年８月

西嶋恭司

神 戸 大 学 博 士 論 文

ANISOTROPY OF ARRIVAL DIRECTION OF PRIMARY COSMIC RAYS FROM $10^{14.8}$ TO 10^{18} EV OBSERVED AT AKENO

（明野で観測された$10^{14.8}$から10^{18} eV領域の
一次宇宙線到来方向の非等方性）

昭和６１年８月

西 嶋 恭 司

ANISOTROPY OF ARRIVAL DIRECTION OF PRIMARY COSMIC RAYS FROM $10^{14.8}$ TO 10^{18} EV OBSERVED AT AKENO

by

Kyoshi Nishijima

Dissertation in Ph.D.
submitted to Kobe University

Institute for Cosmic Ray Research
University of Tokyo
August 1986

ABSTRACT

Anisotropies of arrival direction of primary cosmic rays in the energy range between 6×10^{14} eV and 10^{18} eV are studied with extensive air shower data observed at Akeno observatory from 1981 to 1984. The data are taken by various kind of triggering methods. Small air shower around 6×10^{14} eV is triggered by muon density and only event rate per hour is recorded. The others are that the data taking is triggered by electron density or by muon density, and output signals of density and timing from each detector are all recorded.

The harmonic analysis of counting rate in sidereal time is applied to each data set, and the following significant anisotropies are obtained; 1) the maximum phase of second harmonic is around 92° in right ascension in the energy of 6×10^{14} eV, 2) the maximum phase of the first harmonic is nearly constant with around 300° in right ascension in the energy region of 10^{15} - 10^{17} eV, and 3) for muon-poor showers, the result shows the significant anisotropy for second harmonic at phase around 166° in right ascension.

The above experimental results suggest the following possibilities; 1) for the energy of around several times 10^{14} eV, there is a cosmic ray flow along the local magnetic field near the solar system, 2) for the energy range of 10^{15} to 10^{17} eV, there is a cosmic ray flow along the large scale magnetic field which is parallel to the Galactic arm near the solar system.

In the energy region between 3.2×10^{15} and 1×10^{16} eV, the possibility of the contribution of heavy component whose origin may be different from proton is suggested from observed data by analyzing the muon-rich events.

CONTENTS

CHAPTER I . INTRODUCTION

Since the discovery of cosmic ray by Hess in 1912 (Hess 1912), there have been hitherto unresolved important and fundamental questions, that is, where the cosmic rays originate, where and how they are accelerated, and how they propagate.

The principal ones of many observable quantities which give us important clues to solve those questions are primary composition, isotopic abundance ratio, energy spectrum, arrival direction distribution, and so on. Many efforts to know the cosmic ray origin by using these information have been paid in each energy region for a long time.

In the energy region below about 10^{11} eV, direct observations of primary cosmic rays by balloon and satellite experiments have been revealing the charge composition. Primary charge composition conveys the information of nucleosynthesis, which is essential for establishing the origin of cosmic rays. And more recently, observations of isotopic abundance ratio are also extensively carried on, which gives the information about the time for their acceleration or history of their propagation in the interstellar magnetic field. Their results provide active discussions on the low energy cosmic ray's origin, acceleration and propagation (see, for example Simpson 1983).

Furthermore, in the energy range of 10^{11} eV to 10^{14} eV, the direct observation using balloon-born detectors is carried on and new data of charge composition and their energy spectrum are reported by JACEE group (Burnett et al.1984), which show no change of them up to 1×10^{14} eV/nucleus. Considering the fact that the measured energy is getting to overlap small air shower (SAS) region, further developed experiments are very desirable for verification of indirect observations.

On the other hand, in the energy region above 10^{14} eV, because of very low intensity of cosmic rays, it is difficult to directly detect primary cosmic rays. The available method is to estimate primary composition and its energy indirectly by observing the Extensive Air Shower (EAS). Since the EAS suffers from a number of interactions before arriving at the observational level, the information of characteristics of primary cosmic rays is weakened and sometimes almost lost at the ground level. Therefore the results for the primary composition derived by this method are not very conclusive. Instead we can approach the problem of cosmic ray origin by use of the information of arrival direction in this energy region. It will be mentioned latter.

In very high energy region above 10^{18} eV, to be called Giant Air Shower (GAS), the problem of cosmic ray origin is simpler than the lower energy regions. Here the energy spectrum is very important. If the strength of magnetic field of about 3 μ Gauss near the solar system which recently becomes confirmative (Verschuur 1979) can be applied to the whole our Galaxy, the Larmor radius of proton with energy of 10^{19} eV is about 3 kpc which is the same order of dimension of the Galaxy and it cannot be confined in the Galaxy. Therefore if cosmic rays of this energy region are protons, it is natural to presume that they are of extragalactic origin. If the sources locate further than about 30 Mpc, cosmic ray particles are absorbed by pionization interaction with cosmic back ground photons (Greisen 1966). So by knowing whether the cut off of energy spectrum at above 10^{19} eV is seen or not, we can tell whether the distances of cosmic ray sources are beyond about 30 Mpc or not. Otherwise, if cosmic rays of GAS region are Galactic origin, it must be heavy particles or the magnetic field in the Galactic halo must be very strong. But even the world wide data are not sufficient to tell about these problems.

Notwithstanding the many attempts mentioned above. we have not reached our goal yet. The major cause for difficulty of resolving such problems is that because cosmic rays are generally charged particles the trajectories of them are bent by interstellar magnetic fields and we cannot say the direction of their origins definitely. The Larmor radius ρ (cm) for cosmic ray particle moving in the uniform magnetic field of strength H (Gauss) is given by

$$\rho = pc / (300HZ), \qquad (1)$$

where p is the momentum of particle in eV/c and c (cm s^{-1}) the light velocity and Z the charge of cosmic ray. For example, the strength of the magnetic field in the interstellar space is usually taken as about 3 μ Gauss (Verschuur 1979), so the Larmor radius for proton is about 3×10^{-5} pc for 10^{11} eV and 0.3 pc for 10^{15} eV. Since the thickness of Galactic disk is estimated to be smaller than 1 kpc, the arrival direction of cosmic rays in these energy region is strongly influenced by Galactic magnetic field. This makes it difficult to infer the place of the origin from the arrival direction of <u>each</u> cosmic ray. The energy of cosmic rays whose arrival directions point directly to their origin is estimated to be greater than 10^{19} eV.

However, even in the energy region from 10^{14} to 10^{18} eV, We can get the information of the origin and propagation of cosmic rays by searching the anisotropy of cosmic rays, that is, the direction of <u>average flow</u> in the space. The arrival direction is basically related to the distribution of cosmic ray sources and the structure of Galactic magnetic field through which cosmic ray propagates. So the information of average aspect of arrival direction of them may be expected to give us the clues of not only the origin of cosmic rays but also the structure of Galactic magnetic field.

As one of the method to approach the cosmic ray origin, many efforts have been paid on this subject for many years. Nevertheless the data of anisotropy of arrival direction has not been very reliable. The difficulty of getting significant data for anisotropy for EAS region is caused mainly from the reasons that the expected amplitude of anisotropy is as low as 0.5 % at 10^{15} eV and 5 % at 10^{17} eV and that the flux of EAS is also very small and then the statistics are inevitably poor. Therefore it is also required to observe EAS with high triggering rate.

Considering the above situations, we have observed arrival direction of cosmic rays and analyze the data with the following distinctive features:

1) We make researches on the energy dependence of anisotropy over the wide energy range of several times 10^{14} eV to 10^{18} eV by an apparatus.

2) Using the trigger by muons which are insensitive to the variation of atmospheric pressure and the fluctuation of the longitudinal development of EAS, we observe the anisotropy of SAS region (6×10^{14} eV) where reliable observation is generally difficult. Moreover, our muon detectors (proportional counters) are more insensitive to temperature variation than the electron detectors (plastic scintillators).

3) For the energy above 10^{15} eV, we observe EAS by muon trigger as well as electron trigger which is widely used. The reason why we use muon trigger, in addition to those mentioned above, is that even EAS of large electron size have wide distribution of muon contents and therefore we check the effect for anisotropies by the different triggering method.

Furthermore, we analyze the data selected by muon contents to study the anisotropy in relation to the composition. The propagation in the magnetic field is a function of rigidity as

shown in equation (1). Therefore the distribution of arrival direction is probably different for each component of cosmic ray composition at the same energy, even if their origins are common. Alternatively, if the structure of magnetic field in the Galaxy is given, we may be able to know whether the origins of each component are the same or not. Thus the measurement of anisotropy as a function of composition can give interesting information on cosmic ray origin.

In connection with above mentions, there is the following interesting topic. It is well known that the cosmic ray spectrum has a kink near 10^{15} eV from the data of EAS (e.g. Nagano et al.1984). And being combined to the lower energy data obtained by direct observations, there appears to the enhancement of cosmic ray intensity around such energy region (e.g. Hillas 1984). At first, Karakula et al.(1974) explained such bump in terms of proton contribution accelerated by pulsar. Unfortunately recent observations of EAS have not yet succeeded to reveal composition in that energy region. But recently, Takahashi et al.(1986), using new data of JACEE (Burnett et al. 1984) and HEAO-3 (Jones et al. 1985), report that the bump of the spectrum is due to Calcium and pulsars in type II supernova remnants are the origin of this component. If it is true, we ought to be able to catch the indication of it by analyzing anisotropy as a function of composition.

So, we also analyze the data in this point of view. That is, the fourth distinctive feature of our present work is as follows:

4) By selecting the events in accordance with the ratio of muon and electron contents, we research the difference of anisotropies among each component.

Now, if a considerable part of anisotropy is due to ultra high energy (UHE $> 10^{14}$ eV) gamma-rays (Wdowczyk and Wolfendale 1983), it reflects directly the distribution of energetic gamma-rays, for example, created from the

interaction of cosmic ray with interstellar matter through the π^0-decay process (i.e., $p + p \rightarrow \pi^0 \rightarrow 2\gamma$). Such observation, with the astrophysical quantities, gives us the information about the distribution of cosmic ray particles. Recently many groups including ours report the detection of UHE gamma-rays from point sources such as Cyg X-3 (Samorski and Stamm 1983; Lloyd-Evans et al. 1983; Kifune et al. 1986a and so on). There might be many other point sources of UHE gamma-rays like Cyg X-3 and they might contribute to the observed anisotropies. But here we do not treat the data in such point of view.

It is noted that the point sources can be very important as the place of acceleration of cosmic ray particles, but such approach to cosmic ray origin is not treated here.

In this article, We present the data of arrival direction of cosmic rays in the energy range from 6×10^{14} eV to about 10^{18} eV observed at Akeno observatory by various triggering conditions which include the high rate trigger at SAS region as well as the ordinary EAS trigger.

First of all, the world wide data on anisotropy are briefly reviewed in chapter II, and some possibilities of anisotropy expected from some astrophysically plausible models are shown in chapter III. In chapter IV, brief description of the Akeno EAS array is given, and the details of the method of observation and procedure of data reduction for each trigger are presented in chapters V and VI. Atmospheric effects of trigger rate are discussed in chapter VII. The results of the analysis for anisotropy with EAS are shown mainly for the equatorial coordinate in chapters VIII and IX. In chapter X, we compare presented results with other experiments and discuss the interpretation of our results and the origin and propagation of cosmic rays. Conclusion is presented in chapter XI.

CHAPTER Ⅱ . REVIEW OF OBSERVATIONS OF ANISOTROPY

Ⅱ -1. General Remarks

The cosmic ray flow can be observed with sidereal time variation of cosmic ray intensity as the earth rotates on its axis, except for the case that the direction of maximum intensity of cosmic ray is coincide with the axis of rotation. Almost all the experiments use this earth's rotation and therefore the most observed data are analyzed in terms of their harmonics for sidereal time or right ascension. The principal results of them are summarized in Fig.1 and Fig.2, where projected amplitudes on the equatorial plane are displayed. The method of harmonic analysis is briefly described in Appendix A.

However, it must be noted here that observed harmonic component of flux variation for sidereal time or right ascension at fixed geographic latitude gives only limited information about a projected component of anisotropy in the equatorial plane and cannot give complete spatial distribution of it. Nagashima (1971) represents an expression of observed sidereal intensity distribution from three dimensional cosmic ray anisotropy for which axial symmetry is supposed and is described roughly in Appendix B.

Ⅱ -2. In the Energy Range below 10^{14} eV

A summary in this energy region until 1979 is presented by Elliot (1979). Adding recent results to it, the experiments for anisotropy of cosmic ray intensity at low energy are reviewed in what follows.

In the lower energy around 10^{12} eV, the anisotropy of arrival direction is studied by observing high energy muons

with under-ground muon telescope. Muons are created by interaction of cosmic rays with the air nuclei through π -μ -decay. Some groups such as Holborn (Davies et al. 1979), Hong Kong (Lee et al. 1985), Utah (Cutler et al. 1981), Poatina (Fenton and Fenton 1976) and Ottawa (Bercovitch and Agrawal 1981) report the results of harmonic analysis for arrival direction of muons with energy of about 10 GeV to 100 GeV which correspond to the primary energy of $(0.5 \sim 1.5) \times 10^{12}$ eV.

As shown in Fig.1, observed amplitudes for first harmonic are as large as 0.06 %, which are in good agreement with each other except for Ottawa group. The maximum phases are also very consistent with each other, about $40^\circ \sim 60^\circ$ in right ascension (R.A.). For second harmonic, Utah group and Hong Kong group report the amplitude of less than 0.1 %, however the other groups report no significant anisotropies and only upper limits are obtained, where inconsistency arises among each results.

In the energy range of $10^{13} \sim 10^{14}$ eV, the anisotropy is studied by the observation of counting rate of SAS constantly at the mountain altitude.

Norikura group has continued to observe SAS in this energy region since 1972, by use of a part of 36 m^2 meson telescope consisting of two layers of scintillation counters at Mt. Norikura (at 2770 m above sea level). Their harmonic analysis gives the results that the amplitude of first harmonic is 0.053 $\pm$ 0.003 % at the maximum phase of $14^\circ \pm 8^\circ$ in R.A., and 0.026 $\pm$ 0.003 % with $87^\circ \pm 5^\circ$ for second harmonic (Sakakibara et al. 1979). This result of first harmonic is consistent with Poatina's one observed at southern hemisphere in a slight lower energy region, which indicates that the contribution of function f_2^1 (see appendix B) is negligibly small compared with f_1^1. Then, the second harmonic phase of maximum flux is expected around 90° in R.A. at the equatorial plane and the

results of Holbone group support this expectation.

Baksan group has observed SAS with Baksan EAS array which consists of 400 liquid scintillators array with area of 200 m^2 and six 9.9 m^2 detectors containing scintilator and Geiger-Muler (G-M) counter. The data of Baksan in the energy region of $10^{13} \sim 10^{14}$ eV (Alexeenko and Navarra 1985) show the good agreement with that derived by Norikura group.

Gombosi et al.(1975) at Peak Musala and Morello et al.(1983) at Plateau Rosa also observe in this energy region, the results of which are almost consistent with ones of Norikura group and Baksan group especially for maximum phase.

Consistency of each group in this energy range is very well and the reliability seems high enough. So the experimental results from 10^{11} eV to 10^{14} eV are summarized as follows.

1) For the first harmonic, the amplitude is about $0.04 \sim 0.06$ %, which is almost constant through the energy range of two decades. Its phase of maximum intensity is $40^\circ \sim 60^\circ$ in R.A. around 10^{12} eV and about $10^\circ \sim 20^\circ$ at $10^{13} \sim 10^{14}$ eV.
2) For the second harmonic, significant anisotropy cannot be seen around 10^{12} eV. At the energy of 10^{13} eV level, the amplitude is nearly constant with about $0.02 \sim 0.03$ % and the peak phase seems to be around 90° , however their reliability is rather lower than the first one.

II -3. In the Energy Range from 10^{14} eV to 10^{18} eV

As the review of the results of observations about the anisotropy of primary cosmic ray in this energy region, there are two preceding papers, one of which is by Sakakibara (1965) containing the experiments before the year of 1965 and another is by Linsley and Watson (1977) treating the data obtained between 1951 and 1965.

Daudin et al.(1956) observed the anisotropy of arrival

direction of cosmic ray from 1952 to 1954 by use of EAS array at Pic du Midi (at 2860 m above sea level). They record the counting rate of EAS acquired by four kinds of trigger conditions whose energy range is estimated as 3×10^{14} eV to 4×10^{15} eV. The results of harmonic analysis show that the amplitude of first harmonic is about $0.1 \sim 0.2$ % and seems slightly increasing with energy and the maximum phase is about $300^\circ \sim 330^\circ$ with no large change. For the second harmonic, they obtained the amplitude of about 0.1 % with the characteristic features of phase changing from 80° to 120° in R.A. continuously with energy.

In the same energy region, Cornell University group (Delvaille et al. 1959; 1962) also observed EAS by multiple coincidence between scintillators at spacing of 10 m to 100 m. They show almost three times larger amplitude than Daudin et al. for the first harmonic, and for the second harmonic they report no significant anisotropy. Murakami et al.(1985) report the significant second harmonic amplitude of 0.37 ± 0.10 % with phase of $86^\circ \pm 12^\circ$ in R.A. at the median primary energy of 3×10^{15} eV, which is roughly consistent with others. They record only the counting rate triggered by four muon stations of 25 m^2 separated about 100 m each at Akeno Observatory. The amplitude and phase of first harmonic are also consistent with the results of Pic du Midi group. Haverah Park group (Lloyd-Evans 1982) obtains only the upper limit for 3×10^{15} eV which is not inconsistent with others.

In the energy region around 10^{16} eV, Cornell group and Haverah Park group mainly contribute at the northern hemisphere, but both results give only the upper limit for the amplitude of both first and second harmonics. Our Akeno group also reports the results from the data of two years observation (Kifune et al.1986b). Our previous results show a significant second harmonic amplitude of 1.1 ± 0.4 % in the energy range 10^{16} eV to 10^{17} eV with the phase of $109^\circ \pm 10^\circ$.

At the southern hemisphere, Adelaide group reports the anisotropy with the amplitude of 0.84± 0.4 % and the phase of 120° ± 29° whose phase changes appreciably at about 10^{16} eV (Gerhardy and Clay 1983).

The anisotropies at the energy region around 10^{17} eV are reported by Cornell, Chacaltaya (Kaneko et al. 1985), Haverah Park, Yakutsk groups (Efimov et al. 1983) and so on. The amplitude of first harmonic is about 1 ~ 3 % with no clear energy dependence, and the maximum phase seems to change rapidly from 200° to 360° with energy in a decade at the level of 10^{17} eV. However consistency among each group is not good for both amplitude and phase. For the second harmonic, the most probable amplitude is about 1 ~ 2 %, but the error is large and some data give only the upper limit. Maximum phases are seen around 60° but are not so good agreement. At the latter half of 10^{17} eV level, Yakutsk group reports a high amplitude of about 6 ~ 7 %, and Chacaltaya and Haverah Park group report only the upper limits of 2 ~ 3 % amplitude.

Summarizing the results of harmonic analysis for energy region of 10^{14} eV to 10^{18} eV, there is no definite evidence of anisotropy far beyond the statistical error and the consistency among each group is also not so good. However following tendencies are read from Figs 1 and 2.

1) For the first harmonic, the amplitude increases roughly with energy. The maximum phase is around 300° below 10^{16} eV and above it the phase seems to change rapidly with energy.
2) For the second harmonic, the significance of anisotropy is lower. But the energy dependence of amplitude shows the same character with one for the first harmonic. Reported maximum phases seem to gather around 100° below 10^{16} eV, near 60° at around 10^{17} eV and 150° around 10^{18} eV.

However the above tendencies are not very clear. Therefore it is very important and necessary to observe cosmic ray anisotropies in this energy region in the further studies to

confirm the reported results.

II -4. In the Energy Range above 10^{18} eV

Above 10^{18} eV, Haverah Park (Edge et al. 1978; Eames et al. 1985), Utah (Baltrusaitis et al. 1985a) and Yakutsk group report the results of harmonic analysis which seem to show non zero anisotropy, but the statistics are very poor.

Above 3.2×10^{19} eV, Haverah Park group reports there is some evidence for anisotropy in direction normal to the Galactic plane. This result is consistent with Yakutsk one which shows that most high energy particles more than 3.5×10^{19} eV arrive from the virgo supercluster within the 45° cone. These results may imply the possibility of extragalactic origin of cosmic ray having the highest energy of GAS region, which, if it is true, is very interesting in astrophysical prospect.

II -5. Results by Selecting the Composition of Cosmic Rays

Attempts to analyze anisotropy by picking up cosmic rays biased toward heavy components have been done by some authors such as Hasegawa et al.(1962), Chatterjee et al.(1968), Blake et al.(1975), and recently Akeno group (Kifune et al.1986b). It is not possible to distinguish each primary component completely by observing air showers at ground, but it can be made rough distinction whether the primary component is heavy nucleus or light one; for example, by using the N_μ / N_e ratio as criterion (in case of ours) or by muon density (in case of others).

Our previous results show that the phase of muon-rich showers selected by N_μ / N_e larger than 0.06 is around 230° below several times 10^{16} eV. However, other groups report that there is an excess flux between 90° and 225° in the phase of

R.A. and negative excess between 225° and 315° . These results are not consistent with our previous one.

On the other hand, attempts to find evidence of UHE gamma-ray in the primary cosmic rays have been made by selecting the muon poor showers or some times old-aged showers. For example, Kamata et al.(1963) reported the results of such analysis of the data acquired at Mt.Chacaltaya and showed that the peak of the flux of muon poor shower is in the interval of 200° and 220° in R.A.; 27 events are observed against the expected back ground of 13.8 events. From those data, they also obtained the upper limit of gamma-ray intensity from the Galactic plane and isotropic gamma-ray background for above 3×10^{13} eV.

More recently Samorski and Stamm (1983) have found the evidence of UHE gamma-ray coming from Cyg X-3 which is the well known X-ray point source and considered to be a close binary system including a neutron star. They analyze the flux modulation synchronized with the X-ray intensity periodicity of 4.8 hours and obtain 4.4σ excess at the phase 0.3. The evidence from other point sources is also reported; such as Vela X-1 (Protheroe et al. 1984), Crab pulsar (or nebula) (Dzikowski et al. 1983; Boone et al. 1984), Her X-1 (Baltrusaitis et al. 1985b) and so on (e.g., Protheroe and Clay 1985). The detection of such UHE gamma-rays gives us very important information for not only the mechanism of its radiation but also the evolution and circumstances of the neutron star belonging to close binary system. However, at present, there exist some discrepancies in the experiments with each other. Further checks are undoubtedly necessary.

CHAPTER Ⅲ. REVIEW OF THE ATTEMPTS TO INTERPRET OBSERVED ANISOTROPY

Ⅲ-1. Location of the Solar System

Our Galaxy is considered to be an ordinary spiral galaxy and the radius is about 15 kpc. It consists of the Galactic disk with scale height of about several hundreds pc, where stars, gas and dusts gather closely, and the Galactic halo with height of the order of 10 kpc.

Our solar system locates in the Galactic plane (more exactly it is about 8 pc north to the plane) at near the Galactic center side edge of Orion arm. The arm is considered to be located by open cluster, O associations, HII regions, and interstellar absorption.

For quantitative details of our Galaxy, see the summary by Allen (1973).

By the results of RM (Rotation Measure) of radio sources, the Galactic magnetic field appears to direct toward $l = 45^\circ \sim 50^\circ$, $b = 0^\circ$ within 300 pc to 500 pc from the solar system and beyond 500 pc it appears in the direction toward $l = 90^\circ$, $b = 0^\circ$, and the mean strength of the field is about 3 μ Gauss (see review by Verschuur 1979), where l and b are the Galactic longitude and the Galactic latitude respectively. Schematic model for magnetic field near the solar system is shown in Fig.3.

Ⅲ-2. Expected Anisotropies

In order to interpret the observed anisotropies, expected ones have been calculated by many authors. In Fig.4, the energy dependences of amplitude of anisotropy calculated by some models are shown, and the possible directions expected

from the structure of the Galaxy and the spiral arm are presented in Fig.5. What kind of anisotropies can be expected is summarized below.

a) Compton-Getting effect

Compton-Getting effect (C-G effect; Compton and Getting 1935) is the phenomena that the dominant cosmic ray flux can be seen from the direction toward which the solar system moves relative to the space confining the cosmic rays. The amplitude of C-G effect is given by

$$r_{C\text{-}G} = (\gamma + 2) \times |v| / c, \qquad (2)$$

where γ is the absolute value of power of differential energy spectrum of cosmic ray, v is the relative velocity of solar system and c is the light velocity. As can be seen from equation (2), this effect gives rise to the energy independent anisotropy if the confinement space of cosmic ray does not change as a function of energy.

There are some possible peculiar motions of solar system. The velocities of these motions and the expected amplitudes and phases of anisotropies caused by this effect are summarized in Table 1.

If cosmic ray is of the extragalactic origin as suggested by Brecher and Burbidge (1972), the anisotropy arising from the combined motion of solar system relative to universal micro wave back ground radiation must be observed. As presented in Table 1, the resultant direction of motion is toward α = 165° and δ = +6° with velocity of 390 km s^{-1}, which gives rise to the upper limit of the anisotropy of 0.65 % for first harmonic, where α is right ascension and δ is declination in equatorial coordinate.

b) Expected anisotropies related to the arm structure

Davis (1954) pointed out two types of anisotropies a long time ago. One is an axial symmetric anisotropy. Assuming that magnetic field is approximately parallel and constant, cosmic ray particles move helically along the field line with some pitch angle distribution. So it gives rise to the axial symmetric anisotropy of flux parallel to the direction of magnetic field. The direction of large scale magnetic field near the solar system is as described in the above section. Therefore, for the cosmic ray whose Larmor radius is enough smaller than the radius of Galactic arm of about 500 pc, The anisotropy is expected around the direction of

$$\alpha = 315^\circ \ , \ \delta = +45^\circ \qquad \text{(Spiral In)},$$

and/or

$$\alpha = 135^\circ \ , \ \delta = -45^\circ \qquad \text{(Spiral Out)}$$

in equatorial coordinate. For example, when the sources of cosmic rays exist in the direction of spiral in (SI), the maximum phase of flux is expected from SI. When cosmic rays are accelerated uniformly in the Galactic arm, the flux is expected to be the maximum in direction of both SI and SO (spiral out). When the pitch angles of cosmic rays are small or the magnetic field open, such as, toward SO, cosmic rays are easy to escape such direction of field line. So the intensity of cosmic ray from its direction is rather lower and we can observe it as a 'hole'. This is the anisotropy of loss cone type.

Another expected anisotropy is due to the density gradient of cosmic ray particles whose direction is perpendicular to the Galactic plane. For simplicity, the projection to the cross section perpendicular to the magnetic field is considered. As it is evident from Fig.6, the maximum of cosmic ray flux is expected toward the direction of

$$B \times \nabla n,$$

where B is the Galactic magnetic field, n the density of cosmic ray. As our solar system locates at the Galactic center side edge of Orion arm. if the density of cosmic rays is the highest at the center of the arm and decrease with radial distance from the arm axis, and if the field lines are parallel to the arm, the anisotropy is expected to the direction of galactic south pole, which corresponds to the following direction in R.A.:

$$\alpha = 12^{\circ} \ , \ \delta = -28^{\circ} \ .$$

If the direction of field lines is opposite, the direction of anisotropy is expected to be

$$\alpha = 192^{\circ} \ , \ \delta = +28^{\circ} \ .$$

Here it must be noted that if cosmic ray density is higher toward the Galactic center or Loop I than toward anti-galactic center, excess flux from the direction opposite to the above mentioned is expected.

The amplitude of anisotropy perpendicular to the arm due to this mechanism is expressed as follows:

$$r_{\perp} = \rho \left[\frac{1}{n} \frac{dn}{dr} \right]$$

$$= \frac{2\rho}{r_0} \times \left[\frac{R}{1 - R^2} \right] \ , \qquad (3)$$

where r_0 is the radius of the arm, r is the radial distance from the center of the arm and $R = r/r_0$. From equation (3), we can find that the amplitude has linear correlation with cosmic

ray energy. Detail to derive equation (3) is described in appendix C. Taking typical parameters of r_0 = 500 pc and H = 3 μ Gauss. the amplitude with respect to the energy is calculated for R = 0.6, and is shown in Fig.4 designated by 'S'.

The simulations considering above two types of anisotropies are done by some authors such as Bell et al. (1974), Honda et al.(1985) and so on, but the results are not consistent with each other.

Bell et al.(1974) treat the diffusion of cosmic ray in the Galactic spiral arm with large scale magnetic field and scattering clouds, and calculate the expected anisotropy to obtain the amplitude about 0.4 % below 10^{16} eV and rapid increase above it ('B' in Fig.4), the direction of which is parallel to the spiral arm below about 5×10^{15} eV and shifts at high energies.

On the contrary, preliminary results of Monte Calro simulation for high energy cosmic ray propagation by Honda et al.(1985) show that there is no excess flux coming from the parallel to the arm axis at the energy region from 1×10^{16} eV to 3.2×10^{17} eV. Here uniform distribution of cosmic ray sources is assumed. And also the strength of uniform magnetic field and of its turbulence with scale of 10 $\sim$ 30 pc are assumed to be 3 μ Gauss and 1.5 μ Gauss, respectively, which decrease with radius exponentially. And 600 pc is taken as the radius of arm.

c) Diffusion models in the Galaxy

As the anisotropy predicted by the diffusion model, the following directions are expected; the excess from the Galactic southern hemisphere due to the location of solar system which is on the northern side of the Galactic plane (for example, McIvor 1977, Owens and Jokipii 1977, Nishijima 1983), the excess from the Galactic center or the Galactic

plane due to the assumption of source distribution like HI, SNR, etc.(for example, Giler 1983), the excess from the direction of some local sources (for example, Dorman et al. 1984), and so on.

Simple diffusion model assuming isotropic diffusion in the Galactic disk and halo with reasonable astrophysical parameters predicts excess from the southern part toward Galactic center (Nishijima 1983). However the author leaves the effect of gyro-motion out of consideration. The result of the improved diffusion model will be discussed in the later chapter.

McIvor (1977) shows that the MHD turbulence in the interstellar medium may be able to confine cosmic rays with energies between $5 \times 10^{11} \sim 4 \times 10^{17}$ eV. And through causing them to scatter off the magnetoturbulent eddies, energy dependence of "up-down" anisotropy (Morrison et al. 1954) which depends sensitively on the thickness of the disk is predicted as is shown by symbol 'M' in Fig.4, where using h_d = 150 pc and z_s = 10 pc (the distance from the disk to the solar system).

Owens and Jokipii (1977) find that not only the observed mean free path, matter traversed, interstellar γ ray flux but also the observed anisotropy are consistent with the dynamical halo model in which cosmic rays are confined in an outward-moving galactic halo. The parameters used here are as follows; the disk scale height of $4 \sim 10$ kpc, average convection velocity of less than 60 km s^{-1}, diffusion coefficient of being proportional to $R^{1/3}$ (where R is particle rigidity) and $z_s = +(1/10)h_d$. This model also predicts the southern excess anisotropy, and its energy dependence is shown in Fig.4 by 'DH'.

On the other hand, Giler (1983) has also examined the cosmic ray diffusion in the Galaxy assuming the Galactic center as the source of cosmic rays, and a constant amplitude

from 10^{14} eV to 10^{17} eV is obtained though the magnitude is uncertainty ('G' in Fig.4).

Dorman et al.(1984) have estimated the contribution of local SNRs in vicinity of solar system as the source of cosmic ray to the anisotropy by diffusion model and obtain expected amplitude as a function of diffusion constant. They show it is not excluded that cosmic ray acceleration is due to pulsar only. Streitmatter et al.(1985) have explained the observed energy spectrum and anisotropy by assuming that the solar system locates close to and within the supper bubble and by considering the superposition of contribution of cosmic rays from inner and outer of superbubble.

d) Expected energy dependence of anisotropies from some models

Taking $\lambda \sim 5$ g cm^{-2} of the traversed matter by cosmic ray at rigidity of 10 GV and $\lambda \sim R^{-0.7}$ of its rigidity dependence (Ormes and Protheroe 1983), extrapolated value to 10^5 GV is about 0.01 g cm^{-2}. In leaky box model, Blandford and Ostriker (1980) give an anisotropy of about

$$r(R) = \frac{1}{2} \frac{\lambda_D}{\lambda(R)},$$

where $\lambda_D = 2 \times 10^{-3}$ g cm^{-2} is the mean column density of gas through the galactic disk. Substituting 0.01 into λ, the expected anisotropy is calculated as ~ 10 %, which is larger than the observed one by about two order of magnitude. When 0.3 is taken as the power of R, it is about 0.3 % ('LB7' and 'LB3' in Fig.4 respectively).

Peters and Westergaard (1977) show that the expected anisotropy of the nucleon flux in closed Galaxy model is represented as follows:

$$r_N(E) = \left[\left\{ \frac{R_0}{R} \right\}^{1/2} + \frac{200\ \Lambda}{K a_s n_s} \right]^{-1}.$$

where Λ is the attenuation length for nucleons in hydrogen, K a measure of the fraction of Galactic gas located in the spiral arm, a_s the thickness of the arm, n_s the density of gas in the arm, and $R_0 = 9 \times 10^8 H_{\parallel} a_s$ GVc^{-1}. In this model anisotropy is mainly attributed to the young components, that is, heavy ones. For iron nucleus, the energy dependence of anisotropy is shown in Fig.4 by 'Cl'. For the lighter elements than iron, the smaller anisotropy is expected.

Being related to the energy dependence of leakage time from the Galaxy, Hillas (1984) shows the change of energy dependence of first harmonic amplitude at the energy region above $10^{15} \sim 10^{16}$ eV. Representing the source spectrum of cosmic ray as $Q(E) \sim E^{-\gamma}$ and the life time of escaping from the Galactic arm or the Galaxy as τ (E), the density of cosmic ray can be expressed by $n(E) = Q(E) \times \tau$ (E). Here the relation of amplitude and escape time is $r(E) \sim 1/\tau$ (E), so

$$r(E) \sim 1 / \tau (E) = E^{-\gamma} / n(E)$$
$$\sim E^{-\gamma} / J(E),$$

where J(E) is the differential energy spectrum of cosmic ray. He shows taking 2.47 as the power of source spectrum, observed anisotropy can be explained. However phase is not explained by this model.

Ⅲ-3. Attempts to Interpret Observed Anisotropy

a) Below 10^{14} eV

The observed data for anisotropy of arrival direction at energy below 10^{14} eV were explained by the model of two types

of anisotropies (Nagashima and Mori 1976). One is by C-G effect due to the motion of the solar system relative to the interstellar gas (ISG), and another is an anisotropy of loss cone type.

The direction of loss cone axis which they assumed is toward l = 110° and b = -40° in Galactic coordinate. This suggests the possibility of magnetic field line pointing toward that direction which is inconsistent with the mean direction of Galactic magnetic field near us given by radio RM. However Sofue and Fujimoto (1983) report the positive RM at l = 100° , b = -20° which is consistent with loss cone axis assumed above, and this may result from the interstellar magnetic field directed toward us. Furthermore, the degree of polarization of optical starlight (Mathewson and Ford 1970) seems to be small at l = 110° , b = -20° which supports the value of RM. So if the data of anisotropy are true, cosmic ray data may confirm it independently.

But to our regret, new data of UV observation reveal the motion of solar system relative to the ISG, which is presented in Table 1. and is different from the value they adopted. So the problem remains open.

b) UHE gamma-rays

On the other hand, Wdowczyk and Wolfendale (1983) has presented a view that the contribution of UHE gamma-ray dominates the anisotropy from 10^{14} to 10^{16} eV, because the energy spectrum of gamma-ray at low energy (order of MeV) appears flatter than that of nuclei (most of them is proton). The ratio of intensity of gamma-ray to nuclei becomes significantly large above 10^{14} eV. A plausible location of gamma-ray sources along the Galactic disk predicts the anisotropy of which peak intensity toward 300° .

The data of Baksan group (Alexeenko and Navarra 1985) support this claim. They compare the phase and amplitude of

anisotropy for the first and second harmonics obtained by Baksan EAS array at the energy region of $10^{13} \sim 10^{14}$ eV with those obtained from COS-B data extrapolating diffuse gamma-ray flux to SAS region, and show the surprising coincidence with both results.

Another view of UHE gamma-ray production is given by Bhat et al.(1986), who have calculated the latitude dependence of intensity for secondary UHE gamma-rays. Primary UHE gamma-rays from the Galactic disk interact with 3 K micro wave back ground photon in the Galactic halo and produce electron-positron pair. Such electron and positron lose their energy partly by radiating X-ray through synchrotron process in the magnetic field of Galactic halo, but partly by scattering the 3 K back ground photon into the UHE gamma-ray energy through inverse Compton process. The result claims that the existence of UHE gamma-rays from high Galactic latitude does not necessarily contradict with the UHE gamma-ray sources in the Galactic disk.

c) GAS region

For GAS energy region, its origin is still an open question. However, if the dominant composition is proton. extragalactic origin for example Virgo cluster is natural because Larmor radius is the same order as the scale of our Galaxy. If primary component is heavy nuclei, Galactic origin can be allowed, The observational study on the distribution of arrival direction is an essential key to solve the origin also in this energy region.

CHAPTER Ⅳ . AKENO EAS ARRAY

Ⅳ -1. General Remarks

The EAS Array of Akeno Observatory spans about 1 km^2 area at latitude of 35.° 8 north. The average altitude is 900 m above sea level and the atmospheric depth is about 930 g cm^{-2}. The array consists of three types of detectors, scintillation counters for charged particles, proportional counters (PC) shielded by concrete for muons or energetic particles and optical mirror telescopes for cerencov light detection. The array aims to observe EAS with energy of about several times $10^{14} \sim 10^{18}$ eV.

Details of the Akeno array are described by Hara et al. (1977a). In the following section only general description is presented. (Now the Akeno array has been expanded to about 20 km^2 out side this 1 km^2 array to detect EAS above 10^{18} eV, but we do not mention it here.)

Ⅳ -2. The Array of Scintillation Counters

The charged particle (mainly electron and photon components of EAS) density is measured by an array of plastic scintillation counters which consists of six 2 m^2 counters, one hundred forty eight 1 m^2 counters, thickness of which is 5 cm, and other small and thin counters (Hatano et al. 1979). The counters of 1 m^2 and 2 m^2 are arranged in lattice shape at 120 m mutual intervals over the area of about 1 km × 1 km. Inside of this 120 m span array, four dense arrays, we call S1, S2, S3 and S4 area, are spanned in lattice shape with interval of 30 m and 60 m. The arrangement is shown in Fig.7.

In each detector, 5" photomultiplier tube (PMT) is installed. Output signal from PMT is amplified and its pulse height is converted logarithmically into time width and

digitized by a clock of 2 MHz. Dynamic range of the combination system of PMT and amplifier is from 1 to a few times 10^5 particles per detector for 1 m^2 counters.

Ⅳ-3. Fast Timing System

Among scintillation counters, four counters in S1, sixteen counters in S2, twelve counters in S4 and fifty five counters in 120 m span array are installed with the fast timing equipment for determination of arrival direction (Ishikawa et al. 1981).

In the case of 120 m span array, a HTV type 1068 5" PMT is used both for density and timing measurement, and arrival time is taken directly by counting clock signal of 200 MHz in each detector. Overall accuracy of timing is about 10 n sec in the case of more than 4 particles incidence per detector.

In the case of local FT systems, a RCA type 6655A 2" PMT is installed to each detector besides PMT of 5" for density measurement. An output signal of each detector is start pulse and the fastest pulse which is delayed by 400 n sec is used as stop pulse, and the pulse with width of the time difference are stretched about 330 times and counted by clock of 2 MHz. Overall accuracy of timing is about 2.5 n sec in this system.

The accuracy of determination for arrival direction is about 5° for 120 m span array and 2° ~ 3° for 30 m span array.

Ⅳ-4. Muon Stations

There are two types of muon stations, one of which is called M-station, and the other called ME-station.

M-station is shielded by concrete of 2 m thickness and its threshold energy for vertical muon is 1.0 GeV. Fifty PCs are put in a single layer just under the roof and its effective area is 25 m^2 per station. Top and side views of M-station are

shown in Fig.8. Eight of M-stations are operated. Among these stations, one named M-5 has additional two layer of fifty PCs apart from each other for about 20 cm where projections of muon trajectories are observable.

ME-station is also shielded by concrete but its thickness is 1 m, so the threshold energy for vertical muon is 0.5 GeV. The effective area is 50 m^2 with a hundred PCs per station. Two ME-stations are operated but adding concrete blocks of 1m thick to the roof, west half part of ME-2 is in operation as three layer M-station with threshold energy 1.0 GeV like M-5.

The total effective area of muon stations are 225 m^2 for 1.0 GeV muons and 75 m^2 for 0.5 GeV. For the details of muon detectors, see Hayashida et al.(1979) and Hayashida and Kifune (1980).

Ⅳ-5. Data Acquisition System

All detectors at Akeno array are connected to the mini computer 'MELCOM 70/25 (Mitsubishi Electric Corp.)' through the 'loop 2 data transmission system' (Mitsubishi Electric Corp.). The outputs from all detectors are recorded, the total number of being 3000 channels per event.

The digitized signals from each detector are transmitted to the central computer. Transmission speed of signal on the 'Loop system' is 300 kbps and total time required for registration of signal from all the detectors to the MT (magnetic tape) is about a few seconds.

More details of this system should be referred to Hara et al.(1977b)

CHAPTER V . MEASUREMENTS OF ARRIVAL DIRECTION AT MEDIAN ENERGY OF 6×10^{14} EV

V -1. General Remarks

The measurement of anisotropy in arrival direction of cosmic ray at median energy of 6×10^{14} eV has been done by recording only counting rate, which is hereafter called 'rate trigger'.

The outline of rate trigger is that the same triggering condition is set in each M-station and the trigger rate is recorded independently. This method has advantage of stable and high rate observation for good statistics.

Another characteristic of this method is to be triggered by muon density (muon trigger). The reasons why muon detectors are used to trigger EAS are as follows. Firstly, in case of muon trigger the effect of triggering bias is smaller than in electron trigger because muon size fluctuate less than electron size at fixed primary energy. So the contamination of low energy showers can be reduced. Secondly, the response of the muon detectors, the proportional counters, is less affected by the temperature variation than scintillators, and moreover they are in the shielded rooms where the solar time variation of room temperature is almost negligible.

Details of observation are described in the following sections.

V -2. Method of Observation

a) Trigger condition

Fifty PCs set at each M-station are divided into five blocks of ten PCs each, and a unit consists of eight PCs except two end PCs for each block. Triggering condition is the

five fold coincidence of five units where more than one muon hits any eight PCs in each unit. This coincidence rate is recorded. The reason why the end PCs are excluded is to avoid the effect that single muon incident with large zenith angle pass through two neighboring units and appears just like two muons. Further, each unit is regarded as one detector and its counting rate (i.e., counting rate of single muon) in each unit is also recorded. These data are available to monitor the drift of experimental conditions in each PCs, the circuit systems, and the atmospheric effect of counting rate.

It is checked and confirmed by the detailed analysis of data taken for estimation of primary energy that the above scheme of triggering is free from local showers or bursts in the concrete shielding, and it will be described in the next section.

The block diagram of trigger circuit set at the each M-station is shown in Fig.9. Output pulses from each PC are amplified to thirty times of its voltage and are discriminated by the threshold level of 0.3 particles. The pulse passing through the discriminator is then shaped to a square pulse of five micro seconds width and fed to a coincidence circuit constituted of TTL. The output pulse from the coincidence circuit is again shaped to a square pulse of five micro seconds and latched. On the other hand, single muon pulses are branched before 'AND' gate and reduce their frequency to factor $1/2^{16}$ by binary counters, and output pulses from five each counters are mixed. This output frequency corresponds to counting rate of single muon in each M-station. This pulse is also latched. These two kind of signal pulses are controlled by a multiplexer to transmit one by one. Their pulses are encoded to eight bits serial data by a universal asynchronous receiver and a transmitter (UART) in order to identify the two kinds of signals and to avoid accidental count caused by electrical noise on transmission. Data are transmitted to the

Center through a coaxial cable with baud rate of 9600 baud per sec.

b) Data taking system

The arrangement of M-stations and ME-stations of Akeno EAS array is shown in Fig.7. At each station, the coincidence circuit already mentioned is set and the data of each station are collected at Center. The block diagram of data taking system at the Center is shown in Fig.10. One micro processor (z-80) controls this system. The data sent from each station are received by the universal synchronous asynchronous receiver and transmitter (USART). The micro processor always scan whether the data are coming, or not. When the data are inputted, CPU reads its bit pattern and select coincidence signals, single signals or error pulses, and adds the counting number of each channel at the memories. The data are read out every one hour and are outputted to PTP (paper tape puncher).

If a large EAS arrives, a coincidence occurs at the plural stations at the same time and counting rate is overlapped. This effect is eliminated in the later analysis. We regard it as a coincidence when any stations satisfy trigger condition during one scan cycle after any other station satisfies it. It takes about 300 μ sec to scan data of ten channels. the accidental coincidence rate of this method is therefore about 2×10^{-2} hr^{-1}, which is negligibly small.

V -3. Estimation of Primary Energy

Before the constant operation of RM trigger, a preliminary operation was carried out using M-5 station to infer the response for primary energy with this trigger . Coincidence pulses from RM trigger are inputted to the 'Loop system' to know electron density, muon density and timing data in each event, which are analyzed by normal method to get basic shower

parameters, such as electron size, muon size, age and so on.

The observation time is 16.9 hrs in live time and the number of observed shower is 850 events.

Figure 11 shows the integral distribution of (a) N_μ and (b) N_e. From Fig.11(a), the median muon size is 1.3×10^4. The primary energy,

$$E_{o,median} = 6.1 \times 10^{14} \text{ eV}$$

is derived from the size, where the relation between muon size and primary energy derived by Nagano et al.(1984) is extrapolated to this muon size.

As shown in Fig.11(b), the electron size of about 26% of triggered events can not be determined because of no electron data (called mu-only event). The occurrence of these mu-only events can be explained as follows.

The nearest scintillation counter to M-5 station is at the distance of about 20 m. At this distance, assuming an age parameter S = 1.2, a vertical shower whose electron size is less than or equal to $10^{4.0}$ (this corresponds to energy of $10^{13.8}$ eV) gives electron density less than a single particle. Further, assuming the zenith angle distribution of frequency as $\cos^5\theta$ and the power of integral energy spectrum -1.5, the rate of EAS whose core hits M-5 station is about 11 hr^{-1} for $E_o \geqq 10^{13.8}$ eV and this rate is compatible with the rate of mu-only events.

Next, the possibility of the accidental coincidence by two single muons is considered. It is pointed out by Shimonaga (1980) that burst particles produced from a single muon are spread over four units and the case is not often but observed at our muon station. When such a burst accidentally coincides with another single muon hitting other unit, the trigger condition is satisfied. This contribution to the triggered events is checked. The counting rate of such a burst is

expected to be not so sensitive to the area of each unit because burst particles are closely spread all over the four units. On the other hand, as muon shower particles are scattered, area of each unit affects the counting rate strongly. Therefore, if the mu-only events produce from the above effect, dependence of counting rate on the area of one unit is weaker than the case of real muon shower event. We test such dependence by analysis of the data as follows. We have density data of each PC for each event, so the events which are satisfied the five fold coincidence of each unit with two, three, four, five or eight PCs can be selected respectively in the data, and the counting rate of each case is plotted in Fig.12. They show that there is no difference between the case of all events (open circles) and the case of mu-only events (closed circles). From the above mentions, the mu-only events are considered to be small EASs having energy of around 10^{14} eV.

To make sure, we check muon tracks (to be exact their projections) for each mu-only event by using the data of hit pattern on the three layers, and 68 events which are not certainly identified to the air shower are remained. It corresponds to 8 % of all events. At present stage, such events are regarded as the small air showers with the size less than about 10^5 in accordance with previous mentions.

Then N_e distribution gives $N_{e,median} = 1.5 \times 10^5$ and corresponding primary energy is obtained to

$$E_{o,median} = 7.1 \times 10^{14} \text{ eV}.$$

This value is very close to the value derived from N_μ distribution.

Thus the median primary energy of cosmic rays observed by RM trigger is estimated as 6.1×10^{14} eV.

V -4. Data Reduction for Harmonic Analysis

The operation by this trigger has been started on June 1984. The data of 2,682,363 events recorded for just one year from july 1984 to June 1985, are analyzed in this paper.

In order to avoid the spurious anisotropies caused by artificial effects, such as the interruption of operation by maintenance work, power failure of electricity and mal-operation due to troubles in electric circuits etc., the records of operation during a year are checked. A day is divided into 24 bins in width of an hour in solar time. The data of the whole day including the bin when constant operation is disturbed are rejected from the analysis, assigning the zero flag to bins of such a day. Otherwise flagged one is defined to the bins of the day with normal operation.

The effective operation time after the data reduction mentioned above is 7043 hours, the value of which is averaged over each M-station. The efficiency is 80 % in rate trigger.

This procedure has enabled us easily to correct for the effect of non-uniformity of observation, but this correction is applicable only to solar time but not to sidereal time. Here this sidereal time is determined at the time of bin center for solar time, and the flag of its bin is sorted into alternative bin of an hour width in sidereal time. Then the sums of flags in each bin of sidereal time are regarded as the weight of observation time in each bin. In Fig.13, the distribution of observation time for the phase in sidereal time is presented, which shows almost uniform. The observed events are also sorted into each bin of sidereal time.

CHAPTER VI . MEASUREMENTS OF ARRIVAL DIRECTION ABOVE 10^{15} EV

VI-1. General Remarks

The measurement of anisotropy in arrival direction of cosmic ray in the wide energy range larger than 10^{15} eV has been done by ordinary method which we call 'common trigger' whose data are acquired by 'Loop system'.

We use two kinds of triggering method to acquire air shower data; the one by discriminated by muon density (muon trigger), and the other by electron density (electron trigger).

Generally, electron density is much larger than muon density, so EAS are ordinarily to triggered by electron density. But as mentioned in the preceding chapter, the muon trigger has the following two advantages.

Firstly, in case of the muon trigger the energy resolution is expected to be better than in the electron trigger because muon size fluctuates less than electron size at fixed primary energy. Jogo (1981) has reported that the fluctuation of N_e for fixed primary energy at Akeno level are, for example, 80 % and 70 % for the energy of 10^{15} eV and 10^{16} eV respectively. On the other hand the fluctuations of N_μ are 40 % and 20 % for the same energy regions respectively.

Secondly, as is mentioned before, the response of the muon detectors in Akeno array is insensitive to the temperature variation.

VI-2. Trigger Condition

Among the common trigger, the data taken by three electron triggers (CE1, CE2 and CE3, where C means 'common' and E means 'electron trigger') and one muon trigger (CM, M means 'muon trigger') are suitable to the analysis of anisotropy because of a constant operation condition during a long period.

CE1 and CE2 are the local triggers at the region of S2 and S4 respectively. The triggering condition for CE1 is four-fold coincidence of four adjacent scintillation detectors located at the corner of a square of 30 m sides at the center of S2. The discrimination level is set at about 15 particles. For CE2, the triggering condition is four-fold coincidence just like CE1, but the trigger center is set at S4 and their discrimination level is 10 particles. The threshold of electron size by these trigger is about 3×10^5 and the effective area of 100% detection is established as $2 \times 10^3 \times [N_e / (5 \times 10^5)]^{0.8}$ m^2. Then the non-biased threshold for CE1 and CE2 is at electron size of about 10^6.

CE3 is a wide area trigger. Its triggering condition is seven-fold coincidence out of 38 scintillation counters which form a part of 120 m span array through out the whole area of 1 km × 1km. By this trigger, we can observe the shower of more than 3×10^6 size of electron and the non-biased threshold electron size is about 10^7. Most of the data of $N_e \geqq 10^7$ are taken from this trigger. The effective area is 3×10^{15} m^2 for CE3.

Total trigger rate for these three electron triggers is about 36 events per hour.

The trigger CM is operated, when more than four muons hit each of four muon stations, M-4, M-5, M-7 and ME-2 which are located near the central area of the array. The threshold of muon size by this trigger is about larger than 3×10^4 and non-biased muon size is about larger than 10^5. The effective area is dependent on muon size, given by $6.4 \times 10^3 \times (N_\mu / 10^5)^{1.4}$ m^2 for $N_\mu \geqq 10^5$. The trigger rate for this trigger is almost 10 events per hour.

VI-3. Air Shower Analysis

The core position and electron size of EAS are determined

in both case of electron trigger and muon trigger by fitting the observed electron density in all the scintillation counters to the NKG function (Greisen 1956) of lateral distribution of electron. The function is represented as follows:

$$\Delta_e(r/r_m) = N_e \times f(r/r_m),$$

$$f(R,s) = C(s) \times R^{s-2.0} \times (1 + R)^{s-4.5},$$

where Δ_e is electron density, r is core distance, r_m = 96.1 m is Moliere unit at Akeno and $R = r/r_m$. The value C(s) is the normalization factor which is given by

$$\int_0^\infty f(R,s) \cdot 2\pi R \cdot dR = 1 ,$$

and

$$C(s) = \frac{1}{2\pi} \times \frac{\Gamma(4.5 - s)}{\Gamma(s) \times \Gamma(4.5 - 2s)} .$$

The fitting is carried out by χ^2 minimization method.

The arrival direction of each shower is determined from 'Fast Timing' data by χ^2 fitting in approximation of a plane shower front. The errors in determining arrival direction are less than about 3 degrees for CE1, CE2 and CM, and about 5 degrees for CE3.

The muon size is determined by fitting the muon density to the Greisen's formula (Greisen 1960) for the lateral distribution of muons using χ^2 minimization method. The formula is

$$\Delta_m = \frac{\Gamma(2.5)}{2\pi \times \Gamma(1.25) \times \Gamma(1.25)} \times r_o^{-1.25} \times N_\mu \times r^{-0.75} \times \left(1 + \frac{r}{r_o}\right)^{-2.5},$$

where r_o = 280 m. In order to determine the muon size of each shower, the muon stations located at a distance less than 50 m from the air shower core are excluded from the fitting because they may be contaminated by hadron components and high energy soft components.

The error to determine the muon size is estimated from Monte Calro simulation by Jogo (1981) whose results show that the error is about 50% for muon size of 10^4 and less than 10% for above several times 10^5.

VI-4. Data reduction

a) Operation

Constant operation was started at the end of 1980 for the trigger CE1, CE2 and CE3, and about 850,000 EASs have been accumulated during this period. For the trigger CM, the EAS has been observed since November 1982 and 200.000 showers have been recorded.

In this paper, the data acquired for just four years between the beginning of 1981 and the end of 1984 for the trigger CE2 and CE3, for just three years between 1982 and 1984 for the CE1, and for just two years of 1983 and 1984 for the CM, are analyzed for studying anisotropy.

b) Data reduction for excluding noise events

Data reduction is done as follows. First of all in the analysis are rejected showers whose value of χ^2 of fitting the electron lateral distribution to the NKG function or fitting the muon lateral distribution to the Greisen's formula is larger than 2.0 per a degree of freedom. By this reduction, about 3 % of all triggered events are rejected, which are almost small ASs and miss triggered events. Furthermore we exclude the inclined showers with zenith angle θ larger than

48.° 2 ($\sec\theta$ < 1.5). The showers hitting within the effective area mentioned previously are then analyzed. After these selections, 405,995 events for the electron trigger and 96,645 events for the muon trigger are remained.

The conversions of observed electron size and muon size to the primary energy are done by following two steps.

At the first step, the electron size and muon size which are observed at zenith angle θ , are converted to $N_{e,ver}$ and $N_{\mu,ver}$ reduced to the case of vertical showers respectively, by use of the size attenuation length derived from the equi-intensity cut method (Hara et al. 1983; Nagano et al. 1984). The empirical formulae which are used here are as follows,

$$N_{e,ver} = N_{e,obs} \times \exp[-5.5\ (\sec\theta - 1)] \quad (4)$$

$$N_{\mu,ver} = N_{\mu,obs} \times \exp[-0.73\ (\sec\theta - 1)] \quad (5)$$

At the second step, the conversions of these size to primary energy E_0 are done by using the relation

$$E_0 = 3.9 \times 10^{15}\ (N_e / 10^{16})^{0.90} \quad \text{for } N_e \quad (6)$$

$$E_0 = 1.17 \times 10^{17}\ (N_\mu / 10^{16})^{1.21} \quad \text{for } N_\mu \quad (7)$$

where E_0 is in eV (Nagano et al. 1984).

For the electron trigger the relations (4) and (6) are used and for the muon trigger the relations (5) and (7) are used.

Subsequently we analyze the anisotropy of the frequency of not only the all selected showers, which we call 'all showers', but also the showers classified by the ratio of muon size to electron size. The mean value of N_μ / N_e ratio for vertical showers is 2.75×10^{-2} at $N_e = 10^{7.0}$ at Akeno. The showers whose N_μ / N_e ratios are higher than 0.06 and lower than 0.01 at $N_e = 10^{7.0}$ are selected as 'muon-rich showers' and 'muon poor showers' respectively. The values by this

criterion are varied in accordance with the relation N_μ = const.$\times N_e^{0.83}$ for showers with other size.

c) Data reduction for harmonic analysis

In order to avoid the spurious anisotropies caused by artificial effects, the record of operation during the four years is all checked as the same way as in the case of rate trigger. A day is divided into 24 bins in width of an hour in solar time. The data in the bin (not the whole day) when the constant operation is disturbed, are rejected from the analysis, assigning the zero flag to such bins. Otherwise flagged one is defined to the bin with normal operation.

The effective operation times after the data reduction mentioned above are 27317 hours for CE and 12430 hours for CM, the efficiencies being 78% and 71% for each trigger respectively.

As mentioned in the preceding chapter, this procedure has enabled us easily to correct for the effect of non-uniformity of observation time. Here, the right ascension of arrival direction for each observed event is different from arrival sidereal time. However, making it easy to correct non-uniform observation time, the arrival direction in R.A. is approximated by the sidereal time then. This procedure, in turn, results in large error of right ascension. To minimize such error for common trigger, only events with zenith angle of less than 33.° 6 ($\sec\theta < 1.2$) are used for harmonic analysis, and the maximum error is as large as two hours. However, this will not seriously affect the final results in studying the flux of cosmic ray in terms of harmonic analysis.

CHAPTER Ⅶ. ATMOSPHERIC EFFECT

Ⅶ-1. General Remarks

Besides the artificial effects, the atmospheric effect is one of major cause for spurious anisotropy of EAS.

With variations of barometric pressure, the attenuation of showers changes because the depth of the atmosphere on the point of observation changes. Besides, electrons in the shower are scattered transversely through the atmosphere and the characteristic of scattering is varied in accordance with the density of air which is based on the pressure and temperature of the atmosphere. For nuclear cascade, the behavior of $\pi - \mu$ decay may be changed by atmospheric condition. The temperature characteristic of the detectors must be also considered.

The trigger rate for all triggering conditions suffers the above atmospheric effect and the genuine astrophysical anisotropy of cosmic rays is contaminated. So we check the effect of barometric pressure and atmospheric temperature to the trigger rate in this chapter.

Ⅶ-2. Temperature and Pressure at Akeno

Observations of the barometric pressure and atmospheric temperature are done at the Center of Akeno observatory by use of the 'Digital Pressure Transducer' (Paroscientific INC) for pressure since Mar.1983 and the digital resistance thermometer of platinum for temperature since Aug.1983, respectively.

Figures 14(c) and 15(c) show the seasonal variations of temperature and pressure at Akeno averaged over the period of a year in 1984. From these results we find

$$\text{average temperature} : \langle T \rangle = 8.7\ ^{\circ}\mathrm{C},$$
$$\text{average pressure} : \langle P \rangle = 905.3\ \mathrm{mb},$$

and the range of temperature variation and pressure variation are about 28 ℃ and 10 mb respectively at the Center of Akeno Observatory. Harmonic diagrams for seasonal variation are shown in Figs 16(c) and 17(c) respectively.

In Fig.18 and Fig.19, the solar (a) diurnal and (b) semi-diurnal vectors of temperature and pressure for each month in 1984 are shown respectively. For temperature, the maximum phase are very definite for both first and second harmonics and they hardly vary through a year. Also for pressure, though error circles are comparable to the amplitude, the phases of maximum are nearly the same for each month and the seasonal difference of their phase is negligibly small within error.

Average solar diurnal variations of temperature and pressure over a year are shown in Fig.14(b) and Fig.15(b), and their harmonic diagrams are presented in Figs 16(b) and 17(b) respectively. The pressure diurnal harmonic amplitudes are about 0.543 ± 0.453 mb at the phase of 54° for the first harmonic and about 0.72 ± 0.45 mb at 134° for the second one. These phases correspond to 3.6 hr and 8.9 hr in solar time respectively. The fact that the second harmonic amplitude is as large as first one is well known characteristics. For temperature, the first harmonic phase is 218° ± 2° corresponding 14.5 hr in solar time with amplitude of 3.92 ± 0.16 ℃, and the second harmonic phase and amplitude are 21° (1.4 hr) ± 3° and 7.36 ± 0.16 ℃ respectively.

If the solar diurnal variation of temperature and/or pressure is taken annual modulation, the spurious sidereal modulation is appeared. Fig.14(a) and Fig.15(a) show the variation of temperature and pressure for sidereal phase (0° corresponds to α = 0 hr) averaged over a year of 1984. Their harmonic amplitude and maximum phase are shown in Figs.16(a) and 17(a), and are as follows,

temperature : $r_1 = 0.38 \pm 0.16$ ℃, $\phi_1 = 34° \pm 24°$,
$r_2 = 0.13 \pm 0.16$ ℃, $\phi_2 = 66° \pm 36°$,
pressure : $r_1 = 0.197 \pm 0.453$ mb, $\phi_1 = 266° \pm 169°$,
$r_2 = 0.099 \pm 0.453$ mb, $\phi_2 = 172° \pm 90°$,

where r and ϕ are the amplitude and phase of temperature or pressure respectively, and the subscript indicates the order of harmonics. The first harmonic amplitude for temperature is a little large relative to error, which may be caused by the annual variation of amplitude of diurnal vector seen in Fig.18(a).

Ⅵ-3. The effect of pressure and temperature to the triggering rate

We now define temperature coefficient α and pressure coefficient β as follows,

$$\frac{\partial N}{\partial T} = \alpha \cdot N,$$

and

$$\frac{\partial N}{\partial P} = \beta \cdot N,$$

where N is the counting rate per hour, T the outdoor temperature in degree and P the barometric pressure in mb. So we can assume the relation among N, α and β to be

$$\ln N = c + \alpha T + \beta P, \qquad (8)$$

where c is constant.

The counting rate in every hours is sorted into two dimensional bins of temperature and pressure, and the average counting rates are fitted to three dimensional plane expressed

by the equation (8) using the least square method. Derived energy dependences of temperature coefficients and pressure coefficients for each trigger are shown in Fig.20 and Table 2.

From Fig.20, the energy dependence of temperature coefficients is seen at the energy range from 10^{15} eV to 10^{17} eV where the value of coefficient is negative and increases about from -1.0 % deg^{-1} to 0 % deg^{-1} with energy increasing. Above 10^{17} eV, though error is large, it seems nearly constant. There is no clear difference of temperature dependence of counting rate between the muon trigger and the electron trigger.

It is also found that the pressure effect for counting rate is almost constant with the value of $-0.6 \sim -1.2$ % mb^{-1} independent of energy below 10^{17} eV and is larger for electron trigger than for muon trigger by about a factor two. Above 10^{17} eV, the tendency is similar.

Considering the results of harmonic analysis of temperature and pressure for sidereal time, the rough estimations of the correction vector on amplitude and phase are 0.08 % at 334° for the first harmonic and 0.023 % at 14° for the second harmonic in case of rate trigger, and $0.1 \sim 0.3$ % at $270° \sim 15°$ for first harmonic and $0.1 \sim 0.3$ % at $90° \sim 170°$ for second one in case of common trigger. Here, there is a slight seasonal dependence of values α and β, but such effects to the correction vectors are negligibly small.

Lastly in this chapter, the following is noted. The variation of total counting rate as a function of seasons is large, the first harmonic amplitude of which is about 7.1 % and 4.3 % in case of electron trigger and muon trigger respectively. If the correction of temperature and pressure effect is carried out ideally, these amplitudes are expected to be reduced to near zero. However, even after the above correction is applied to present data, the amplitudes are reduced to 4.3 % and 1.5 % respectively, which indicates that

the correction is not sufficient. This residual effect may be considered to be caused by the seasonal variation of upper air condition. So it will be required to monitor such condition in order to avoid the temperature and pressure effect perfectly.

CHAPTER Ⅷ. ANISOTROPY AT MEDIAN ENERGY OF 6×10^{14} EV

Ⅷ-1. The Results of Harmonic Analysis

The distribution of counting rate versus the phase of sidereal time is shown in Fig.21, where the phase 0° corresponds to 0 hr in R.A. and the correction for the effect of non-uniformity of operation time for the sidereal time has already been done. In this figure, there are two characteristics. One is the excess of about more than three standard deviation at the phase between 285° and 300° , which corresponds to the direction of Galactic plane at Akeno. Another is two heaps appeared in this histogram.

Harmonic analyses are carried out about counting rate for (a) sidereal time, (b) solar time and (c) anti-sidereal time. Results are shown in Table 3 and in Fig.22, where r_i and ϕ_i are the amplitude and phase of maximum flux, and k is the parameter representing statistical reliability and the probability of obtaining amplitude greater than r from the uniform distribution is given by $P(>r) = \exp(-k)$ $(k = r^2N/4)$ (Linsley 1975). The effects of atmospheric temperature and barometric pressure are not corrected for counting rate at a present stage. The results are as follows.

1) The phase of maximum flux for first harmonic in sidereal time appears at 340° which is the direction of 22 hr - 23 hr in R.A..
2) For the component of second harmonic for sidereal time, considering only the statistical error, a significant amplitude of 3.5σ whose direction is about 6 hr (and 18 hr) in R.A. is seen.
3) The amplitude for anti-sidereal time is as small as statistical error.

Ⅷ-2. Significance of the Results

The seasonal variation of solar time vector can be thought to be the cause of spurious sidereal time variation. But as shown in Figs 18 and 19, the temperature and pressure variations for solar time which are considered to be a main cause of solar time vector variation are not significantly large during a year, and so those effects are expected to be small.

In another view, if the true variation for the sidereal time exists, We can expect the vector for solar time to rotate around the average vector with the radius of norm of vector for sidereal time by month to month. The reason is as follows. The sidereal time is shorter than the solar time by about one day per a year, so the vector goes forward to the phase by just one period on the harmonic diagram of solar time, that is, the vector rotates by one cycle during one year for the first harmonic and a half year for second one. This is shown in Fig.23, where for easy to see, the diagram for first harmonic is also shown separately for two half years (Fig.23(a)). There is no evidence for the first harmonic vector to rotate clearly because of large error related to the amplitude, but the direction of rotation is roughly consistent with expected one, or at least not inconsistent with it. For the second harmonic, we can say the vector rotates toward the expected direction except one depression. From above test, the existence of the half day variation of the cosmic ray flux in this energy is appeared to be true.

Lastly, temperature and pressure effects are considered. The amplitude and phase of maximum flux for the sidereal time which have been corrected for the temperature and pressure effects are

r_1=0.23± 0.09 %, ϕ_1=330° ± 21° , k_1=3.58, $P(>r_1)=2.8\times 10^{-2}$
for first harmonic

r_2=0.30± 0.09 %, ϕ_2= 92° ± 8° , k_2=5.96, $P(>r_2)=2.6\times 10^{-3}$
for second harmonic

where the subscript i indicates the order of harmonics.

Figure 24 shows the sidereal time vector before (dotted circle) and after correction (bold circle) for temperature and pressure effect with anti-sidereal time vector after correction (thin circle) for the first and second harmonics respectively. The statistical error of their amplitudes is 0.09 %, and the expected effect by temperature and pressure from the results of the previous chapter is within errors.

CHAPTER Ⅸ . ANISOTROPY IN THE ENERGY REGION ABOVE 10^{15} EV

Ⅸ-1. Celestial Distribution of Cosmic Rays

The celestial distributions of arrival direction of cosmic rays in the energy region between 10^{15} eV and 10^{19} eV are shown for all showers in Table 4, for muon-rich showers in Table 5 and for muon-poor showers in Table 6. In those tables, observed numbers of events from cellular division of $\Delta\alpha = 10°$ and $\Delta\delta = 10°$ are presented in case of (a) electron trigger and (b) muon trigger respectively. The values of χ^2 for assuming uniform distribution for right ascension at fixed declination band are also shown in the bottom lines in these Tables. From these tables, we can find no remarkable excess or 'hole' in any cells or regions.

To see details of distribution of arrival direction, the deviations of events number in each cell from the expected values are calculated for each trigger and for each muon content. The expected values are given by averaging observed event number over right ascension in each declination band. The results are presented in Figs 25 ~ 27 as the celestial map in unit of standard deviation for the results summed over all energy bins. The meanings of each mark are described in the figure captions. These figures show that the number of cells beyond 2σ is not inconsistent with that expected from the statistics when the arrival direction is distributed isotropically, and these cells are distributed almost randomly. Therefore there is no evidence to support positively the existence of excess or lack region beyond the statistical fluctuation.

Ⅸ-2. Results of Harmonic Analysis for Sidereal Time

The results of harmonic analysis for all observed showers

are presented in Tables 7 ~ 9 and Figs 28 ~ 30 with the amplitude and phase already corrected for the temperature and pressure effects, where closed circles designate the results for muon trigger and open circles for electron trigger. The results show following features.

a) For all showers

From Fig.28(a), we find very characteristic features for the first harmonic that the maximum flux phase is almost constant around 300° in R.A. for energy range more than two decades above 10^{15} eV in both case of muon trigger and electron trigger. The amplitude and phase summed for electron trigger show the following values:

r_1=0.80± 0.26 %, ϕ_1=294° ± 19° , k=4.71, for E=(1-32)× 10^{15}eV,

and for muon trigger in each decade:

r_1=1.74± 0.78 %, ϕ_1=332° ± 26° , k=2.50, for E=(1-10)× 10^{15}eV,
r_1=2.13± 0.73 %, ϕ_1=313° ± 20° , k=4.23, for E=(1-10)× 10^{16}eV,
r_1=2.46± 2.31 %, ϕ_1=312° ± 54° , k=0.57, for E=(1-10)× 10^{17}eV,

The chance probabilities that the random fluctuation produces such values of k = 4.71 in case of electron trigger and k = 4.23 in case of muon trigger are 9.0 × 10^{-3} and 1.5 × 10^{-2}, respectively. The anti-sidereal amplitudes for above two energy regions with large k values are calculated as follows;

r=0.12 ± 0.26 % for (1 - 32)× 10^{15} eV in electron trigger
r=0.38 ± 0.73 % for (1 - 10)× 10^{16} eV in muon trigger.

They are enough small compared with the signal level. Furthermore, Fig.31(a) and (b) show the results of each year for the same energy regions, respectively, where dotted

circles indicate the results for sidereal time in each year, bold circles indicate that of sum and thin circles indicate that for anti-sidereal time. Even though the fluctuations are seen, the results of each year are consistent within error. So we can say that the significance of the anisotropies for above energy regions is enough high.

On the other hand, in the level of 10^{15} eV, the signal level is comparable to the noise level and its reliability seems to be not so high.

For the second harmonic, indication of strong anisotropy beyond the noise level is not found from Fig.28(b) or Table 7 except for the energy region of (3.2 - 10) $\times 10^{16}$ eV in case of electron trigger. In that energy region, the probability of obtaining observed amplitude from the uniform distribution is 6.0×10^{-3}. The anti-sidereal amplitude for it is calculated to be 1.35 ± 0.82 % and the signal level is 1.9 times larger than it. However, considering the fact that the expected number of samples with $k \geqq 5.1$ from the random fluctuation is estimated as 0.4 accordingly, the obtained value of $k = 5.1$ is not inconsistent with random fluctuation.

This figure also shows the following tendencies that for the electron trigger the phase seems to be almost constant with around 150° below 3×10^{16} eV, and for higher energies the amplitude increases and phase changes gradually with energy. These features are not inconsistent with those of muon trigger within errors. However their significance is rather poor.

b) For muon-rich showers

Figure 29(a) for the first harmonic shows that there is no energy bin where the amplitude exceeds two standard deviation except only one for (1 - 3.2) $\times 10^{17}$ eV in electron trigger. However the anti-sidereal amplitude for that energy is comparable to the signal level considering the error and then

the significance is not so high.

It is also shown that the energy dependence of maximum flux phase is different from that of all showers especially around 10^{16} eV for muon trigger. Figure 32 shows the maximum phase of first harmonic of muon trigger (the result of electron trigger is also shown in figure (b)) for three energy bins between (1 - 32) $\times 10^{15}$ eV as a function of the fraction of selected events biased to muon rich by criteria of N_μ / N_e ratio. A clear change of phase is noted around the fraction of 60 % in figure (b) for muon trigger. For electron trigger, its difference is not so clear but its tendency is not inconsistent with for muon trigger. About this, we will discuss in the latter chapter.

In Fig.29(b) for the second harmonic, There is no significant anisotropy for both trigger and only upper limits are obtained in some energy bins. However, for energy above 3.2 $\times 10^{16}$ eV, the phase of maximum flux slightly tends to concentrate at about 60° to 100° in R.A. for both trigger, even though their significance is poor.

c) For muon-poor showers

Figure 30 shows that the first harmonic phases are near 330° in R.A. below 3.2 $\times 10^{16}$ eV, whose amplitudes are (1~5) %. The maximum phases are nearly the same for total showers. In the energy range of (3.2 - 10) $\times 10^{15}$ eV, the chance probability producing the amplitude due to random fluctuation is 2.5 $\times 10^{-2}$ and which signal level is 1.9 times larger than the anti-sidereal amplitude of 2.76 ± 1.94 %. However combined amplitude for the energy range of (1 - 32) $\times 10^{15}$ eV is the same level as the noise and it is statistically low significance.

For the second harmonic, the maximum phases are almost constant around 170° in R.A. independent of energy, and each amplitude is as high as several %.

The amplitude and phase for sidereal and anti-sidereal time summed over the energy between 1×10^{15} eV and 1×10^{17} eV are calculated as follows:

sidereal: r_2=4.62± 1.24 %, ϕ_2=166° ± 8° , k=6.97,
anti-sidereal: r_2=0.75± 1.24 %, ϕ_2=134° ± 47° , k=0.18,
for E=1×10^{15}-1×10^{17} eV.

The chance probability producing such anisotropy from the fluctuation is 9.4×10^{-4} and signal level is 6.2 times larger than noise level. This is very significant anisotropy. Figure 31(c) also shows that the phases of each year for muon-poor showers are consistent.

e) Other remarks on the significance of the data

Firstly we consider the difference of the results between muon trigger and electron trigger. Two populations which are analyzed as each trigger events are slightly different. A part of the difference between them is explained by the lack of muon-poor showers in case of muon trigger. The fractions of muon-poor showers are about 4 % for electron trigger and 0.3 % for muon trigger respectively. So it is not surprising that there is a slight difference of anisotropies between each triggered events. In fact, the difference of the first harmonic phase in the energy bin of $(3.2 - 10) \times 10^{16}$ eV is explained approximately by the above mentions. However, we cannot explain the fact that the amplitude of first harmonic in case of muon trigger below 10^{17} eV appears systematically larger than in case of electron trigger. We are trying to clear up the cause but the difference has been remained. However, at present, taking account of their errors, it is desired to accumulate more data in this region.

It also must be noted here that the data at the lowest energy bin in common trigger events may be sensitive to a

slight change of operational circumstances because the shower size of such events is near to the threshold size. So they may suffer trigger bias and the reliability is not enough. In fact the amplitude of first harmonic for such bin abruptly change from the reliable point at 6×10^{14} eV and looks artificial.

Lastly, the effect of correction connected to the temperature and pressure is checked. In Fig.33, harmonic diagrams before (dotted circles) and after (solid circles) correction of the temperature and pressure effect are shown for some energy regions, which show the quantities of correction both for amplitude and phase are very small, compared with the observed amplitude and statistical error, so the error from the uncertainty of temperature and pressure coefficients can be taken as small.

Ⅸ-3. Summary of the Results of Harmonic Analysis

From the results of examination in the previous section, there are three comparatively significant anisotropies, which are summarized as follows:

1) For all showers in case of electron trigger
$r_1 = 0.80 \pm 0.26$ %, $\phi_1 = 294^\circ \pm 19^\circ$, $P(>r) = 9.0 \times 10^{-3}$, for $E = (1 - 32) \times 10^{15}$ eV.

2) For all showers in case of muon trigger
$r_1 = 2.13 \pm 0.73$ %, $\phi_1 = 313^\circ \pm 20^\circ$, $P(>r) = 1.45 \times 10^{-2}$, for $E = (1 - 10) \times 10^{16}$ eV.

3) For the muon-poor showers($N_\mu / N_e < 0.01$)
$r_2 = 4.62 \pm 1.24$ %, $\phi_2 = 166^\circ \pm 8^\circ$, $P(>r) = 9.4 \times 10^{-4}$, for $E = (1 - 100) \times 10^{15}$ eV.

Other anisotropies which are not very significant but cannot be excluded are as follows:

4) For all showers in case of muon trigger

$r_1 = 1.74 \pm 0.78$ %, $\phi_1 = 332° \pm 26°$, $P(>r) = 8.21 \times 10^{-2}$, for $E = (1 - 10) \times 10^{15}$ eV.

5) For all showers in case of electron trigger

$r_2 = 2.61 \pm 0.82$ %, $\phi_2 = 106° \pm 9°$, $P(>r) = 6.0 \times 10^{-3}$, for $E = (3.2 - 10) \times 10^{16}$ eV.

6) For muon rich showers in case of electron trigger

$r_1 = 17.7 \pm 7.5$ %, $\phi_1 = 261° \pm 28°$, $P(>r) = 1.2 \times 10^{-1}$, for $E = (1 - 3.2) \times 10^{17}$ eV.

7) For muon rich showers in case of muon trigger

$r_2 = 3.38 \pm 1.68$ %, $\phi_2 = 60° \pm 14°$, $P(>r) = 1.3 \times 10^{-1}$, for $E = (0.32 - 3.2) \times 10^{17}$ eV.

8) For muon poor showers

$r_1 = 5.27 \pm 1.94$ %, $\phi_1 = 329° \pm 21°$, $P(>r) = 2.5 \times 10^{-2}$, for $E = (3.2 - 10) \times 10^{15}$ eV.

In other energy regions, no statistically significant anisotropies are observed. Obtained upper limits of the amplitude with 95 % confidence level for all showers are as follows;

In case of electron trigger

$(1 - 10) \times 10^{15}$eV :		$r_2 \leqq 1.23$ %
$(1 - 3.2) \times 10^{16}$eV :		$r_2 \leqq 1.70$ %
$(3.2 - 10) \times 10^{16}$eV :	$r_1 \leqq 2.44$ %	
$(1 - 10) \times 10^{17}$eV :	$r_1 \leqq 6.98$ %,	$r_2 \leqq 9.02$ %

In case of muon trigger

$(1 - 10) \times 10^{15}$eV :		$r_2 \leqq 2.06$ %
$(1 - 10) \times 10^{16}$eV :		$r_2 \leqq 2.23$ %
$(1 - 10) \times 10^{17}$eV :	$r_1 \leqq 7.08$ %,	$r_2 \leqq 5.53$ %

Ⅸ-4. Anisotropy on Galactic Coordinate Above 10^{15} eV

a) General Remarks

It is natural to describe the anisotropy of arrival direction by the Galactic coordinate. The distribution of cosmic ray sources, if it is of Galactic origin, must be related to the structure of the Galaxy and the trajectories of cosmic rays. The trajectories are strongly affected by the Galactic magnetic field before reaching our solar system below the energy of about 10^{18} eV. These structures are best described by the Galactic coordinate. In this chapter, we report only the preliminary results of anisotropy as a function of the Galactic coordinate. Details of data reduction and their analyses are described in appendix E.

b) Summary of the Results for Galactic Coordinate

In Fig.34 for all showers, in Fig.35 for muon-rich showers, and in Fig.36 for muon-poor showers, the ratios of observed event number to expected one are shown as a function of Galactic latitude in case of (a) electron trigger and (b) muon trigger. And the same ratios are also shown as a function of Galactic longitude in Figs 37 ~ 39 (see appendix E). There are nothing but some weak tendencies which are not statistically significant but cannot be excluded at present. They are summarized as follows.

1) From the latitude dependence, the significant excess flux from the Galactic plane cannot be seen. On the contrary, the flux seems to be rather small relative to middle latitudes where excess flux seems to appear near $|b| \sim 30°$ at some energy region. In case of electron trigger, the flux from Galactic north pole seems to be lower than low Galactic latitudes, which is not inconsistent with muon trigger.
2) For muon-poor showers, there are three tendencies of anisotropy. One is that there seems to be higher flux from

higher Galactic latitude in the energy below 10^{16} eV. The others are that a little excess around the direction of 'spiral in' and a lower flux from the direction of anti-Galactic center can be seen particularly for energy region around 10^{16} eV.

But it must be noted here that there are non-uniformity of observation time in right ascension which is as large as 2.5 % at maximum and in the phase between about 200° and 300° in R.A. observation time is systematically lower than in other phase. When we examine the distribution of flux in Galactic coordinate, normalization of observation time is not carried out, so this gives rise to the reduction of flux from the corresponding Galactic coordinate with l = 30° ~ 90° and b = 0° ~ 90° . It is the direction of Galactic plane and also the direction of spiral in.

Some directions in the Galactic coordinate are impossible to observe from the northern hemisphere. This causes a very poor statistics for various interesting directions, for examples near Galactic center, necessitating more accumulated data than the analysis in the equatorial coordinate.

CHAPTER X . DISCUSSION

X -1. Comparison with Other Experiments

The principal results of other measurements for anisotropy have already been described in chapter II and summarized in Figs 1 and 2. In this section, the present results are compared with them. In Figs 40 and 41, we re-present our results of first and second harmonics with the results summarized in Figs 1 and 2 respectively. Though the statistical significance of almost all data points at above 10^{14} eV except for some points is not so high, we examine the general tendencies of the energy dependence of anisotropy.

For the first harmonic, both the amplitude and the phase at energy of 6×10^{14} eV, are consistent with ones inferred by extending the data of Daudin et al.(1956) and Delvaille et al. (1959) in the lower energy region.

In the energy region of 10^{15} eV the phase of the maximum flux is in good agreement with others around 300° in R.A., which is in accordance with the extrapolated value from the phases in the lower energy regions. The amplitude of the present result is a little higher than other experiments particularly for muon trigger. However, if we could ignore the data of the lowest energy bin of common trigger as mentioned in chapter IX , we do not think the discrepancy is serious considering the degree of statistical significance for both electron trigger and muon trigger in this region.

When we look at the whole energy region below 10^{17} eV, the amplitude appears to increase with energy above 10^{14} eV and is consistent with each other, though the ambiguity is remained. However our results appear to indicate the constant phase over two decades of energy region. No such result has reported until present time.

Above 10^{17} eV, the rapid change of phase from about 200°

to 60° through 360° is a prominent feature of the world data as seen in Fig.40(b). The present result shows no such phase-change particularly in case of muon trigger. It may be explained by the difference of trigger bias between electron trigger and muon trigger mentioned in chapter Ⅸ. However unfortunately, the statistics of ours in this energy region is poor, so we cannot discuss anymore.

For the second harmonic, at the energy of 6×10^{14} eV, the phase of maximum flux is in good agreement with the result of Daudin et al.(1956) and the phase is the same as one at 10^{13} eV level. But the amplitude is about four times larger than their data. At present it is not clear what is the cause for the difference between their results and ours, and it is the problem to be solved in future. However, from the point of view of stable operation, our result can be thought to be reliable because the trigger efficiency of our muon detectors is very stable.

At above 10^{15} eV, though significance of the results is poor, the maximum phase for muon trigger is roughly consistent with other experiments such as Murakami et al.(1985) which is probably the most reliable report at 3×10^{15} eV region at present, Daudin et al.(1956) for below 10^{16} eV, and Haverah Park, Yakutsk for above 10^{17} eV. This is also not inconsistent with for electron trigger within error. However considering the poor statistical significance, a definite claim at the energy above 10^{16} eV cannot be made for the second harmonic at present.

Unfortunately, there have been very few preliminary observations as a function of biased composition such as the N_μ / N_e ratio here analyzed. It is to be emphasized that ours is the first observation with a considerably good statistics.

Present result for muon-rich showers does not appear to support earlier results of Chatterjee et al.(1968), Hasegawa et al.(1962) and so on which report 'bright region' between

90° and 225° and 'dark' region between 225° and 315° in R.A.. One example of them is presented in Fig.42, which clearly shows such characteristics. Their selection of muon-rich showers is done by muon density and the number of selected events is very small, at most 220 events, and the fraction is about 10 % of all showers. In contrast to them, our muon-rich showers are selected by the ratio of total muon size to total electron size and the number of selected showers is 25,610 events for muon trigger and 41,682 events for electron trigger, and the fractions are about 35 % and 13 % respectively. The quality of present data is by far better than other ones and accordingly the statistical reliability seems to be higher than them.

Previously, we reported for muon-rich showers to be preferential from the direction of about 230° in R.A. in the energy region of 10^{15} eV to several times 10^{16} eV (Kifune et al. 1986b). However present results show the maximum phase being 243° ± 34° with k = 1.46 for electron trigger and 199° ± 45° with k = 0.82 for muon trigger in the same energy region, phases of which are not inconsistent with previous results but their significance is not so high.

For muon poor showers, for example, Blake et al.(1975) report the result of harmonic analysis, which shows 6.3 ± 9.6 % for first harmonic amplitude and 189° ± 87° in R.A. for its maximum phase for lower muon density events of the fraction 10 % of total showers. This phase is exactly opposite to the present result below 3.2×10^{16} eV. However, Fig.43 quoted from their paper shows clear second harmonic variation with peak phase of about 0° and 180° , which is in good agreement with present data.

By setting more severe criteria as muon-poor showers, attempts to select the showers produced from primary gamma-ray are carried out by some groups, such as Chacaltaya group and Akeno group. We have selected the very muon-poor showers whose

N_μ / N_e ratio is less than 0.001 corresponding to about 3 % of average ratio and analyze their periodicity for Cyg X-3 well known as an active point sources in other wave lengths. In this way, we have found the evidence of detection of ultra high energy gamma-ray (Kifune et al. 1986a). On the other hand, Kamata et al.(1968) obtained the upper limit of diffuse component of UHE gamma-rays by selecting low muon density event. To look for such anisotropy of diffuse gamma-ray by selecting very muon-poor showers is now under way and can be promising in future.

XI -2. Comparison of Some Models with Observed Anisotropies

a) Contribution of C-G effect

When the C-G effect is a dominant origin of anisotropy, the amplitude and phase should be independent of energy and composition if their confinement volume is the same.

In the energy range from 10^{15} to 10^{17} eV, the constant phase around 300° in R.A. suggests the possibility of such effect caused from the Galactic rotation or the motion relative to local star. However observed amplitude is several times larger than expected one, and rejecting the data of lowest energy bin of common trigger, there is a tendency of increasing amplitude with energy. And no such constancy of phase is observed for muon-rich nor muon-poor showers. Therefore it is difficult to consider anisotropy mainly due to C-G effect above 10^{15} eV. Furthermore, observed maximum phase indicates that less portion of cosmic ray is extragalactic origin even if it contributes because of the inconsistency between the expected direction and the observed one.

b) Attempts to explain the maximum phase by the arm structure

When we carry out the harmonic analysis in sidereal time, the maximum phase near observed one is able to be predicted

also from the axial symmetric anisotropy along the Galactic arm (see chapter Ⅲ and appendix B).

If there is a cosmic ray flow toward the spiral out, we can find maximum phase of first harmonic around 315° in R.A. (f_1^1 component). Otherwise even if there are flows toward both directions along the spiral arm, we can also find maximum phase of first harmonic around 315° in R.A.(f_2^1 component) as well as that of second one around 135° and 315° (f_2^2 component).

At energy of $10^{14.8}$ eV, the observed maximum phase of first harmonic is consistent with both above models. However the second harmonic phase is around 90° which is not consistent with them. In order to make the observed maximum phase of both first and second harmonics consistent with axial symmetric anisotropy, it should be assumed that the direction of symmetrical axis of cosmic ray flow is about from l = 50° toward l = 230° (b = 0°). By Vallee and Krongberg (1973, 1975), this direction coincides with the local field closed to the solar system associated with Loop I . Considering the Larmor radius of about 0.18 pc at this energy region, this agreement is not unexpected, but rather reasonable.

Above 10^{15} eV, the flow toward spiral out and the flows of both directions along the arm can explain the observed maximum phase of first harmonic. Though significance of the second harmonic anisotropy is very low, a result of observation at southern hemisphere shows the reverse phase behavior of first harmonic around 10^{16} eV (Gerhardy and Clay 1983). This indicates that the contribution of f_2^1 component appears, that is, both directions flow of cosmic rays along the spiral arm is a dominant cause of anisotropy of cosmic ray flux around this energy region.

It should be noted here that these cosmic ray flows along the spiral arm come from the anisotropy of pitch angle distribution and it is caused by not only the distribution of

cosmic ray sources but also the time variation of production rate of cosmic rays.

If the excess from the Galactic plane is assumed instead of the axial symmetric anisotropy along the arm, the maximum phase of second harmonic is expected around 100° (and 280°), which is well consistent with observed one in the energy between $10^{14.8}$ eV and 10^{17} eV.

c) Attempts to explain the energy dependence of anisotropy

In Fig.44, we again show the expected energy dependence of the first harmonic amplitude by some models together with the observed amplitude. It must be noted here that the observed data and our predictions (see next section) are the projected values on the equatorial plane but the other predictions are not so.

Anisotropy caused by density gradient of cosmic ray in the spiral arm with assumption described in chapter Ⅲ less contributes to the observed anisotropy, because there is a large discrepancy of the energy dependence of amplitude, even though observed maximum phase is able to be explained by this mechanism.

Models by Bell et al.(1974) and Giler (1983) explain the amplitude in the energy region about $10^{14} \sim 10^{16}$ eV, but the former prediction breaks down above 10^{17} eV, and the latter also cannot explain the experimental results either below 10^{14} eV and above 10^{16} eV. In addition, neither of predicted maximum phases from each model agrees with observed one.

MHD turbulence model by McIvor (1977) also explains the observed amplitude below 10^{17} eV well, but above 10^{17} eV predicted amplitude becomes higher than observed. Moreover it cannot explain the weak energy dependence of maximum phase below 10^{15} eV.

Dynamical halo model is roughly consistent with the lower values of the energy dependence of amplitude, however this

model predicts constant maximum phase which does not agree with observed one below 10^{14} eV.

In the leaky box model, when the value $\delta = -0.7$ is taken as the power of rigidity dependence on the path length, expected anisotropy is far from observed one and this model can be rejected. As shown in Fig.44, taking the value of 0.3 as δ seems roughly to explain observed energy dependence of the amplitude. However this model cannot predict the maximum phase.

Hillas attributes the energy dependence of amplitude to the leakage time. However nothing can be predicted about the energy dependence of maximum phase by this.

Summarizing above discussions, some models succeed in explaining the observed amplitude of the first harmonic in some energy regions, though the dispersion of data is so large that it is not easy to argue for and against each model from this figure. However, the models which can explain those in the wide energy range are limited, for example, by Blandford and Ostriker (1980) (LB3) and by Owens and Jokipii (1977) (DH). But neither of them cannot predict the observed energy dependence of maximum phase. One possibility to avoid this problem is to consider two or more mechanism in the different energy regions. But it is difficult to make models agree with both observed amplitude and maximum phase even if any combinations of them are taken.

X -3. Attempt of Interpretation by Diffusion Model

a) Calculated results of our diffusion model

Assuming the primary cosmic ray to be proton, we try to explain the observed anisotropy of arrival direction by diffusion model. The procedures to set up and solve the diffusion equation and to find the predicted anisotropies are described in appendix F. Here we present only the results.

Some examples of parameters sets which can predict

approximately the observed energy dependence of the amplitude are presented in Table 11. And predicted amplitudes from each model are shown in Fig.45(a) with the observed data (The predicted ones by models U and A are shown also in Fig.44 for comparison with other models.). Considering the ambiguities of the data, together with the effect of trigger bias at 10^{15} eV, it seems that the observed data are well explained by those any models above 6×10^{14} eV.

However, as shown in Fig.45(b), some models of them do not succeed in explaining the energy dependence of the observed maximum phase below about 10^{17} eV. Model U, where cosmic ray sources are assumed to distribute uniformly in the disk and low Galactic halo is assumed, seems to be the best to explain the observed data below several times 10^{17} eV. On the other hand, considering the continuity from low energy region, the tendency of energy dependence of the prediction from model A which does not fit to the observed one very good seems to be better than others. More discussion of them will be done in the following sub section.

b) Discussion of our models with observed anisotropies

The assumptions which are common to model R, model E and model C are that the source distribution is biased to the inner Galaxy rather than the outer Galaxy and the direction of magnetic field is toward the spiral in. These assumptions and the sets of parameters of their models seem to be very reasonable. But because the energy dependence of maximum phase below 10^{17} eV cannot be explained by their models, they should be rejected as far as we assume the uniform and the concentric circular magnetic field.

In model U, the disk height is assumed to be 100 pc which is as high as the height of HI distribution (Burton 1976). And the halo height is assumed to be 1 kpc which is lower than the value taken usually, however it is not unreasonable value

(for example, Hayakawa (1979) suggests the dynamical halo of about 2 kpc thickness).

On the other hand in model A, the disk height and the halo height are assumed to be 1 kpc and 10 kpc, respectively. By the results of RM of radio sources, the thickness of the magnetoionic plane of the Galaxy is estimated to be about 1.4 kpc (Simard-Normandin and Kronberg 1980, Inoue and Tabara 1981). In the Galactic halo, the strength of magnetic field is little known and is only conjectured to be weaker than in the disk by more than one order. Therefore the values of these parameters in this model can also be regarded to be reasonable at present.

We further consider the propriety of the above two models. The energy dependence of diffusion coefficients in the disk assumed in the two models are shown in Fig.46, together with those used in other models where particles are assumed to be protons. In this figure, it is clear that our assumed values are not so peculiar, rather close to the values by McIvor (1977) and Ormes (1983). Scattering mean free path is about 3 pc at 10^{15} eV and about 30 pc at 10^{17} eV in both models, which tend to be a little smaller than astrophysically reasonable values of 10 pc to 100 pc (Heiles 1976) but roughly not inconsistent. In this figure, the value of $(1/3)\rho c$ (where ρ is the Larmor radius of proton in the magnetic field of about 3 μ G strength) is presented by dashed line.

As above mentions, the values of parameters used in model U and model A seem to be reasonable, and the observed anisotropy seems to be well explained both by them. However, there are some problems.

In model U, the first problem is the bad continuity between the predicted phase above 10^{14} eV to the observed one below 10^{14} eV, though we may be able to avoid the difficulty by another mechanism of anisotropy. The second problem, which is more severe, is the assumption of the uniform source

distribution. In fact, the overall forms of radial distribution of several constituents of the Galactic disk, such as H_2, HII , SNR, and γ -radiation are quite similar (Burton 1976) which have a peak of radial distribution around 5 kpc and decrease both inner and outer sides of it. Considering pulsars or SNRs are the highly probable candidates of Cosmic ray sources, this inconsistency cannot but make us recognize the failure of this model to explain the observed anisotropy.

On the other hand, in model A, we assume the direction of magnetic field toward spiral out, which cannot be rejected but is very unreasonable at present status. In spite of ambiguity, the possibility of the field direction toward spiral out near the solar system is less than 1 % from the astrophysical informations (Tabara 1986). So, This model should also be rejected here.

In the diffusion model, density gradient of cosmic rays is the prime factor for the anisotropies. The observed anisotropy should be explained by the combination of simple diffusion caused by density gradient of cosmic ray with the gyro-motion around the magnetic field. In Fig.47, we show the calculated density gradient at near the solar system in models U and A. There is a remarkable difference between two models. In model U the gradient is approximately normal to the Galactic plane. In model A, on the other hand, it is toward the Galactic center. Considering these facts, together with the tendency of predicted energy dependence of maximum phase shown in Fig.45(b), we can find that we inevitably confront with the contradiction of the assumption between the direction of the Galactic magnetic field and the source distribution, as far as we take other parameters reasonably. The results assuming the heavy particles instead of protons are also the same. In this point, even though there is large degree of freedom to select parameters, we cannot but say that the diffusion model as

treated here do not succeed in explaining the observed anisotropies. It is likely to need to consider the local structure of magnetic field and source distribution, such as Loop I and so on.

Lastly, the following is noted. We ignore the transverse component of diffusion coefficient in our models except for the process of determination of the arrival direction. Such treatment is not permitted a priori. In fact, drift motion of cosmic rays arises at the boundary of disk and halo, and may affect the diffusion process as the apparent sources (such effect may be not so large). If we treat the diffusion model more strictly, the mathematical treatment is very complicated and it is difficult to solve diffusion equation analytically.

X -4. Anisotropies of Selected Showers and their Composition

a) muon-rich showers

If the maximum phase for muon-rich showers is different from all showers as seen in Fig.32(b), it may suggest the possibility of two or more components of primary cosmic rays in that energy region. And if the observed muon-rich showers are heavy primary component such as iron, together with the results of direct detection experiments showing proton dominant composition below 10^{14} eV/nucleus, its maximum phase should be consistent with the phase observed at lower energy region corresponding to the same rigidity of proton.

Observed maximum phases of both the first and second harmonics for all showers at energy of $(3.2 - 10) \times 10^{15}$ eV are different from the results of lower energy. This suggests the possibility that heavy primary cosmic ray of different origin is getting dominant with energy below 3.2×10^{16} eV as is discussed by Kifune et al.(1986c), and also supports the interpretation of bump by Takahashi et al.(1986). So we will discuss these points more detail.

Figure 32 shows the maximum phase of first harmonic in three energy bins of the muon trigger (the result of electron trigger is also shown in figure (b)) as a function of the fraction of selected events biased to muon-rich showers by the criteria of N_μ / N_e. In these figures, the change of phase with the fraction of selected muon-rich events can be seen at only one energy bin of a half decade, at the energy bin of (3.2 - 10) $\times 10^{15}$ eV, which roughly corresponds to the energy region of existing a bump of primary energy spectrum of cosmic rays. This result suggests that if heavy components are dominant in this region, they might have rather sharp peak of energy spectrum. So next, we pay attention to this energy region.

The amplitudes of first harmonic in this energy region for the case of muon trigger are shown in Fig.48 as a function of the fraction of selected muon-rich events, as Fig.32.

Even though the error is large, there seems to be a minimum around the fraction of about 60 % and plateau below the fraction of about 30 % of muon triggered events respectively. It is found that this minimum corresponds to the criteria of the phase change in Fig.32(b), and at this point, their composition may also change . Following to Kifune et al. (1986), and assuming two components model, plateau region consists of only heavy component, and the amplitude of plateau indicates that of heavy component. At the criteria of 60 %, the contribution of heavy component to the all shower's anisotropy is expected to be comparable to the proton contribution. Therefore, if the statistics were enough, we could estimate the the fraction of heavy component and the amplitudes of both proton and heavy components respectively in accordance with the procedure described in appendix G. But here, statistics is so much poor that we cannot discuss above quantities meaningly.

If we take qualitative tendency as it is, it indicates that heavy component has a different origin from proton, and

plays an important role in this energy region for such as the bump of energy spectrum, phase change of anisotropy, and so on. However at present, it may be reckless to claim it because statistical significance is very poor and also because we cannot find definite change of N_μ / N_e relation (Hara et al. 1983). In order to discuss the primary composition meaningly in view of these points, at least several times as much as the data here analyzed are needed.

Lastly, we shortly mention our diffusion model in connection with heavy component. By the diffusion model treated above, neither of observed amplitude and phase with their energy dependence can be explained, even if heavy particles such as iron are assumed.

b) Muon-poor showers

On the other hand, it is considered that the primary composition selected by muon-poor showers is almost proton or gamma-ray. Then if the proton is dominant in the considered energy region and the amplitude of anisotropy of other components is not so high, the anisotropy of muon-poor showers should be almost the same as the one of all showers.

In Fig.49, we show the amplitude of first harmonic for muon poor showers in the energy region of (3.2 - 10) $\times 10^{15}$ eV as a function of biased criteria of N_μ / N_e, where events whose N_μ / N_e ratios are less than the criteria are selected. From this figure, we can estimate the lower limit of proton components in the electron triggered events and its amplitude. Obtained results are consistent with the results from muon-rich showers mentioned above, but the statistics is very poor.

Here as we select muon poor events by weak criteria, the possibility of γ -ray may be small, and no data also support it positively. We will give a little mention about it in the next section.

X -5. Anisotropy on Galactic Coordinate

Following the diffusion model treated in this article, excess from southern direction of Galactic plane is expected. But, as mentioned in chapter IX and shown in Fig.34, no such excess can be seen. Instead as shown in Fig.34, there is a tendency of the excess from around b = 30° and decrease as angular distance along the circle of Galactic latitude. However considering the remained problems about the correction for the non-uniformity of observation time, it is difficult to say definitely whether there is an excess from southern direction or not.

As mentioned above, the results of harmonic analysis for second harmonic in the energy of 6×10^{14} eV is well explained by the axial symmetric anisotropy along the local field line or the excess from Galactic plane, which give rise to the maximum flux from about 100° and 280° in R.A.. Unfortunately, the data of this energy region cannot be analyzed on their distribution of arrival direction for Galactic coordinate. In the energy region above 10^{15} eV, as shown in Fig.34, there can be seen no evidence of excess from Galactic plane. In addition to them we check longitude dependence of anisotropy and find no definite excess from any directions such as SI.

For muon poor showers, as shown in Fig.39, a little excess is seen at the direction of SI on the plane. And the tendency of smaller flux at Galactic plane than at high Galactic latitude is also noted. Possibilities are considered about the effect of local magnetic field such as reverse direction, and the γ -ray effect predicted by Bhat et al.(1986). But definite conclusions cannot presented in present status.

CHAPTER XI . CONCLUSION

In the case of rate trigger, where the median energy of observed showers is about 6×10^{14} eV, the following significant anisotropies are observed:

- The maximum flux phase of first harmonic is 330° ± 21° . Its amplitude is 0.23 ± 0.09 %, and the chance probability of the value is 2.8×10^{-2}. For the second harmonic, the amplitude is 0.30 ± 0.09 % and the phase is 92° ± 8° . This excess is more than 3σ and its chance probability is 2.6×10^{-3}.

Cosmic ray flows along the local field line toward l = 50° , b = 0° and l = 230° , b = 0° explain the observed anisotropies, especially for the results of second harmonic, very well. However, the possibility of the excess from Galactic plane for this energy region cannot be rejected.

Most significant anisotropies obtained by the present experiment in the energy range between 10^{15} eV and 10^{18} eV are as follows:

- In the energy range from 1×10^{15} to 3.2×10^{16} eV for all showers in case of electron trigger, the maximum phase of first harmonic is 294° ± 19° in R.A.. Its amplitude is 0.80 ± 0.26 %, and its chance probability is 9.0×10^{-3}.

  In the energy range from 1×10^{16} to 1×10^{17} eV for all showers in case of muon trigger, the maximum phase of first harmonic is 313° ± 20° in R.A.. Its amplitude is 2.13 ± 0.73 %, and the chance probability is about 1.45×10^{-2}.
- For the muon-poor showers whose N_μ / N_e ratios are less than 0.01. there is an evidence of significant anisotropy in the second harmonic. The phase of its maximum flux is 166° ± 8° in R.A. in the energy range of 1×10^{15} eV to 1×10^{17} eV. The amplitude is 4.62 ± 1.24 %, and its chance probability is 9.4×10^{-4}.

The excess from the direction normal to the Galactic plane can be also conjectured from the observed muon-poor showers data in the energy region above 10^{15} eV.

In other energy regions for each trigger and for each selection of showers, there is no significant anisotropy, and in some energy regions only upper limits are obtained.

Cosmic ray flows along the Galactic arm toward $l = 90°$, $b = 0°$ and $l = 270°$, $b = 0°$ for above 10^{15} eV, explain the observed anisotropies well. Such direction is nearly parallel to the spiral arm.

There are some differences on maximum phase and amplitude between all showers and muon-rich showers. This suggests that some portions of primary cosmic rays are heavy components around 10^{16} eV. Composition is roughly estimated but statistical reliability is not enough. From the comparison of the energy dependence of maximum phases in the same rigidity region, the possibility of the different origin and/or different propagation among them is suggested. However, more arguments are open to the future study.

APPENDIX A. Harmonic Analysis

We consider the data set of N, where the phase of arrival direction of i-th event is ϕ_i (i = 1,2,...,N). The m-th harmonic amplitude r_m and its maximum phase ϕ_m are given by the following well known equations.

$$r_m = (a^2 + b^2)^{1/2},$$

where

$$a = (2/N) \sum_{i=1}^{N} \cos m\phi_i, \quad b = (2/N) \sum_{i=1}^{N} \sin m\phi_i,$$

and

$$\phi_m = [\tan^{-1}(b/a)] / m, \quad (0 \leqq \phi \leqq 2\pi /m),$$

respectively.

The probability of obtaining fractional amplitude greater than r by chance is given by

$$P(> r) = \exp (-k), \quad k = (r^2 N) / 4.$$

and the magnitude of errors estimated for amplitude and phase are as follows (Linsley 1975),

$$\Delta r_m = r / (2k)^{1/2},$$
$$\Delta \phi_m = [1 / (2k)^{1/2}] / m.$$

APPENDIX B. Formula of Cosmic Ray of Axial Symmetric Anisotropy

Nagashima (1971) gives the equation of axial symmetric anisotropy. Following him, we define the intensity of cosmic ray incident upon a point O from a direction JO in Fig.50 as following equation,

$$J(R,\chi,\Lambda) = J(R) + \delta J(R,\chi,\Lambda),$$

where R is rigidity of cosmic ray, χ and Λ are polar and co-declination of incident direction. Variational intensity distribution $\delta J/J$ is expanded into a series of Legendre function as follows:

$$\begin{aligned}\delta J/J &= F(\chi) \\ &= \sum_{n=0}^{\infty} F_n(\chi) \\ &= \sum_{n=0}^{\infty} \eta_n P_n^0(\cos\chi).\end{aligned}$$

where $F(\chi)$ is space distribution of cosmic rays. Next, the above spatial distribution is transformed into equatorial coordinate expression as follows:

$$\begin{aligned}F(\chi) &= \sum_{n=0}^{\infty} F_n(\chi) = \sum_{n=0}^{\infty} \{ \sum_{m=0}^{n} f_n^m(\chi) \} \\ &= \sum_{n=0}^{\infty} \sum_{m=0}^{n} \eta_n P_n^m(\theta_R) P_n^m(\theta_J) \cos m(\alpha_J - \alpha_R)\end{aligned}$$

where α_R, θ_r are right ascension and co-declination of reference axis (OR) and α_J, θ_J are those of incident direction (OR).

When m = 0, any diurnal variation is not produced, and components f_1^1 and f_2^2 are the terms responsible for usual diurnal variations. On the other hand, component f_2^1 produces a new type of diurnal variation.

APPENDIX C. Anisotropy caused by density gradient and magnetic field

The amplitude of anisotropy caused by density gradient of cosmic ray and uniform magnetic field is given about $\rho \times | \nabla n | / n$. This means that it depends on cosmic ray energy if their composition does not change with energy. Sakakibara (1965) calculates the energy dependence of the amplitude in this case. Assuming the length of arm is infinite, the distribution of cosmic ray sources is uniform in the arm and the distribution of cosmic ray particles does not depend on time, the diffusion equation on the plane normal to the arm axis is expressed as follows:

$$K_{\perp} \left[\frac{\partial^2}{\partial r^2} + \frac{1}{r} \frac{\partial}{\partial r} + \frac{1}{r^2} \frac{\partial^2}{\partial \phi^2} \right] n(r) + Q = 0,$$

where $K_{\perp}$ is diffusion constant in $cm^2 s^{-1}$, $n(r)$ is the density of cosmic ray particles in cm^{-3}, r is the radial distance from the center of arm in cm and Q is the source flux per second. The solution of this equation with the boundary condition of $n(r_o) = 0$ and the continuous condition of $n(0)$ being finite is given by

$$n(r) = \frac{Q}{4K_{\perp}} (r_o^2 - r^2),$$

where r_o is the radius of arm.

The amplitude of anisotropy perpendicular to the arm is expressed as follows:

$$\begin{aligned} a_{\perp} &= \rho \, [(dn/dr)/n] \\ &= \frac{2\rho}{r_o} \frac{R}{1 - R^2}, \end{aligned} \qquad \text{(C-2)}$$

where $R = r/r_0$.

APPENDIX D. Transformation from Equatorial coordinate to Galactic coordinate

The transformation from the equatorial coordinate to the Galactic coordinate is done by using following equations.

$$\begin{aligned} \cos b \cos(l-l_0) &= \cos\delta \cos(\alpha-\Omega) \\ \cos b \sin(l-l_0) &= \sin\delta \sin i + \cos\delta \sin(\alpha-\Omega) \cos i \\ \sin b &= \sin\delta \cos i - \cos\delta \sin(\alpha-\Omega) \sin i \end{aligned} \qquad \text{(D-1)}$$

where l and b are Galactic longitude and latitude respectively, $l_0 = 33.^\circ 0$ and $\Omega = 18^h49^m$ are the Galactic longitude and right ascension of ascending node for galactic plane on equatorial plane respectively, and $i = 62.^\circ 60$ is the angle between equatorial plane and Galactic plane, which are recommended by IAU (International Astronomical Union) in 1959.

APPENDIX E. Anisotropy in Galactic Coordinate

E-1. Data Reduction

One and serious difficulty for investigation of the anisotropy on Galactic coordinate is non-uniformity of observational efficiency for Galactic latitude and/or Galactic longitude because the observation is carried out at fixed place and we scan the sky by making use of rotation of the Earth which is uniform for right ascension in fixed declination band but not for Galactic coordinate. It depends on zenith angle dependence of detection efficiency which is very difficult to calculate accurately because it is a complex function of shower attenuation and array response. The method

used by Haverah Park group (Lloyd-Evans 1982) is applied.

Assuming the ideal condition of equal operation time for right ascension, the efficiency of observation for each α -δ cell is the same at fixed declination band because the relation of the zenith angle and the effective time for each right ascension is the same. So firstly we calculate the expected event number in each cell by averaging over the right ascension for each declination band. And the values of α and δ in equatorial coordinate at the center of each cell are transformed to the values of l and b in Galactic coordinate according to the equations (D-1) (see appendix D).

Lastly, the transformed values l and b are sorting to the cellular division with Δ l = 10° and Δ b = 10° , and the observed event number and expected one are summed up respectively in each cell.

When the Galactic latitude dependence is examined, the observed number and the expected number are summed up respectively over the whole Galactic longitude and the ratio R(b) in each latitude bin is calculated according to the following equation,

$$R(b) = \sum_{l} N_{obs}(l,b) \; / \; \sum_{l} N_{exp}(l,b),$$

where $N_{obs}(l,b)$ and $N_{exp}(l,b)$ are observed and expected number in each cell. On the other hand when the Galactic longitude dependence is examined, by the same procedure as above, the ratio R(l) is calculated as follows,

$$R(l) = \sum_{b} N_{obs}(l,b) \; / \; \sum_{b} N_{exp}(l,b),$$

where summation of b is carried out over $|b| < 30°$. One of which reason is to exclude the contaminated data caused by large difference of the field of each cell for Galactic coordinate and equatorial one because at high latitude the

solid angle of each cell is far smaller than the original α -δ cell according to cos| b| , and another is to investigate the distribution along the Galactic plane.

E-2. Anisotropy on Galactic Latitude b

The calculated ratios R(b) for each energy bin with the width of a half decade together with their sum are shown as a function of b in Fig.34 for all showers, in Fig.35 for muon-rich showers by (a) electron trigger and (b) muon trigger, respectively, and in Fig.36 for muon-poor showers by electron trigger.

Assuming the linear relation,

$$R(b) = c_{bo} + c_{b1}\, b,$$

where c_{bo} and c_{b1} are constants, the least square fitting is carried out for three regions, for $b \leqq 0°$, for $b \geqq 0°$ and for $-90° \leqq b \leqq +90°$, respectively. The obtained parameters are presented in Table 12 with the results of χ^2 test for discrepancy from uniform distribution, and the gradient c_{b1} are shown also in Fig.51 as a function of energy where closed circles indicate the case by muon trigger and open circles indicate by electron trigger.

E-3. Anisotropy on Galactic Longitude l

In Figs 37~ 39, the ratios R(l) are plotted as a function of Galactic longitude l for each energy bin of a half decade. First, we check the consistency with isotropic distribution between $l = 0°$ and $l = 180°$ by using χ^2 test. where because of very poor statistics caused by excluding the data for $|b| \leqq 30°$, the data from $l = 180°$ to $l = 360°$ are not used. The results are presented at first column in Table 13.

If there is anisotropy related to the direction of Galactic center or anti Galactic center, we expect the

positive or negative gradient in Figs 37~39. So we try to fit the data to the linear relation,

$$R(l) = c_{10} + c_{11}\, l, \qquad \text{for } 0° \leqq l \leqq 180° ,$$

and the best fitting parameters c_{10} and c_{11} are presented at second and third column in Table 13.

On the other hand, if there is anisotropy related to the direction of spiral arm of Galaxy, we expect roughly the first and/or second harmonic distribution of arrival direction for Galactic longitude. Since the data between l = 180° and l = 360° are very poor as mentioned above and cannot use here, We check the anisotropy for Galactic longitude conventionally by analyzing first harmonic component for l = 0° to 180° , which corresponds to assume second harmonic distribution of cosmic ray flux. The results are presented at columns from fourth to sixth in Table 13.

APPENDIX F. Diffusion Model

F-1. Diffusion Equation

First of all, the whole our Galaxy which consists of "disk" and "halo" is taken to be the diffusion space. Here, for simplicity, it is assumed that the Galaxy consists of three layers of disk (or low height cylindrical) shape region which are symmetrical about the Galactic plane, as shown in Fig.52. The magnetic field in the Galaxy is assumed to be parallel to the Galactic plane and concentric circular field (Inoue and Tabara 1981). Cosmic rays being assumed to be protons are produced constantly in time in the Galactic disk which has a thickness of 2b with a radius of R, and diffuse due to scattering by irregularities of magnetic field. Diffusion coefficients are constant with K_d and K_h in the disk and halo respectively. At the boundary between disk and halo,

cosmic rays come and go freely, and at the outer boundary of the Galaxy, they flow out intergalactic space freely. In addition to the leakage, nuclear interaction of cosmic rays with interstellar gas is considered. Interstellar gas is assumed to be distributed uniformly only in the disk. The sources of cosmic rays are also assumed to be distributed only in the disk symmetrically about the axis of Galactic rotation and uniformly about the direction normal to the Galactic plane.

Now we take the axis of Galactic rotation as z axis and r as the distance from z axis, and take cylindrical coordinate (r, ϕ, z) where Galactic plane coincidence with the plane of $z = 0$. By the assumption of constant activity of sources in time, we can consider the stationary case. And by the assumption of the symmetrical source distribution, azimuthal dependence of the number density of cosmic ray particles $N(r, \phi, z)$ does not exist and is neglected. So the equations which should be solved can be expressed as follows,

$$K_d \left\{ \frac{\partial^2}{\partial r^2} + \frac{1}{r}\frac{\partial}{\partial r} + \frac{\partial^2}{\partial z^2} \right\} N(r,z) - v\sigma n N(r,z) + S(r,z) = 0 \quad \text{for } |z| \leqq b \qquad \text{(F-1a)}$$

$$K_h \left\{ \frac{\partial^2}{\partial r^2} + \frac{1}{r}\frac{\partial}{\partial r} + \frac{\partial^2}{\partial z^2} \right\} N(r,z) = 0 \quad \text{for } b \leqq |z| \leqq h, \qquad \text{(F-1b)}$$

where $S(r,z) = S(r)\theta(b - |z|)$ the number of cosmic ray yielded in unit time and unit volume, n the density of interstellar gas, $v = c$ the velocity of cosmic ray particles, and σ the total cross section of inelastic interaction of cosmic ray particles with interstellar gas. The first term of left side of the equation (F-1a) and the left side of (F-1b) are the terms about diffusion, the second term of left side of (F-1a) is the term about the interaction with interstellar gas and the third term of it is the cosmic ray production term.

We must solve these equations under the boundary conditions;

$$N(R,z) = 0 \qquad \text{for } |z| \leqq h \qquad \text{(F-2a)}$$

$$N(r,\pm h) = 0 \qquad \text{for } r \leqq R \qquad \text{(F-2b)}$$

and the continuity conditions of the number density and flux of cosmic rays on the boundary of disk and halo;

$$N_{(disk)}(r,\pm b) = N_{(halo)}(r,\pm b) \qquad \text{(F-3a)}$$

$$K_d \left.\frac{\partial N_{(disk)}}{\partial z}\right|_{\lim_{\varepsilon\to 0} z=\pm(b-\varepsilon)} = K_h \left.\frac{\partial N_{(halo)}}{\partial z}\right|_{\lim_{\varepsilon\to 0} z=\pm(b+\varepsilon)} \qquad \text{(F-3b)}$$

F-2. The solution of Diffusion Equation

N(r,z) and S(r,z) are expanded by the Fourier-Bessel series as follows,

$$N(r,z) = \frac{2}{R^2} \Sigma_k \frac{J_0\left(\nu_k \frac{r}{R}\right)}{J_1^2(\nu_k)} N_k(z)$$

$$N_k(z) = \int_0^R r\, N(r,z)\, J_0\left(\nu_k \frac{r}{R}\right) dr. \qquad \text{(F-4)}$$

$$S(r,z) = \frac{2}{R^2} \Sigma_k \frac{J_0\left(\nu_k \frac{r}{R}\right)}{J_1^2(\nu_k)} S_k(z)$$

$$S_k(z) = \int_0^R r\, S(r,z)\, J_0\left(\nu_k \frac{r}{R}\right) dr. \qquad \text{(F-5)}$$

The equations (F-4) and (F-5) are substituted in the equation (F-1), and we can get the following equations respectively,

$$\left[\left(\frac{\nu_k}{R}\right)^2 + \frac{v\sigma}{K_d} n - \frac{d^2}{dz^2} \right] N_k(z) = Q_k$$

for $|z| \leqq b$ (F-6a)

$$\left[\left(\frac{\nu_k}{R}\right)^2 + \frac{v\sigma}{K_d} n - \frac{d^2}{dz^2} \right] N_k(z) = Q_k$$

for $b \leqq |z| \leqq h$ (F-6b)

where J_0 and J_1 are the first kind Bessel function of zero order and first order respectively, and ν_k is the k th positive zero point of J_0. By the assumption $Q_k \equiv S_k(z)/K_d$ is independent on z.

By using the boundary conditions at $z = \pm h$ and $r = R$ (F-2) and the continuity condition at $z = \pm b$ (F-3), we can get the solutions of the equation (F-6) as follows,

$$N_k(z) = \frac{Q_k}{\lambda_k^2} \left[\frac{q \cosh(\lambda_k z)}{(K_d \lambda_k / K_h \mu_k)\, q' \sinh(\lambda_k b) - q \cosh(\lambda_k b)} + 1 \right]$$

for $|z| \leqq b$ (F-7a)

$$N_k(z) = \frac{Q_k}{\lambda_k^2} \left[\frac{e^{\mu_k(|z|-2h)} - e^{-\mu_k|z|}) \sinh(\lambda_k b)}{q' \sinh(\lambda_k b) - (K_h \mu_k / K_d \lambda_k) q \cosh(\lambda_k b)} \right]$$

for $b \leqq |z| \leqq h$ (F-7b)

where

$$\lambda_k^2 = \left(\frac{\nu_k}{R}\right)^2 + \frac{v\sigma}{K_d} n , \qquad \mu_k^2 = \left(\frac{\nu_k}{R}\right)^2$$

$$q = \exp(\mu_k(b-2h)) + \exp(-\mu_k b)$$

$$q' = \exp(\mu_k(b-2h)) - \exp(-\mu_k b).$$

So, if the r distribution of cosmic ray sources S(r) is known, the density distribution of cosmic rays can be calculated as a function of r and z from equations (F-4), (F-5) and (F-7).

However, it should be noted that the transverse component of diffusion coefficient $K_{\perp}$ is ignored here. But such treatment is not permitted a priori. In fact, drift motion of cosmic rays arises at the boundary of disk and halo, and may affect the diffusion process as the apparent sources. When the strength of the magnetic field in the halo is far weaker than in the disk, we can neglect $K_{\perp}$. But such situation cannot be assured in the halo. Therefore to neglect $K_{\perp}$ is the question point in this model. We should keep it in mind, even though above effect may not be so large,

F-3. Expected Anisotropy from Diffusion Model

a) Expected amplitude of harmonic analysis in sidereal time

Here, we consider not only the simple diffusion caused by density gradient but also the charged particle flow caused by the gyro-motion in the average magnetic field. As we assume the average configuration of Galactic magnetic field to be concentric circular, r component and z component of anisotropy are expressed as follows respectively,

$$\delta_r = -\frac{3K}{v}\frac{1}{N(r,z)}\left\{\frac{\partial N(r,z)}{\partial r} - \mathrm{sign}(B_\phi)\frac{\lambda}{\rho}\frac{\partial N(r,z)}{\partial z}\right\} \quad \text{(F-8a)},$$

$$\delta_z = -\frac{3K}{v}\frac{1}{N(r,z)}\left\{\frac{\partial N(r,z)}{\partial z} + \mathrm{sign}(B_\phi)\frac{\lambda}{\rho}\frac{\partial N(r,z)}{\partial r}\right\} \quad \text{(F-8b)},$$

where λ is a scattering mean free path, ρ is a gyro radius and $\mathrm{sign}(B_\phi)$ is the direction of magnetic field, where the direction of anticlockwise is taken as plus. ϕ component of anisotropy is not considered at present because when we assume an axial symmetric configuration the first order of anisotropy is zero.

The observable amplitude of sinusoidal sidereal variation at the geographical latitude ϕ_{obs} is given by

$$r(\phi_{obs}) = (\delta_r^2 + \delta_z^2) \cos\delta \cos\phi_{obs}$$

where r is the amplitude of first harmonic in sidereal time and δ is the declination of the direction of maximum cosmic ray flux.

b) Parameter setting

As presented in Table 10, we set the fixed values on seven parameters. Some of them are not confirmed values but taken ones are the most acceptable ones.

The disk height and the halo height are freely taken within the values of 100 pc $\leqq$ b $\leqq$ 1 kpc and 1 kpc $\leqq$ h $\leqq$ 15 kpc respectively. The energy dependence of the diffusion coefficient is assumed to be expressed as

$$K_d = \kappa (E/10^{15})^{\eta} ,$$

where E in eV. Therefore scattering mean free path λ is expressed as

$$\lambda = 3\kappa (E/10^{15})^{\eta} /v.$$

The parameters κ and η are taken as the values between 1×10^{28} cm^2s^{-1} and 3×10^{29} cm^2s^{-1}, and between 0.3 and 1.0 respectively. The diffusion coefficient in the halo are assumed to be the X times larger than K_d, where $X = K_h/K_d$ are taken to the value from 1 to 10^3. The direction of magnetic field is assumed to be toward spiral in and spiral out respectively.

Four types of distribution of cosmic ray sources are assumed. The configurations of those source functions as a

function of Galactocentric distance are shown in Fig.53. They are the distribution of SNRs (Kodaira 1974; chain line), the exponential type distribution (solid line), the Heaviside's function type (broken line) and the uniform distribution in the Galactic disk (dotted line).

APPENDIX G. Estimation of the Fraction of each Component

Here two components, proton and heavy nuclei, are assumed to be primary cosmic rays. r_p and r_H are taken as the amplitude of the first harmonic for proton and heavy component respectively, and their maximum phase ϕ_p and ϕ_H are assumed to be the exact opposite. The contribution of proton to the anisotropy for all showers assumed to be more dominant than that of heavy component. Then the first harmonic amplitude for all showers r_A is expressed as follows,

$$r_A = (1 - \zeta) r_p - \zeta r_H \qquad (G.1)$$

where ζ is the fraction of heavy component.

ξ is taken as the fraction of selected showers by N_μ / N_e which is biased to high muon contents, and r_R is taken as the amplitude of such selected showers, that is, muon-rich showers.

When $\xi = 1$, $r_H = r_A$ and maximum phase coincides with ϕ_p. As ξ decreases, r_R decreases and becomes zero at a certain transition point ξ_0, where the contribution of proton and that of heavy are comparable. At transition point, following relation

$$0 = (\xi_0 - \zeta) r_p - \zeta r_H \qquad (G.2)$$

is realized. As ξ decreases furthermore, r_R again increases but now maximum phase coincides with ϕ_H, where the contribution of heavy component is dominant. Below a certain

fraction of ξ , r_R saturates, where pure heavy components are selected and $r_R = r_H$.

From observed data, r_A, $r_R(\xi)$, r_H and ξ_0 can be obtained. So r_p and ζ are given by,

$$r_p = \frac{r_A}{1 - \xi_0}$$

$$\zeta = \frac{\xi_0}{1 - \xi_0} \frac{r_A}{r_p + r_H}$$

In the case of muon poor showers, the same method can be applied.

It is noted here that the differing relation between primary energy and shower size for different masses is not considered.

Acknowledgments

I am grateful to Professor Y. Toyoda for his guidance and continuous encouragement on this work through more than five years. I wish to thank professor T. Kifune in Institute for Cosmic Ray Research (ICR), University of Tokyo, for his valuable discussion and comment on this work and for his reading the manuscript critically. I am thankful to Professor K. Murakami for his useful suggestions and critical comments on this study.

The experimental works described in this paper are done at Akeno Observatory, ICR. It is a pleasure to Professor K. Kamata, the director of ICR, and Professor G. Tanahashi, the director of Akeno observatory, for giving me facilities for study in this field as well as for useful discussions. And I also wish to thank all members of Akeno experiments, Professors M. Nagano, T. Hara and N. Hayashida for their useful comments, Mr. H. Ohoka for his help in designing electrical circuits and development of data taking system, Mr. K. Hoji for his help in data taking, Mrs. R. Torii for her help in data analysis. and Messrs. F. Ishikawa, Y. Ohno, M. Shimizu, K. Hirabayashi, Y. Takei, K. Mesuda and K. Kobuchi for their help to maintenance and operation of EAS array.

I thank Professors K. Kobayakawa and M. Miyagaki for their reading the manuscript and critical comments on it.

My stay at ICR would not have been very pleasant and exciting without the young fellow students, Messrs. M. Teshima, Y. Matsubara and M. Mori.

The analysis was carried out with FACOM M380 at the Computer Room of Institute for Nuclear Study, the University of Tokyo.

Reference

Alexeenko, V.V.. and Navarra, G. 1985, Lettere al Nuovo Cimento, 42, 321.

Allen, C.W. 1973, Astrophysical Quantities, 3rd ed., Athlone Press., London.

Baltrusaitis, R.M., et al. 1985a, Proc. 19th ICRC (La Jolla), 2, 246.

Baltrusaitis, R.M., et al. 1985b, Ap. J. Lett., 293, L69.

Bell, M.C., et al. 1974, J. Phys. A:Math.,Nucl.Gen., 7, 420.

Bercovitch, M., and Agrawal, S.P. 1981, Proc. 17th ICRC (Paris), 10, 246.

Bhat, C.L., et al. 1986, Astron. Astrophys., 159, 299.

Blake, P.R., et al. 1975, Proc. 14th ICRC (Munich), 8, 2768.

Blandford, R.D., and Ostriker, J.P. 1980, Ap. J., 237, 793.

Boone, J., et al. 1984, Ap. J., 285, 264.

Brecher, K., and Burbidge, G.R. 1972, Ap. J., 174, 253.

Burnett, T.H., et al. 1984, Proc. Int. Symp. on Cosmic Rays and Particle Physics (Tokyo), 468.

Burton, W.B. 1976, Ann. Rev. Astron. Astrophys., 14, 275.

Chatterjee, B.K., et al. 1968, Canadian J. Phys., 46, S131.

Compton, A.H., and Getting, I.A. 1935, Phys. Rev., 47, 817.

Cutler, D. J., et al. 1981, Ap. J., 248, 1166.

Daudin, J., et al. 1956, Nuovo Cimento, Ⅲ, 1017.

Davies, S.T., et al. 1979, Proc. 16th ICRC (Kyoto), 4, 210.

Davis, L., Jr. 1954, Phys. Rev., 96, 743.

Delvaille, J., et al. 1959, Proc. Moscow ICRC (Moscow), Ⅲ, 143.

Delvaille, J., et al. 1962, J. Phys. Soc. Japan, 17, Suppl. A-Ⅲ, 76.

Dorman, L.I., et al. 1984, Astrophys. Space Sci., 109, 87.

Dzikowski, T., et al.1983, J. Phys. G:Nucl.Phys., 9, 459.

Eames, P.V.J., et al. 1985, Proc. 19th ICRC (La Jolla), 2, 254.

Edge, D.M., et al. 1978, J. Phys. G:Nucl.Phys., 4, 133.

Efimov, N.N., et al. 1983, Proc. 18th ICRC (Bangalore), 2, 149.

Elliot, H. 1979, Proc. 16th ICRC (Kyoto), 14, 200.

Fenton, A.G., and Fenton, K.B. 1976, Proc. Int. Cosmic Ray Simp. (Tokyo), 313.

Gerhardy, P.R., and Clay, R.W. 1983, J. Phys. G:Nucl.Phys., 9, 1279.

Giler, M. 1983, J. Phys. G:Nucl.Phys., 9, 1139.

Gombosi, T., et al. 1975, Proc. 14th ICRC (Munich), 2, 586.

Greisen, K. 1956, Progress in Cosmic Ray Physics, 3rd (ed. by J.G.Wilson 1956) 27.
Greisen, K. 1960, Ann. Rev. Nucl. Sci., 10, 63.
Greisen, K. 1966, Phys. Rev. Lett., 16, 748.
Hara, T., et al. 1977a, Proc. 16th ICRC (Kyoto), 8, 135.
Hara, T., et al. 1977b, Proc. 16th ICRC (Kyoto), 11, 166.
Hara, T., et al. 1981, Proc. 18th ICRC (Bangalore), 11, 281.
Hasegawa, H., et al. 1962, Phys. Rev. Lett., 8, 284.
Hatano, Y., et al. 1979, Proc. 16th ICRC (Kyoto), 11, 161.
Hayakawa, S. 1979, COSPAR Symposium on Gamma-Rays (Bangalore).
Hayashida, N., et al. 1979, Proc. 16th ICRC (Kyoto), 8, 143.
Hayashida, N., and Kifune, T. 1980, Nucl. Instr. Method, 173, 431.
Heiles, C. 1976, Ann. Rev. Astron. Astrophys., 14, 1.
Hess, V.F. 1912, Physik Zeitschr, 13, 1804.
Hillas, A.M. 1984, Ann. Rev. Astron. Astrophys., 22, 425.
Honda, M., et al. 1985, Proc. 19th ICRC (La Jolla), 2, 276.
Inoue, M., and Tabara, H. 1981, Publ. Astron. Soc. Japan, 33, 603
Ishikawa, F., et al. 1981, Proc. 17th ICRC (Paris), 8, 141.
Jogo, N. 1981, Ph D Thesis, University of Tokyo.
Jones, M.D. 1985, Proc. 19th ICRC (La Jolla), 2, 28.
Kamata, K., et al. 1968, Canadian J. Phys., 46, S72.
Kaneko, T., et al. 1985, Proc. 19th ICRC (La Jolla), 2, 238.
Karakula, S., et al. 1974, J. Phys., A7, 437.
Kifune, T., et al. 1986a, Ap. J., 301, 230.
Kifune, T., et al. 1986b, J. Phys. G:Nucl.Phys., 12, 129.
Kifune, T., et al. 1986c, J. Phys. G:Nucl.Phys., 12, 143.
Kodaira, K. 1974, Publ. Astron. Soc. Japan, 26, 255.
Lee, Y.W., et al. 1985, Proc. 19th ICRC (La Jolla), 2, 262.
Linsley, J. 1975, Phys. Rev. Lett., 34, 1530.
Linsley, J., and Watson, A.A. 1977, Proc. 15th ICRC (Plovdiv), 12, 203.
Lloyd-Evans, J. 1982, Ph D Thesis, University of Leeds.
Lloyd-Evans, J., et al.1983, Nature, 305, 783.
Mathewson, D.S., and Ford, V.L. 1970, Mem. R.A.S., 74, 139.
McClintock et al. 1978, Ap. J., 225, 465.
McIvor, I. 1977, Mon. Not. R. astr. Soc., 179, 13.
Morello, C., et al. 1983, Proc. 18th ICRC (Bangalore), 2, 137.
Morrison, P., et al. 1954, Phys. Rev., 94, 440.
Murakami, K., et al. 1985, Proc. 19th ICRC (La Jolla), 2, 250.
Nagano, M., et al. 1984, J. Phys. G:Nucl.Phys., 10, 1295.

Nishijima, K. 1983, Master Thesis, Kobe University (in Japanese).
Nagashima, K. 1971, Rep. of Ionosphere and Space Res. in Japan, 25, 189.
Nagashima, K., and Mori, S. 1976, Proc. Int. Cosmic Ray Symp. (Tokyo), 326.
Owens, A.J., and Jokipii, J.R. 1977, Ap. J., 215, 677.
Ormes, J.F., and Protheroe, R.J. 1983, Ap. J., 272, 756.
Ormes, J.F. 1983, Proc. 18th ICRC (Bangalore), 2, 187.
Peters, B., and Westergaard, N.J. 1977, Astrphys. Space Sci., 48, 21.
Protheroe, R.J., et al. 1984, Ap. J. Lett., 286, L47.
Protheroe, R.J., and Clay, R.W. 1985, Nature, 315, 205.
Sakakibara. S. 1965, J. Geomagnetism and Geoelectricity, 17, 99.
Sakakibara, S., et al. 1979, Proc. 16th ICRC (Kyoto), 4, 216.
Samorski, M., and Stamm, W. 1983, Ap. J. Lett., 268, L17.
Shimonaga, S. 1980, Proc. CRRL. Nagoya Univ.(in Japanese), 24, 67.
Simard-Normandin, M., and Kronberg, P.P. 1980, Ap. J., 242, 74.
Simpson, J.A. 1983, Ann. Rev. Nucl. Part. Sci., 33, 323.
Smoot et al. 1977, Phys. Rev. Lett., 39, 898.
Sofue, Y., and Fujimoto, M. 1983, Ap. J., 265, 722.
Streitmatter, R.E., et al. 1985, Astron. Astrophys., 143, 249.
Tabara, H. 1986, Private communication.
Takahashi, Y., et al. 1986, preprint.
Vallee, J.P., and Kronberg, P.P. 1973, Nature Phys. Sciences, 246, 49.
Vallee, J.P., and Kronberg, P.P. 1975, Astron.Astrophys. 43, 233.
Verschuur, G.L. 1979, Fundamentals of Cosmic Physics, 5, 113.
Wdowczyk, J., and Wolfendale, A.W. 1983, Nature, 305, 609.

List of Tables

for first and second harmonics respectively.

Table 10 : List of values for fixed parameters which are taken in our diffusion model.

Table 11 : List of values for free parameters which are taken in representative five models.

Table 12 : The Galactic latitude distribution for (a) all showers, (b) muon-rich showers and (c) muon-poor showers in case of i) electron trigger and ii) muon trigger respectively. The meanings of each parameters are described in appendix E and see them.

Table 13 : The Galactic longitude distribution for (a) all showers, (b) muon-rich showers and (c) muon-poor showers in case of i) electron trigger and ii) muon trigger respectively. The meanings of each parameters are described in appendix E and see them.

Figure Captions

Fig. 1 : Summary of principal results for cosmic ray anisotropy from harmonic analysis in right ascension. Figures (a) and (b) show the amplitude and the maximum phase of first harmonic respectively, where each amplitude is the projected value on the equatorial plane.

Measurements are indicated by O:Bercivitch and Agrawal (1981); Hl:Davies et al.(1979); Po:Fenton and Fenton (1976); U:Cutler et al.(1981); HK:Lee et al.(1985); N: Sakakibara et al.(1979); B:Alexeenko and Navarra (1985); PM:Gombosi et al.(1975); PR:Morello et al.(1983); □ : Delvaille et al.(1959, 1962); ● :Daudin et al.(1956); △ : Murakami et al.(1985); ▽ :Gerhardy and Clay (1983); ○ : Kaneko et al. (1985); ■ :Lloyd-Evans (1982), Eames et al. (1985); ▲ :Efimov et al. (1983).

Fig. 2 : Summary of principal results for cosmic ray anisotropy from harmonic analysis in right ascension. Figures (a) and (b) show the amplitude and the maximum phase of second harmonic respectively, where each amplitude is the projected value on the equatorial plane. The meanings of marks are the same in Fig.2.

Fig. 3 : The model for the local magnetic field which is quoted from Verschuur (1979). The sections are taken along the lines shown in the ellipse, which indicates the cross-section through the spiral arm.

Fig. 4 : Expected amplitude of anisotropy from various models as a function of primary energy. Signatures indicate as follows: CGs, CGg and CGe:C-G effect relative to the local stars, local gas and universal back ground radiation respectively; LB3 and LB7:Leaky box model with δ = 0.3, 0.7 respectively (Blandford and Ostriker 1980), where traversed column density is $\lambda \sim R^{-\delta}$; Cl:anisotropy of iron by closed galaxy model (Peters and Westergaard 1977); S:Cosmic ray density gradient (Sakakibara 1965); B and G: Diffusion model in the arm (Bell et al. 1974) and in the Galaxy (Giler 1983) respectively; DH:dynamical halo model by Owens and jokipii (1977); MI:McIvor (1977).

Fig. 5 : Expected direction of anisotropy on the celestial coordinate. Signatures indicate as follows: CGs, CGg and CGe:C-G effect relative to the local stars, local gas and universal back ground radiation respectively; SI:Spiral

in; SO:Spiral out; GC:Galactic center; AGC:Anti-Galactic center; GNP:Galactic north pole; GSP:Galactic South pole.

Fig. 6 : Anisotropy due to the cosmic ray density gradient. The circles are projections of helices to the cross section perpendicular to the magnetic field. Their boldness indicates the number of particles, and straight arrows indicate the flux in the different directions.

Fig. 7 : The arrangement of detectors in Akeno EAS array. Scintillation counters are designated by closed circles (1 m^2 area) and open circles (2 m^2 area), and muon stations (E_μ > 1 GeV) are by square.

Fig. 8 : Structure of Muon-stations at Akeno Observatory.

Fig. 9 : Block diagram of trigger circuit being set at the each M-station.

Fig.10 : Block diagram of data taking system at the Center.

Fig.11 : Integral distribution of (a) N_μ and (b) N_e in case of rate trigger.

Fig.12 : Frequency versus area of each counter unit, where the distance between the center of neighboring unit is constant of 1 m.

Fig.13 : Non-uniformity of observation time for sidereal time in the case of rate trigger.

Fig.14 : Atmospheric temperature in 1984 at Akeno as the function of the phase of (a) sidereal time, (b) solar time and (c) seasonal.

Fig.15 : Barometric pressure in 1984 at Akeno as the function of the phase of (a) sidereal time, (b) solar time and (c) seasonal.

Fig.16 : Harmonic diagram of temperature variation for (a) sidereal time, (b) solar time and (c) seasonal in 1984 at Akeno. The diagram of left handed is for first harmonic and right handed for second one.

Fig.17 : Harmonic diagram of pressure variation for (a) sidereal time, (b) solar time and (c) seasonal in 1984 at Akeno. The diagram of left handed is for first harmonic and right handed for second one.

Fig.18 : Harmonic diagram of temperature in solar time for each month of 1984 at Akeno, where diagram (a) is for first harmonic and (b) for second one.

Fig.19 : Harmonic diagram of barometric pressure in solar time for each month of 1984 at Akeno, where diagram (a) is for first harmonic and (b) for second one.

Fig.20 : Energy dependence of (a) temperature coefficient and (b) pressure coefficient. Signature are as follows: ○ :for common electron trigger; ● :for common muon trigger; ▲ :for rate trigger.

Fig.21 : Phase distribution of counting rate for sidereal time in case of rate trigger, where phase 0° correspond to 0 hr.

Fig.22 : The results of harmonic analysis in the median energy of 6×10^{14} eV (rate trigger) for (a) sidereal time, (b) solar time and (c) anti-sidereal time, where correction of temperature and pressure effect have not been carried out.

Fig.23 : Monthly rotation of solar (a) diurnal and (b) semi-diurnal vectors in case of rate trigger. For easy to see, diurnal vectors are presented being separated each half year.

Fig.24 : Comparison of sidereal time vectors between before (dotted circles) and after (bold circles) the correction of temperature and pressure effect for (a) first harmonic and (b) second harmonic in case of rate trigger with anti-sidereal vector after the correction (thin circles).

Fig.25 : Celestial distribution of arrival direction as the deviation of events number from the expected one in each cell for all showers in case of (a) electron trigger and (b) muon trigger respectively. Meanings of each mark are as follows; ■ : $+2\sigma \leqq$; ▩ : $+1\sigma \sim +2\sigma$; ▨ : $0\sigma \sim +1\sigma$; ▧ : $-1\sigma \sim 0\sigma$; ⊡ : $-2\sigma \sim -1\sigma$; □ : $\leqq -2\sigma$. Added line indicates the equator of Galactic coordinate.

Fig.26 : Celestial distribution of arrival direction as the deviation of events number from the expected one in each cell for muon-rich showers in case of (a) electron trigger and (b) muon trigger respectively. Meanings of each mark are the same as in Fig.25.

Fig.27 : Celestial distribution of arrival direction as the deviation of events number from the expected one in each cell for muon-poor showers in case of electron trigger. Meanings of each mark are the same as in Fig.25.

Fig.28 : The results of harmonic analysis in sidereal time for all showers in the energy above 10^{15} eV. (a) is that for first harmonic and (b) for second one, where amplitude is presented in upper figures and their phase are in lower ones. Open circles are designated by electron trigger and closed circles are by muon trigger. Error bars are only

statistical error of one standard deviation. They have already been corrected temperature and pressure effect.

Fig.29 : The results of harmonic analysis in sidereal time for muon-rich showers. Signature and other comments are the same as in Fig.28.

Fig.30 : The results of harmonic analysis in sidereal time for muon-poor showers. Signature and other comments are the same as in Fig.28.

Fig.31 : Harmonic diagram in sidereal time for each year (dotted circles) and for their sums (bold circles) with that of anti-sidereal time (thin circles). Harmonics, energy range, muon contents and trigger are as follows: (a):first harmonic, 1×10^{15} - 3.2×10^{16} eV and all showers by electron trigger; (b):first harmonic, 1×10^{16} - 1×10^{17} eV and all showers by muon trigger; (c):second harmonic, 1×10^{15} - 1×10^{17} eV and muon-poor showers by electron trigger.

Fig.32 : Maximum phase of first harmonic as a function of the fraction of selected events in the energy range of (a)(1 - 3.2)$\times 10^{15}$ eV, (b)(3.2 - 10)$\times 10^{15}$ eV and (c)(10 - 32)$\times 10^{15}$ eV, where showers having N_μ / N_e greater than the criterion are analyzed. Closed circles indicate the case of muon trigger and open circles indicate the case of electron trigger.

Fig.33 : The effect of correction of temperature and pressure effect for the same case in Fig 31. dotted circles indicate the results of no correction and solid circles indicate those after correction.

Fig.34 : The ratio of observed event number to expected one is shown as a function of Galactic latitude for all showers in case of (a) electron trigger and (b) muon trigger respectively, where those ratios are integrated over Galactic longitude. Details of data reduction are described in appendix E, and see there.

Fig.35 : The ratio of observed event number to expected one is shown as a function of Galactic latitude for muon-rich showers in case of (a) electron trigger and (b) muon trigger respectively, which are in the same way as in Fig.34.

Fig.36 : The ratio of observed event number to expected one is shown as a function of Galactic latitude for muon-poor showers in case of electron trigger which is in the same way as in Fig.34.

Fig.37 : The ratio of observed event number to expected one is shown as a function of Galactic longitude for all showers in case of (a) electron trigger and (b) muon trigger respectively, where they are integrated over Galactic latitude within $|b| \leqq 30°$. Details of data reduction are described in appendix E, and see there.

Fig.38 : The ratio of observed event number to expected one is shown as a function of Galactic longitude for muon-rich showers in case of (a) electron trigger and (b) muon trigger respectively, which are in the same way as in Fig.37.

Fig.39 : The ratio of observed event number to expected one is shown as a function of Galactic longitude for muon-poor showers in case of electron trigger, which are in the same way as in Fig.37.

Fig.40 : Comparison of our observed results with other observation for first harmonic. Our results are designated by closed triangle (rate trigger), open circles (common electron trigger) and closed circles(common muon trigger), respectively. other measurements are designated by cross (northern hemisphere) and plus (southern hemisphere), respectively. Figure (a) shows the ampilutes and (b) the phases.

Fig.41 : Comparison of our observed results with other observation for second harmonic. Means of marks are the same as in Fig.40.

Fig.42 : Celestial distribution of muon-rich showers by Hasegawa et al.(1962).

Fig.43 : distribution of muon-poor showers for right ascension by Blake et al(1975).

Fig.44 : Comparison of expected amplitude for first harmonic from some models with world wide observed data. This figure is compounded with Figs.4 and 40-(a). Expected amplitude from our models U and A are also represented by two bold solid lines. (upper is from Model A; see Fig.45)

Fig.45 : Expected (a) amplitudes and (b) phases for first harmonic at Akeno from five representative models (each alphabet means the name of each model). Observed results

which are the same as in Fig.28(a) are also shown.

Fig.46 : Energy dependences of diffusion coefficient which are assumed in models U and A (solid lines) are shown with other calculations (dashed lines). Dotted line indicates the corresponding diffusion coefficient when larmor radius of proton is equal to the scattering mean free path.

Fig.47 : Density gradients of cosmic rays near solar system which are derived from models U and A by comparison of the calculated results with the observed one. The subscript means the component of the gradient.

Fig.48 : First harmonic amplitude of muon-rich showers as a function of the fraction of selected events, which is in case of muon trigger.

Fig.49 : First harmonic amplitude of muon-poor showers as a function of the fraction of selected events, which is in case of electron trigger.

Fig.50 : Equatorial coordinate systems. The signatures are as follows: N:Equatorial north pole; JO:direction of incident particle; OR:reference axis of anisotropy; α and θ :right ascension and co-declination.

Fig.51 : The gradient of flux versus Galactic latitude as a function of energy with their sum indicated by 'total' for (a) all showers, (b) muon-rich showers and (c) muon-poor showers, where open circles indicate the case of electron trigger and closed circles the case of muon.

Fig.52 : The model of the Galaxy simplified for calculation. b and h are the height of Galactic disk and halo respectively, and R is the radius of the Galaxy. The axis of Galactic rotation is taken as z axis and considered on the cylindrical coordinate.

Fig.53 : Source distributions as a function of Galactocentric distance. Solid line: A exp(-0.23r); chain line: SNR distribution (Kodaira 1974); broken line: Fθ (5 - r); dotted line: uniform distribution.

Table 1. Expected anisotropy from Compton-Getting effect

references	velocity	direction of anisotropy				amplitude
		Galactic longitude	Galactic latitude	R.A.	declination	
	v(km s^{-1})	l(deg)	b(deg)	α(deg)	δ(deg)	r(%)
local stars*1	19.7	57	+22	271	+30	0.033
local gas*2	22	4	+16	252	-15	0.037
the Galaxy*1	250	90	0	318	+48	0.418
black body*3	390	248	+56	165	+6	0.650

*1 Allen(1973)
*2 McClintock et al.(1978)
*3 Smoot et al.(1977)

Table 2. Temperature and pressure coefficients

trigger	E_0 (eV)	temperature α(% deg^{-1})	pressure β(% deg^{-1})
RM	6×10^{14}	-0.230 ± 0.013	-0.426 ± 0.021
CE	1.4×10^{15}	-0.908 ± 0.041	-1.229 ± 0.075
	4.4×10^{15}	-0.473 ± 0.044	-1.321 ± 0.074
	1.4×10^{16}	-0.341 ± 0.041	-1.099 ± 0.071
	4.3×10^{16}	0.055 ± 0.066	-1.032 ± 0.117
	1.4×10^{17}	-0.293 ± 0.173	-1.584 ± 0.299
	4.3×10^{17}	-0.078 ± 0.375	-4.428 ± 0.717
CM	1.4×10^{15}	-1.191 ± 0.128	-0.627 ± 0.228
	4.4×10^{15}	-0.790 ± 0.055	-0.728 ± 0.094
	1.4×10^{16}	-0.223 ± 0.059	-0.582 ± 0.099
	4.3×10^{16}	-0.099 ± 0.076	-0.571 ± 0.130
	1.4×10^{17}	-0.519 ± 0.151	-0.039 ± 0.262
	4.3×10^{17}	-0.443 ± 0.357	-2.670 ± 0.662
single muon		-0.012 ± 0.000	-0.042 ± 0.001

Table 3. The results of harmonic analysis in the energy of 6×10^{14} eV

time variation	first harmonic amplitude r_1(%)	first harmonic phase ϕ_1(deg)	k_1	second harmonic amplitude r_2(%)	second harmonic phase ϕ_2(deg)	k_2
sidereal	0.20 ±0.09	340 ± 25	2.58	0.32 ±0.09	92 ± 8	6.62
solar	0.04 ±0.09	257 ±117	0.12	0.20 ±0.09	68 ±12	2.65
anti-sidereal	0.12 ±0.09	91 ± 40	1.02	0.11 ±0.09	175 ±22	0.88

Table 4a . Celestial distribution of all events by electron trigger

R.A.	declination δ (deg)									
α(deg)	-10	0	10	20	30	40	50	60	70	80	sum
0- 10	156	647	1437	2169	2315	1860	1073	426	60		10152
10- 20	154	643	1495	2134	2231	1823	1062	435	72		10057
20- 30	164	622	1471	2188	2281	1790	1064	401	80		10069
30- 40	151	632	1462	2112	2219	1860	1081	409	73		10009
40- 50	176	698	1394	2147	2193	1867	1043	407	89		10026
50- 60	145	593	1451	2158	2203	1973	1027	382	83		10022
60- 70	168	665	1515	2126	2260	1797	1053	412	58		10068
70- 80	147	639	1445	2108	2297	1846	1137	402	82		10110
80- 90	162	638	1423	2187	2280	1836	1078	424	78		10111
90-100	172	636	1415	2101	2299	1877	1060	427	66		10060
100-110	175	628	1516	2174	2167	1908	1115	423	82		10193
110-120	168	640	1434	2105	2341	1898	1063	366	81		10104
120-130	162	642	1533	2214	2310	1853	1078	418	97		10314
130-140	181	611	1463	2215	2377	1958	1060	398	72		10347
140-150	160	605	1512	2050	2233	1842	1073	424	71		9978
150-160	151	598	1445	2178	2266	1844	1105	417	73		10092
160-170	159	646	1524	2184	2194	1884	1050	383	69		10104
170-180	166	635	1376	2231	2247	1839	1081	418	76		10079
180-190	135	610	1499	2121	2200	1837	1102	411	83		10005
190-200	151	661	1463	2186	2258	1816	1025	403	56		10027
200-210	179	597	1436	2150	2221	1753	1051	407	69		9875
210-220	158	630	1563	2092	2220	1892	1071	395	82		10114
220-230	150	641	1451	2201	2199	1791	1123	417	76		10055
230-240	169	604	1492	2131	2184	1824	1059	384	69		9923
240-250	159	622	1455	2239	2207	1804	1054	398	64		10016
250-260	164	652	1468	2201	2298	1869	1061	369	71		10160
260-270	136	607	1450	2092	2379	1813	1081	417	65		10045
270-280	145	675	1525	2203	2362	1810	1069	415	84		10295
280-290	174	591	1500	2115	2252	1890	1062	432	82		10109
290-300	150	642	1450	2144	2329	1897	1016	419	57		10114
300-310	167	643	1564	2175	2203	1861	1084	425	77		10207
310-320	144	641	1463	2134	2307	1797	1076	429	70		10074
320-330	168	662	1443	2173	2341	1857	1146	440	78		10316
330-340	169	669	1484	2164	2328	1924	1108	421	92		10375
340-350	158	647	1449	2248	2213	1856	1096	367	64		10104
350-360	153	622	1415	2186	2277	1866	1070	397	93		10091
sum	5746	22834	52881	77736	81491	66712	38657	14718	2694		
$\chi^2/35$	0.846	0.946	1.305	0.991	1.543	1.183	0.775	0.888	1.373		

Table 4b . Celestial distribution of all events by muon trigger

R.A.	declination δ (deg)									
α(deg)	-10	0	10	20	30	40	50	60	70	80	sum
0- 10	65	224	355	430	433	356	240	124	33		2267
10- 20	73	211	348	438	417	358	231	119	38		2241
20- 30	87	214	333	430	399	347	224	110	34		2192
30- 40	85	218	282	430	420	349	241	133	37		2204
40- 50	77	235	330	427	383	363	224	109	50		2206
50- 60	68	208	329	414	414	368	263	116	34		2217
60- 70	79	228	376	428	439	363	246	111	28		2308
70- 80	69	219	352	405	392	353	253	132	33		2214
80- 90	89	217	323	417	403	368	222	134	40		2220
90-100	72	211	323	373	405	353	286	122	30		2177
100-110	91	207	332	389	384	377	217	119	35		2159
110-120	69	234	389	397	429	322	238	122	34		2242
120-130	85	208	350	423	403	363	235	150	46		2267
130-140	82	215	323	456	421	369	215	119	37		2247
140-150	89	202	346	396	439	363	233	116	31		2219
150-160	83	203	358	382	406	364	261	117	32		2212
160-170	87	212	359	370	426	351	252	97	32		2190
170-180	83	213	313	450	419	333	273	99	30		2218
180-190	77	200	288	387	383	340	272	113	44		2110
190-200	86	220	346	378	427	337	224	120	26		2172
200-210	102	185	329	421	433	372	254	124	28		2253
210-220	69	203	363	415	437	366	238	124	35		2259
220-230	84	195	341	393	422	399	248	119	36		2241
230-240	90	178	374	384	340	334	230	133	29		2098
240-250	78	190	327	414	402	333	250	115	24		2143
250-260	80	214	344	385	421	380	207	104	30		2176
260-270	81	226	321	406	451	380	269	143	35		2316
270-280	52	231	353	391	443	334	280	109	40		2240
280-290	90	198	337	396	431	397	218	111	36		2226
290-300	82	221	337	413	371	328	227	140	21		2146
300-310	84	224	335	408	416	371	249	126	38		2257
310-320	79	204	314	398	405	327	255	104	27		2122
320-330	87	215	407	416	446	359	227	113	38		2313
330-340	82	247	318	417	431	419	240	102	42		2303
340-350	78	216	340	404	391	360	212	102	38		2149
350-360	69	203	358	427	440	369	246	103	34		2255
sum	2883	7649	12253	14708	14922	12925	8700	4254	1235		
$\chi^2/35$	1.085	0.954	1.806	1.084	1.361	1.262	1.631	1.347	1.059		

Table 5a . Celestial distribution of muon-rich events by electron trigger

R.A.	declination δ (deg)									
α(deg)	-10	0	10	20	30	40	50	60	70	80	sum
0- 10	85	188	203	190	170	194	154	128	35		1352
10- 20	69	181	203	199	178	206	145	130	39		1355
20- 30	77	172	209	209	205	171	158	113	46		1368
30- 40	71	173	190	221	175	179	181	115	39		1351
40- 50	86	184	196	212	177	184	151	107	46		1352
50- 60	73	136	191	204	190	192	164	111	36		1302
60- 70	86	183	221	211	202	146	153	118	25		1354
70- 80	59	172	208	186	196	201	179	113	33		1351
80- 90	84	149	219	189	169	183	148	112	47		1302
90-100	72	154	205	186	231	187	166	131	39		1376
100-110	87	170	211	188	178	200	176	120	48		1382
110-120	72	161	207	214	207	241	170	115	37		1428
120-130	78	170	228	220	165	201	190	120	49		1425
130-140	77	151	194	200	191	203	162	113	38		1337
140-150	76	136	176	190	183	184	127	121	42		1241
150-160	64	157	217	192	186	179	181	117	33		1336
160-170	70	176	213	211	189	161	172	104	33		1335
170-180	82	162	191	231	207	176	189	124	39		1409
180-190	70	153	232	201	173	193	189	135	46		1394
190-200	80	175	227	212	196	183	157	111	27		1374
200-210	88	169	208	197	183	165	154	105	38		1313
210-220	77	163	232	195	170	182	169	120	45		1360
220-230	67	185	214	216	180	184	186	113	35		1385
230-240	78	170	222	220	195	176	183	116	34		1399
240-250	74	172	185	219	173	214	160	102	31		1339
250-260	79	188	228	199	182	169	179	109	35		1373
260-270	56	159	206	191	225	192	144	124	36		1337
270-280	64	181	236	185	206	170	168	115	48		1376
280-290	80	152	204	194	192	193	180	146	40		1388
290-300	70	194	177	180	175	184	155	109	28		1278
300-310	75	173	212	185	185	211	188	122	44		1401
310-320	58	184	201	175	198	181	175	125	37		1344
320-330	76	176	229	199	171	195	162	125	44		1381
330-340	75	190	210	214	206	194	164	115	50		1427
340-350	67	175	186	208	170	196	171	105	30		1313
350-360	73	162	210	196	181	204	169	110	57		1369
sum	2675	6093	7501	7239	6760	6774	6019	4219	1409		
$\chi^2/35$	0.883	1.235	1.174	0.914	1.347	1.551	1.335	0.751	1.335		

Table 5b . Celestial distribution of muon-rich events by muon trigger

R.A.	declination δ (deg)									
α (deg)	-10	0	10	20	30	40	50	60	70	80	sum
0- 10	46	122	124	83	98	86	82	80	27		755
10- 20	44	108	122	111	85	103	84	72	32		768
20- 30	69	118	113	112	93	103	73	64	27		784
30- 40	55	107	94	106	89	93	101	67	30		751
40- 50	53	118	113	104	95	94	90	55	40		768
50- 60	48	99	107	94	102	106	86	72	28		746
60- 70	71	125	135	108	107	93	99	73	21		841
70- 80	58	115	113	80	86	95	89	74	20		735
80- 90	63	95	123	102	82	95	77	80	34		756
90-100	49	101	112	84	90	90	115	74	27		743
100-110	66	109	111	75	87	108	76	64	33		737
110-120	53	126	140	112	100	100	89	81	28		837
120-130	57	101	116	105	85	108	92	90	40		798
130-140	57	118	107	109	96	91	85	66	27		763
140-150	70	101	98	111	87	99	78	59	26		733
150-160	67	93	122	95	92	97	86	71	24		753
160-170	61	116	118	92	88	99	95	52	25		750
170-180	66	109	108	110	101	80	104	48	22		753
180-190	61	113	117	88	89	84	106	72	40		776
190-200	74	125	130	84	97	98	82	70	22		788
200-210	74	109	113	103	102	102	93	76	26		803
210-220	58	115	126	94	103	99	75	79	28		785
220-230	67	105	113	103	93	110	84	65	28		772
230-240	78	95	119	99	82	77	96	76	27		755
240-250	57	99	97	107	83	97	102	58	20		728
250-260	55	117	115	90	102	95	72	55	24		735
260-270	56	97	113	99	106	98	88	85	31		776
270-280	36	121	110	96	87	85	115	70	33		760
280-290	68	93	115	93	93	111	93	75	29		780
290-300	59	132	92	101	62	90	75	86	16		718
300-310	57	123	109	83	87	98	106	63	31		762
310-320	58	103	101	93	100	82	105	62	22		735
320-330	63	109	141	101	103	94	90	70	35		810
330-340	62	127	114	106	86	113	71	64	35		783
340-350	60	107	110	91	79	99	91	65	30		739
350-360	47	109	123	93	91	104	88	60	29		750
sum	2143	3980	4135	3518	3308	3476	3233	2493	1017		
$\chi^2/35$	1.413	1.039	1.113	1.032	0.908	0.786	1.531	1.375	1.154		

Table 6 . Celestial distribution of muon-poor events by electron trigger

R.A.	declination δ (deg)									
α (deg)	-10	0	10	20	30	40	50	60	70	80	sum
0- 10	1	18	57	107	104	70	32	6	0		395
10- 20	1	17	72	99	123	71	28	15	0		426
20- 30	3	12	46	99	121	86	45	8	1		421
30- 40	2	9	67	95	117	74	29	6	1		400
40- 50	2	15	58	95	95	80	38	8	2		393
50- 60	1	13	61	88	116	77	23	13	0		392
60- 70	2	15	55	78	97	72	37	5	1		362
70- 80	4	13	36	99	106	69	36	8	0		371
80- 90	2	17	49	90	106	83	31	12	1		391
90-100	0	11	37	91	109	87	33	10	2		380
100-110	1	15	46	85	108	73	32	9	1		370
110-120	4	17	51	92	103	78	47	10	0		402
120-130	2	8	52	106	106	70	36	12	1		393
130-140	4	6	46	96	123	80	31	15	2		403
140-150	2	15	51	101	110	91	21	9	1		401
150-160	2	19	47	106	104	77	32	10	4		401
160-170	2	19	51	94	104	92	49	3	2		416
170-180	3	11	72	95	122	75	38	12	1		429
180-190	4	15	62	90	91	85	32	8	0		387
190-200	3	14	49	91	117	86	36	11	0		407
200-210	5	19	61	106	109	75	40	12	0		427
210-220	3	14	49	81	105	95	27	6	0		380
220-230	2	14	42	109	100	76	31	9	1		384
230-240	2	19	54	87	110	81	37	14	1		405
240-250	3	13	49	99	97	65	31	13	2		372
250-260	1	10	46	85	121	81	42	12	3		401
260-270	3	11	53	85	111	62	25	10	1		361
270-280	4	16	66	104	127	69	38	12	1		437
280-290	2	16	48	86	104	65	37	5	1		364
290-300	3	15	62	89	132	80	33	5	1		420
300-310	4	14	63	99	110	58	35	15	1		399
310-320	1	8	46	108	112	93	43	13	0		424
320-330	2	18	40	103	123	83	40	18	1		428
330-340	4	18	59	107	130	95	44	13	2		472
340-350	4	16	56	121	103	92	38	7	2		439
350-360	1	20	65	93	98	73	35	8	1		396
sum	89	520	1924	3459	3974	2819	1262	362	38		
$\chi^2/35$	0.589	0.856	1.563	0.899	0.955	1.152	1.167	1.193	0.809		

Table 7a. Results of harmonic analysis in sidereal time for all showers in case of electron trigger

E_0(eV)	N	r_1(%)	ϕ_1(deg)	k_1	r_2(%)	ϕ_2(deg)	k_2
1.4×10^{15}	101842	1.24±0.44	283±21	3.92	0.86±0.44	145±15	1.88
4.4×10^{15}	100608	0.52±0.45	307±50	0.67	0.35±0.45	147±36	0.31
1.4×10^{16}	89322	0.68±0.47	306±40	1.04	0.76±0.47	147±18	1.29
4.3×10^{16}	29917	0.80±0.82	238±58	0.48	2.61±0.82	106± 9	5.12
1.4×10^{17}	2902	2.53±2.63	304±59	0.47	4.25±2.63	71±18	1.31
4.3×10^{17}	208	11.42±9.79	169±49	0.68	12.89±9.79	22±22	0.87

Table 7b. Results of harmonic analysis in sidereal time for all showers in case of muon trigger

E_0(eV)	N	r_1(%)	ϕ_1(deg)	k_1	r_2(%)	ϕ_2(deg)	k_2
1.4×10^{15}	5075	2.19±2.00	328±52	0.60	1.46±2.00	89±39	0.27
4.4×10^{15}	27881	1.66±0.85	333±29	1.91	0.34±0.85	99±71	0.08
1.4×10^{16}	23380	2.05±0.93	309±26	2.45	0.83±0.93	137±32	0.40
4.3×10^{16}	14062	2.27±1.19	318±30	1.82	1.67±1.19	89±20	0.99
1.4×10^{17}	3360	1.46±2.45	326±96	0.18	1.23±2.45	78±57	0.13
4.3×10^{17}	393	11.76±7.14	298±35	1.36	6.37±7.14	140±32	0.40

Table 8a. Results of harmonic analysis in sidereal time for muon-rich showers in case of electron trigger

E_0(eV)	N	r_1(%)	ϕ_1(deg)	k_1	r_2(%)	ϕ_2(deg)	k_2
1.4×10^{15}	16860	1.82±1.09	208± 21	1.39	0.45±1.09	116±70	0.08
4.4×10^{15}	10080	1.03±1.41	226± 50	0.27	1.11±1.41	33±36	0.31
1.4×10^{16}	11122	2.16±1.34	303± 40	1.30	0.61±1.34	131±63	0.10
4.3×10^{16}	3250	0.86±2.48	23±166	0.06	3.10±2.48	59±23	0.78
1.4×10^{17}	350	15.67±7.53	261± 28	2.16	13.39±7.53	105±16	1.58
4.3×10^{17}	18	26.22±33.3	114± 73	0.31	28.16±33.3	74±34	0.36

Table 8b. Results of harmonic analysis in sidereal time for muon-rich showers in case of muon trigger

E_0(eV)	N	r_1(%)	ϕ_1(deg)	k_1	r_2(%)	ϕ_2(deg)	k_2
1.4×10^{15}	1350	6.21±3.86	263±36	1.29	3.78±3.86	109±29	0.48
4.4×10^{15}	9314	2.34±1.47	136±36	1.26	1.50±1.47	33±28	0.52
1.4×10^{16}	7622	2.11±1.62	246±44	0.84	1.41±1.62	125±33	0.38
4.3×10^{16}	5478	2.04±1.91	343±54	0.57	3.62±1.91	59±15	1.80
1.4×10^{17}	1614	4.79±3.52	331±42	0.93	2.65±3.52	66±38	0.28
4.3×10^{17}	212	16.13±9.72	251±35	1.38	5.94±9.72	97±47	0.19

Table 9. Results of harmonic analysis in sidereal time for muon-poor showers in case of electron trigger

E_0(eV)	N	r_1(%)	ϕ_1(deg)	k_1	r_2(%)	ϕ_2(deg)	k_2
1.4×10^{15}	3589	1.36±2.36	324±100	0.17	4.90±2.36	173±14	2.14
4.4×10^{15}	5326	5.27±1.94	329± 21	3.68	5.48±1.94	169±10	3.94
1.4×10^{16}	3195	3.02±2.50	273± 47	0.73	4.15±2.50	157±17	1.38
4.3×10^{16}	932	5.73±4.63	133± 46	0.77	3.21±4.63	137±41	0.24
1.4×10^{17}	66	15.53±17.4	6± 64	0.40	9.76±17.4	124±51	0.16
4.3×10^{17}	5	172.6±63.3	192± 21	3.72	109.4±63.3	8±17	1.50

Table 10. Fixed parameters

parameters	symbol	values
radius of the disk	R	15 kpc
distance from the Galactic center to our solar system.	R_s	8.5 kpc
height from the Galactic plane to our solar system	z_s	8 pc
total cross section of inelastic scattering with interstellar gas	σ	100 mb
number density of interstellar gas	n	0.7 cm^{-3}
velocity of cosmic ray	v	3×10^{10} cm s^{-1}
strength of galactic magnetic field	B	3 μG

Table 11. Parameters in each Model

parameters	Model R	Model E	Model C	Model U	Model A
b	0.1	0.1	1	0.1	1
h	1	1	10	1	10
κ	7×10^{28}	6×10^{28}	3×10^{28}	9×10^{28}	8×10^{28}
η	0.6	0.65	0.7	0.5	0.65
K_h/K_d	10	10	10	10	10
IN/OUT	IN	IN	IN	IN	OUT
S(r)	SNR	EXP	HVS	UNI	EXP

meanings of symbols :

b (kpc) : disk height

h (kpc) : halo height

$K_d = \kappa(E(eV)/10^{15})^{\eta}$ (cm^2s^{-1}) : diffusion coefficient in the disk

K_h/K_d : ratio of diffusion coefficients

spiral IN/OUT : direction of Galactic magnetic field

S(r) : source distribution

SNR : distribution of SNR

EXP : A exp(-0.23r)

HVS : $F\theta(500-r)$

UNI : uniform distribution

Table 12a-i. The Galactic latitude distribution for all showers in case of electron trigger

E_0(eV)	χ^2	$-90° \leqq b \leqq 0°$ c_{b0}	$c_{b1}(\times 10^{-4})$	$0° \leqq b \leqq +90°$ c_{b0}	$c_{b1}(\times 10^{-4})$	$-90° \leqq b \leqq +90°$ c_{b0}	$c_{b1}(\times 10^{-4})$
1.4×10^{15}	0.815	1.01 ±0.01	4.81 ±2.20	1.01 ±0.01	-1.46 ±1.19	1.00 ±0.00	0.12 ±0.58
4.4×10^{15}	0.356	1.01 ±0.00	3.36 ±1.02	1.00 ±0.00	-1.15 ±0.58	1.00 ±0.00	-0.88 ±0.30
1.4×10^{16}	0.702	0.99 ±0.00	-6.16 ±1.62	1.01 ±0.01	-2.36 ±1.54	1.00 ±0.00	-1.18 ±0.53
4.3×10^{16}	1.264	0.98 ±0.01	-4.32 ±3.13	1.03 ±0.02	-6.46 ±3.43	1.00 ±0.01	-0.23 ±1.35
1.4×10^{17}	0.235	0.99 ±0.03	-1.10 ±10.1	1.02 ±0.02	-5.34 ±3.45	1.00 ±0.01	0.01 ±1.86
Total	0.491	1.00 ±0.00	-0.36 ±0.42	1.01 ±0.00	-2.03 ±0.50	1.00 ±0.00	-0.58 ±0.22

Table 12a-ii. The Galactic latitude distribution for all showers in case of muon trigger

E_0(eV)	χ^2	$-90° \leqq b \leqq 0°$ c_{b0}	$c_{b1}(\times 10^{-4})$	$0° \leqq b \leqq +90°$ c_{b0}	$c_{b1}(\times 10^{-4})$	$-90° \leqq b \leqq +90°$ c_{b0}	$c_{b1}(\times 10^{-4})$
1.4×10^{15}	0.736	1.01 ±0.02	3.06 ±8.09	1.01 ±0.03	-3.30 ±5.86	1.00 ±0.01	-1.87 ±2.39
4.4×10^{15}	1.215	0.99 ±0.02	-4.91 ±6.89	1.00 ±0.01	-0.97 ±2.23	1.00 ±0.01	-1.53 ±1.29
1.4×10^{16}	1.094	1.04 ±0.01	12.7 ±5.02	0.98 ±0.01	2.08 ±2.52	1.00 ±0.01	-0.96 ±1.39
4.3×10^{16}	1.192	0.95 ±0.02	122.0 ±8.09	1.02 ±0.02	-5.59 ±3.91	1.00 ±0.01	-2.35 ±1.86
1.4×10^{17}	1.073	0.98 ±0.05	-2.69 ±17.1	1.00 ±0.04	-0.31 ±8.20	0.99 ±0.01	1.39 ±3.72
Total	0.736	1.00 ±0.01	-2.95 ±3.55	1.00 ±0.01	-1.04 ±1.51	1.00 ±0.00	-1.62 ±0.72

Table 12b-i. The Galactic latitude distribution for muon-rich showers in case of electron trigger

E_0(eV)	χ^2	$-90° \leqq b \leqq 0°$ c_{b0}	$c_{b1}(\times10^{-4})$	$0° \leqq b \leqq +90°$ c_{b0}	$c_{b1}(\times10^{-4})$	$-90° \leqq b \leqq +90°$ c_{b0}	$c_{b1}(\times10^{-4})$
1.4×10^{15}	1.699	0.96 ±0.01	-9.45 ±3.61	1.02 ±0.02	-1.26 ±5.34	0.99 ±0.01	2.81 ±2.00
4.4×10^{15}	0.873	1.04 ±0.01	17.5 ±3.29	0.98 ±0.02	5.84 ±4.87	1.00 ±0.01	2.41 ±1.90
1.4×10^{16}	0.436	0.98 ±0.01	-10.5 ±3.20	0.98 ±0.01	3.72 ±2.57	1.00 ±0.00	-0.60 ±1.23
4.3×10^{16}	1.271	0.94 ±0.06	-27.1 ±19.9	0.96 ±0.04	-1.08 ±9.05	1.00 ±0.02	-3.06 ±4.57
1.4×10^{17}	0.668	-	-	1.06 ±0.08	-9.98 ±20.5	1.03 ±0.04	-3.95 ±11.7
Total	0.915	0.98 ±0.01	-6.05 ±2.10	1.00 ±0.01	1.11 ±2.37	1.00 ±0.00	0.96 ±0.91

Table 12b-ii. The Galactic latitude distribution for muon-rich showers in case of muon trigger

E_0(eV)	χ^2	$-90° \leqq b \leqq 0°$ c_{b0}	$c_{b1}(\times10^{-4})$	$0° \leqq b \leqq +90°$ c_{b0}	$c_{b1}(\times10^{-4})$	$-90° \leqq b \leqq +90°$ c_{b0}	$c_{b1}(\times10^{-4})$
1.4×10^{15}	0.444	1.03 ±0.05	17.5 ±17.5	0.99 ±0.03	3.46 ±7.94	0.99 ±0.01	3.21 ±3.95
4.4×10^{15}	0.723	1.01 ±0.02	8.46 ±5.79	0.98 ±0.01	7.86 ±3.25	0.99 ±0.01	3.57 ±1.60
1.4×10^{16}	0.881	1.02 ±0.03	11.3 ±8.32	0.98 ±0.02	5.65 ±4.02	0.99 ±0.01	2.90 ±2.12
4.3×10^{16}	0.914	0.93 ±0.03	-23.0 ±9.44	1.03 ±0.02	-9.21 ±5.43	1.00 ±0.01	-3.30 ±2.60
1.4×10^{17}	0.977	0.94 ±0,05	-24.6 ±18.4	0.97 ±0.05	2.47 ±13.3	0.99 ±0.02	-3.74 ±5.63
Total	0.904	0.99 ±0.01	-0.47 ±4.86	0.99 ±0.01	2.88 ±2.39	1.00 ±0.00	1.32 ±1.14

Table 12c. The Galactic latitude distribution for muon-poor showers in case of electron trigger

E_0(eV)	χ^2	$-90° \leqq b \leqq 0°$		$0° \leqq b \leqq +90°$		$-90° \leqq b \leqq +90°$	
		c_{b0}	$c_{b1}(\times 10^{-4})$	c_{b0}	$c_{b1}(\times 10^{-4})$	c_{b0}	$c_{b1}(\times 10^{-4})$
1.4×10^{15}	0.689	0.97 ±0.02	-0.24 ±9.71	0.92 ±0.02	16.6 ±5.37	1.00 ±0.01	0.08 ±2.96
4.4×10^{15}	0.898	0.98 ±0.03	-0.31 ±13.5	0.96 ±0.01	3.01 ±2.16	1.01 ±0.01	-8.16 ±2.26
1.4×10^{16}	0.370	1.01 ±0.03	0.02 ±12.8	0.99 ±0.02	1.92 ±5.29	1.00 ±0.01	0.35 ±2.32
4.3×10^{16}	0.448	1.05 ±0.03	0.21 ±16.6	1.01 ±0.05	-5.09 ±11.8	1.00 ±0.02	-4.30 ±5.23
Total	1.008	0.99 ±0.02	-0.17 ±8.94	0.96 ±0.01	6.81 ±2.89	1.00 ±0.01	-2.88 ±1.76

Table 13a-i. The Galactic longitude distribution for all showers in case of electron trigger

E_0(eV)	$\chi^2/17$	c_{10}	$c_{11}(\times 10^{-4})$	r(%)	l(deg)	k
1.4×10^{15}	0.664	1.009±0.005	-0.82±0.48	0.84±0.60	44±20	0.98
4.4×10^{15}	1.069	1.013±0.006	-1.14±0.62	0.44±0.60	55±39	0.27
1.4×10^{16}	0.664	1.007±0.005	-0.68±0.52	1.14±0.64	69±32	1.59
4.3×10^{16}	1.354	0.990±0.012	1.59±1.22	3.00±1.09	178±10	3.77
1.4×10^{17}	0.435	0.997±0.024	-1.05±2.34	1.28±3.54	176±79	0.07
Total	0.515	1.004±0.002	-0.25±0.18	0.24±0.26	26±30	0.45

Table 13a-ii. The Galactic longitude distribution for all showers in case of muon trigger

E_0(eV)	$\chi^2/17$	c_{10}	$c_{11}(\times 10^{-4})$	r(%)	l(deg)	k
1.4×10^{15}	1.241	1.055±0.030	-5.17±2.90	3.17±2.72	8±25	0.68
4.4×10^{15}	1.085	0.092±0.012	0.07±1.17	0.99±1.17	3±34	0.35
1.4×10^{16}	0.793	1.011±0.011	-0.70±1.12	2.21±1.26	67±16	1.54
4.3×10^{16}	0.737	0.998±0.014	0.19±1.42	1.65±1.64	1±28	0.51
1.4×10^{17}	0.565	0.963±0.024	4.98±2.36	3.16±3.31	142±30	0.46
Total	0.480	1.001±0.004	0.15±0.38	0.43±0.56	82±38	0.29

Table 13b-i. The Galactic longitude distribution
for muon-rich showers in case of electron trigger

E_0(eV)	χ^2/17	c_{10}	$c_{11}(\times 10^{-4})$	r(%)	l(deg)	k
1.4×10^{15}	0.774	0.983±0.013	2.08±1.27	2.24±1.50	174±19	1.11
4.4×10^{15}	0.637	0.998±0.016	-0.02±1.57	1.49±1.97	134±38	0.29
1.4×10^{16}	0.353	1.021±0.012	-1.98±1.19	1.60±1.87	79±33	0.37
4.3×10^{16}	1.701	0.936±0.042	6.23±4.20	1.88±3.41	127±52	0.15
Total	0.499	1.004±0.005	-0.41±0.49	0.44±0.72	88±47	0.18

Table 13b-ii. The Galactic longitude distribution
for muon-rich showers in case of muon trigger

E_0(eV)	χ^2/17	c_{10}	$c_{11}(\times 10^{-4})$	r(%)	l(deg)	k
1.4×10^{15}	0.749	1.111±0.042	-13.08±3.95	7.17±5.42	28± 22	0.88
4.4×10^{15}	0.986	0.939±0.017	5.53±1.72	2.91±2.08	123± 20	0.98
1.4×10^{16}	0.555	0.995±0.018	0.61±1.75	1.45±2.28	95± 45	0.20
4.3×10^{16}	1.052	0.990±0.028	1.32±2.79	0.85±2.67	67±180	0.05
1.4×10^{17}	0.594	0.979±0.038	3.41±3.81	2.96±4.86	44± 47	0.19
Total	0.719	0.985±0.008	1.60±0.80	0.47±0.97	121± 59	0.12

Table 13c. The Galactic longitude distribution
for muon-poor showers in case of electron trigger

E_0(eV)	χ^2/17	c_{10}	$c_{11}(\times 10^{-4})$	r(%)	l(deg)	k
1.4×10^{15}	1.542	0.967±0.036	-0.03±3.55	2.88±3.25	66±32	0.39
4.4×10^{15}	1.313	1.096±0.024	-10.88±2.33	6.79±2.59	62±11	3.45
1.4×10^{16}	1.205	1.076±0.033	-10.41±3.22	7.87±2.27	59± 8	6.02
4.3×10^{16}	1.136	0.920±0.067	5.53±6.68	6.94±6.09	178±25	0.65
Total	1.286	1.015±0.014	-1.98±1.37	3.51±1.30	68±11	3.58

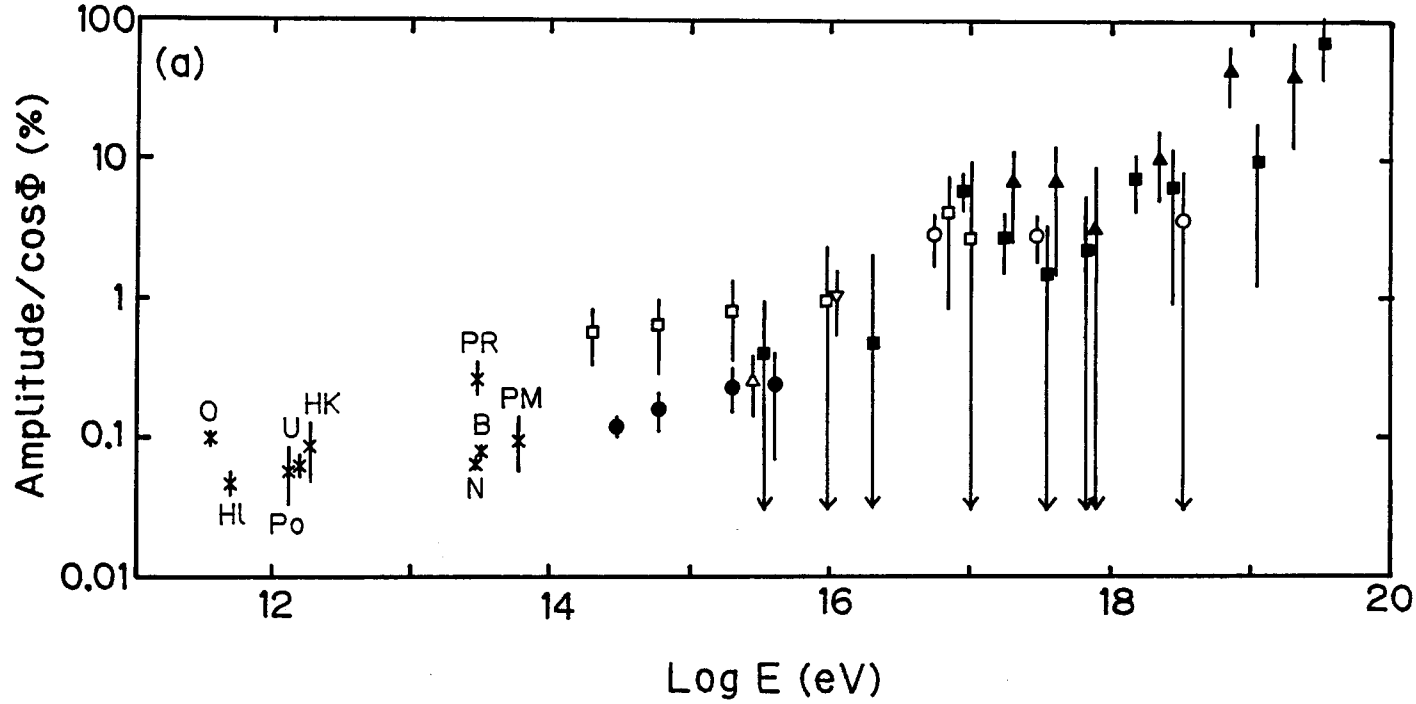
(a)
100
10
1
0.1
0.01
Amplitude/cosΦ (%)
O
Hl
Po
U
HK
PR
B
N
PM
12
14
16
18
20
Log E (eV)

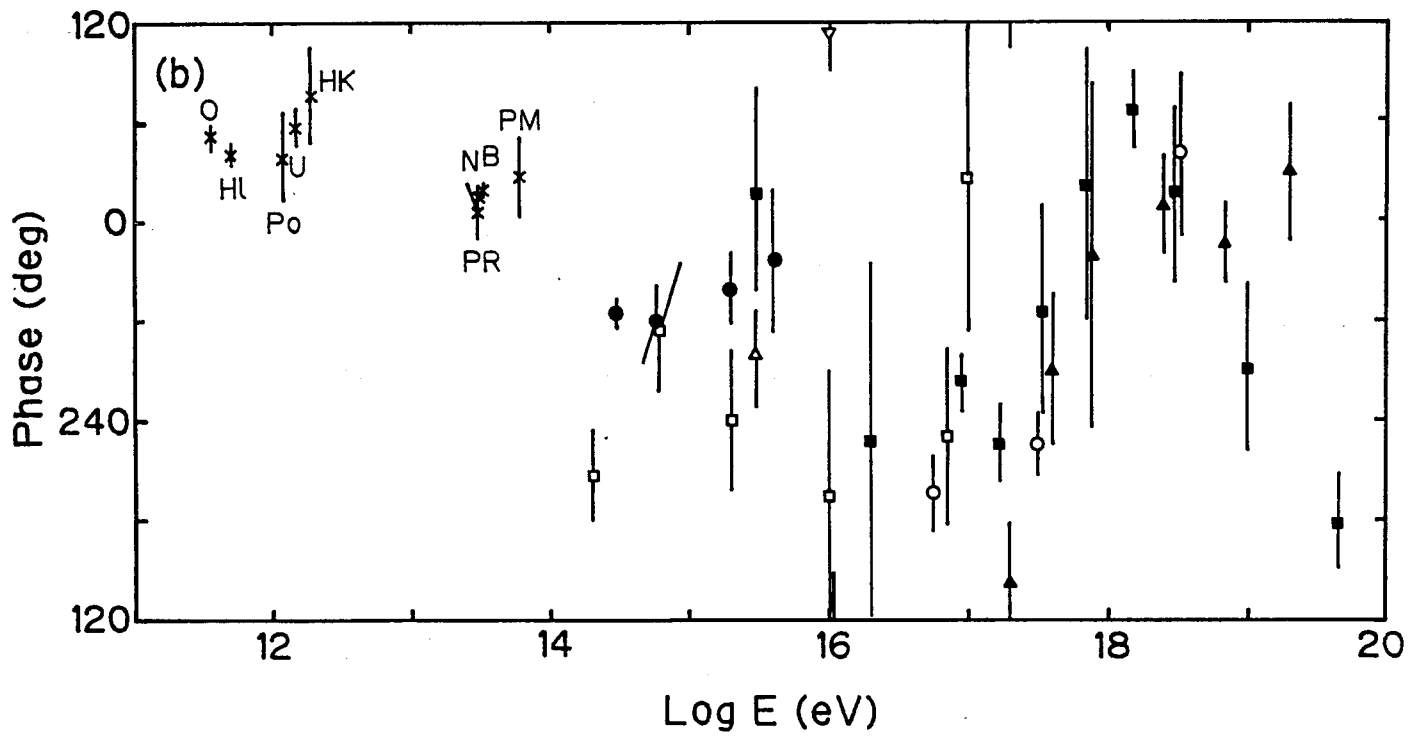
(b)
120
0
240
120
Phase (deg)
O
Hl
Po
U
HK
PR
N
B
PM
12
14
16
18
20
Log E (eV)

Fig. 1

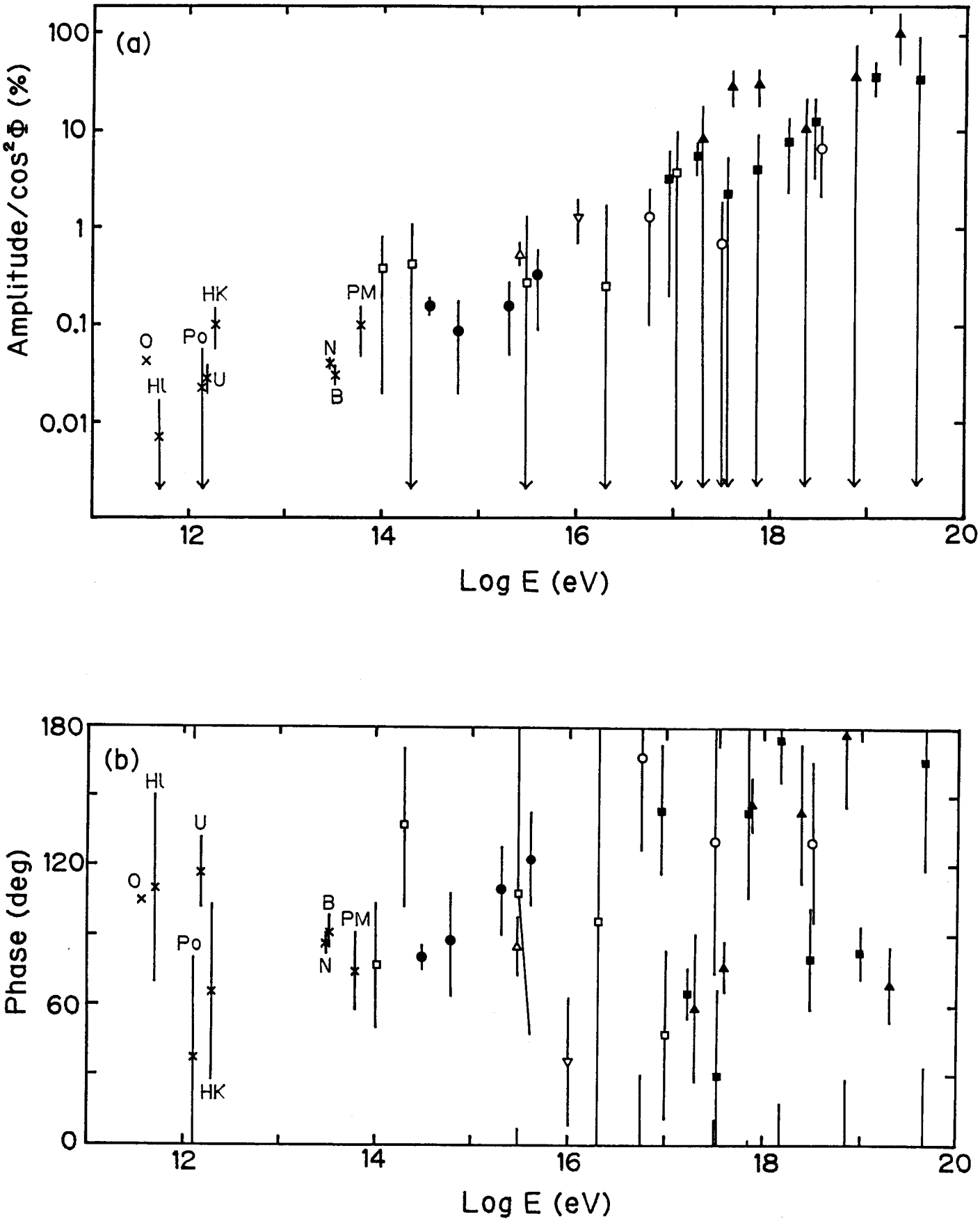
(a)
Amplitude/cos²Φ (%)
100
10
1
0.1
0.01
O
Hl
Po
HK
U
N
B
PM
12
14
16
18
20
Log E (eV)
(b)
Phase (deg)
180
120
60
0
Hl
O
U
Po
HK
B
N
PM
12
14
16
18
20
Log E (eV)

Fig. 2

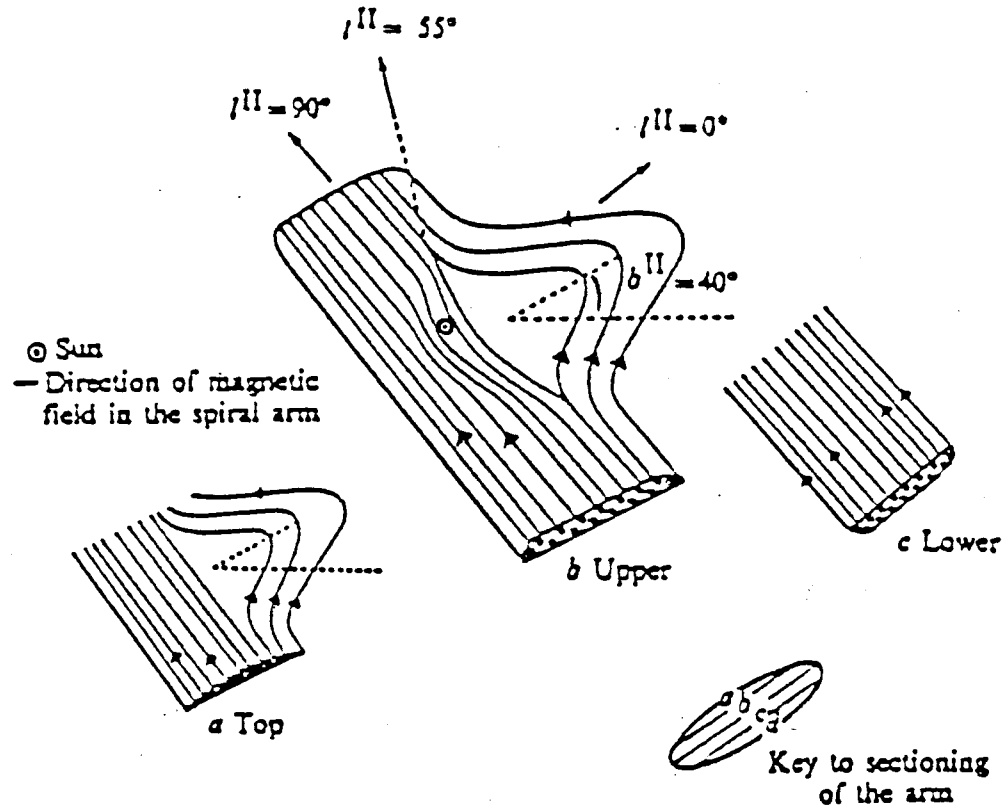
$l^{II} = 55°$
$l^{II} = 90°$
$l^{II} = 0°$
$b^{II} = 40°$
⊙ Sun
— Direction of magnetic field in the spiral arm
a Top
b Upper
c Lower
Key to sectioning of the arm

Fig. 3

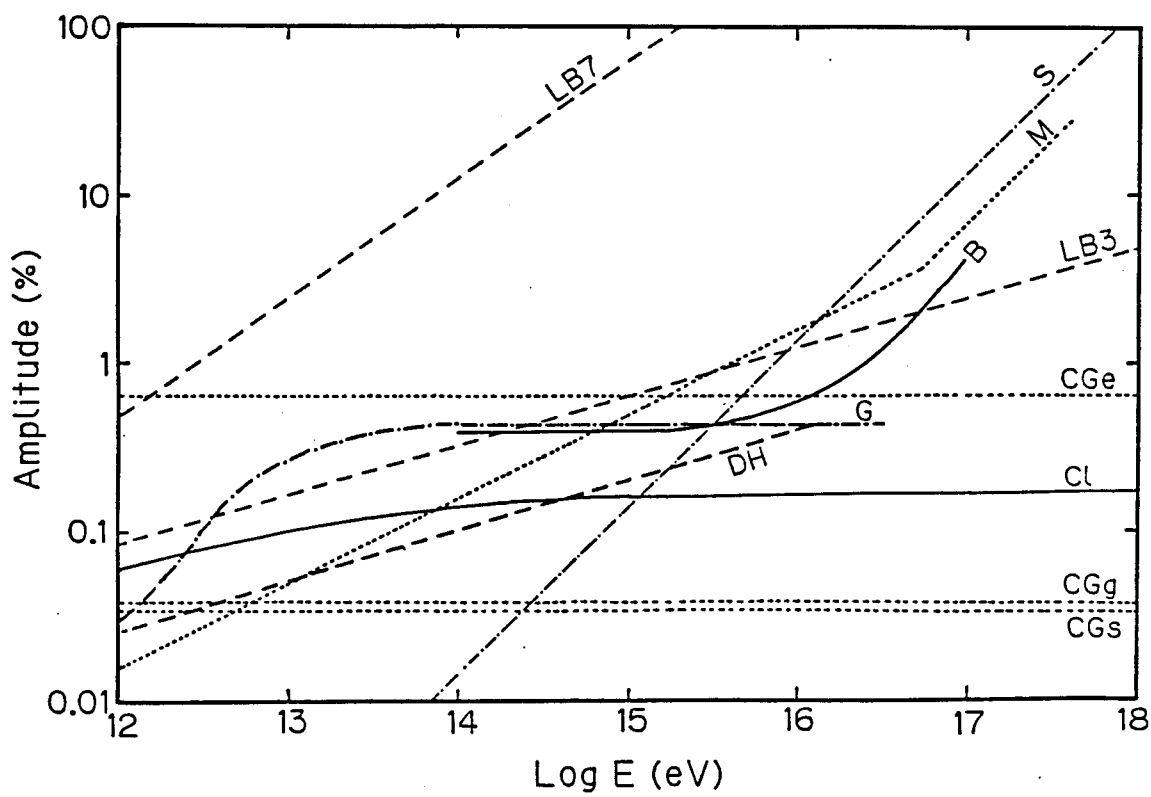
100
10
1
0.1
0.01
Amplitude (%)
12
13
14
15
16
17
18
Log E (eV)
LB7
S
M
B
LB3
CGe
G
DH
Cl
CGg
CGs

Fig. 4

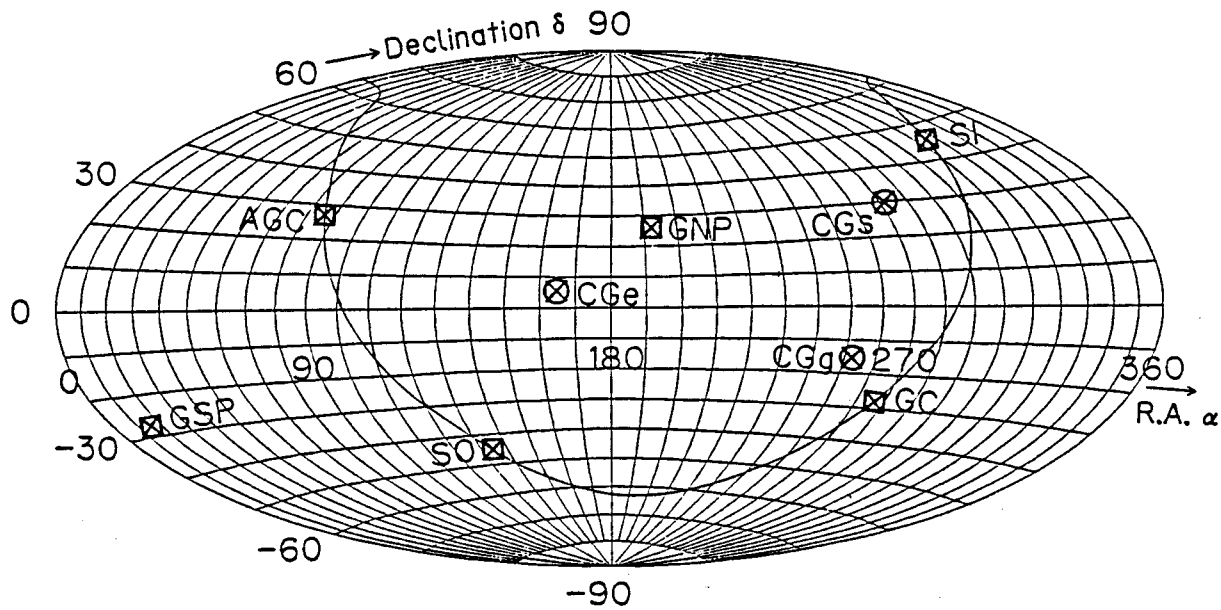
Declination δ 90
60
30
0
-30
-60
-90
0
90
180
270
360
R.A. α
SI
AGC
GNP
CGs
CGe
CGg
GC
GSP
SO

Fig. 5

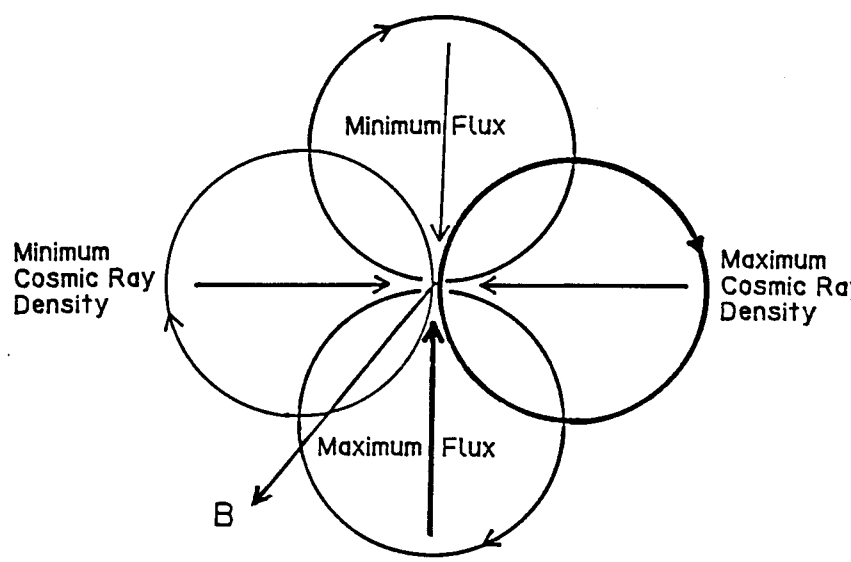
Minimum Flux
Minimum
Cosmic Ray
Density
Maximum
Cosmic Ray
Density
Maximum Flux
B

Fig. 6

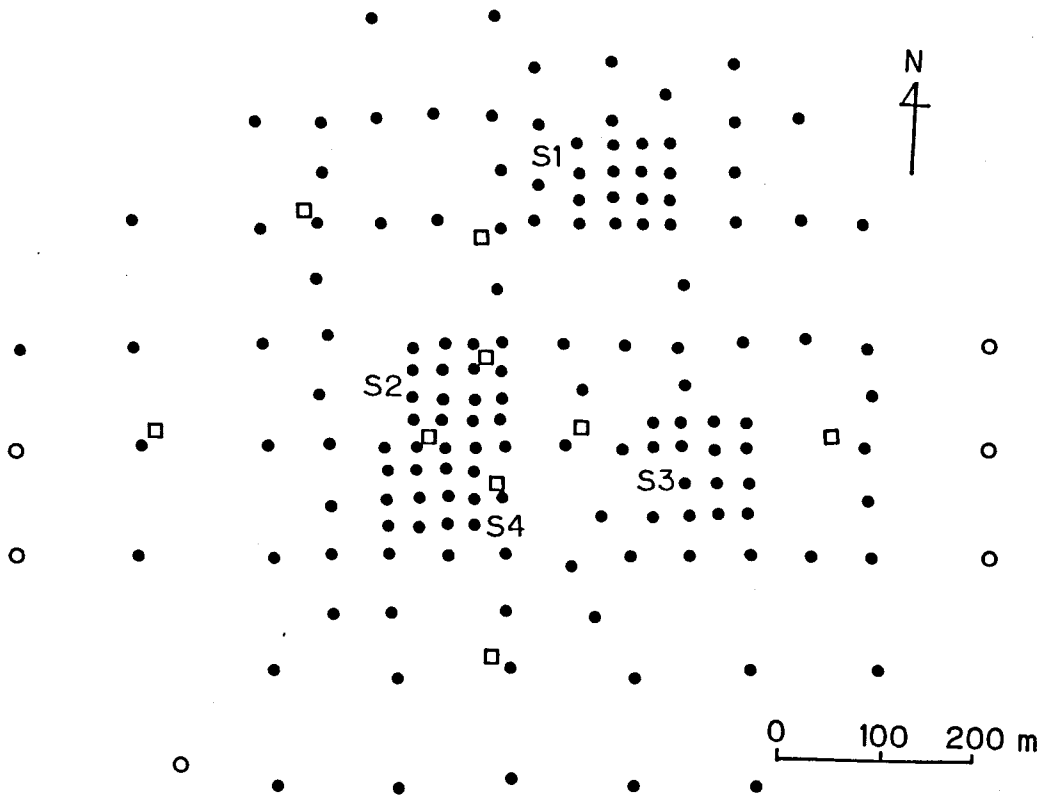
N
S1
S2
S3
S4
0 100 200 m

Fig. 7

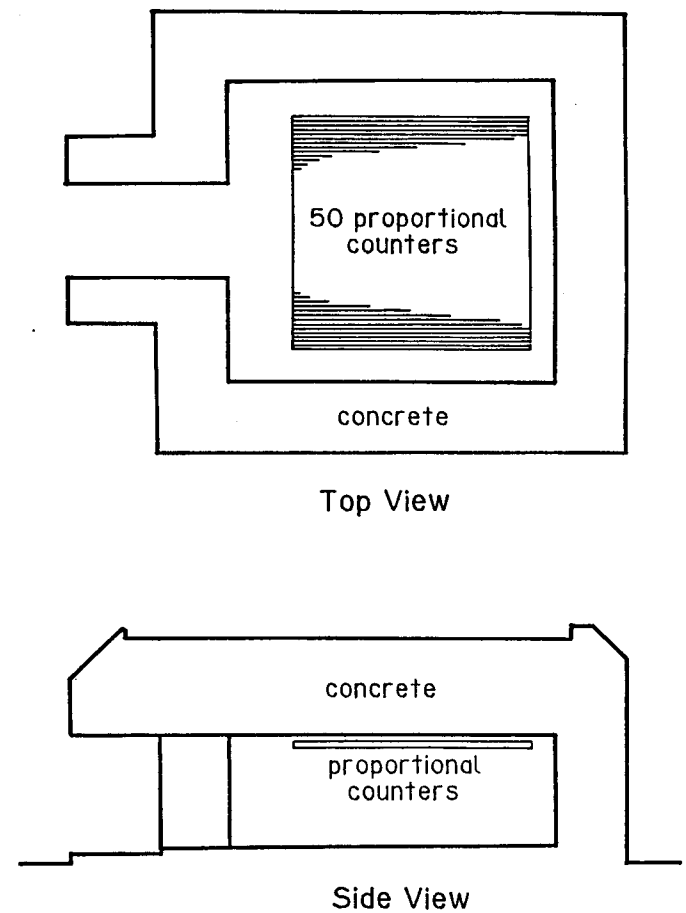
50 proportional counters
concrete
Top View
concrete
proportional counters
Side View

Fig. 8

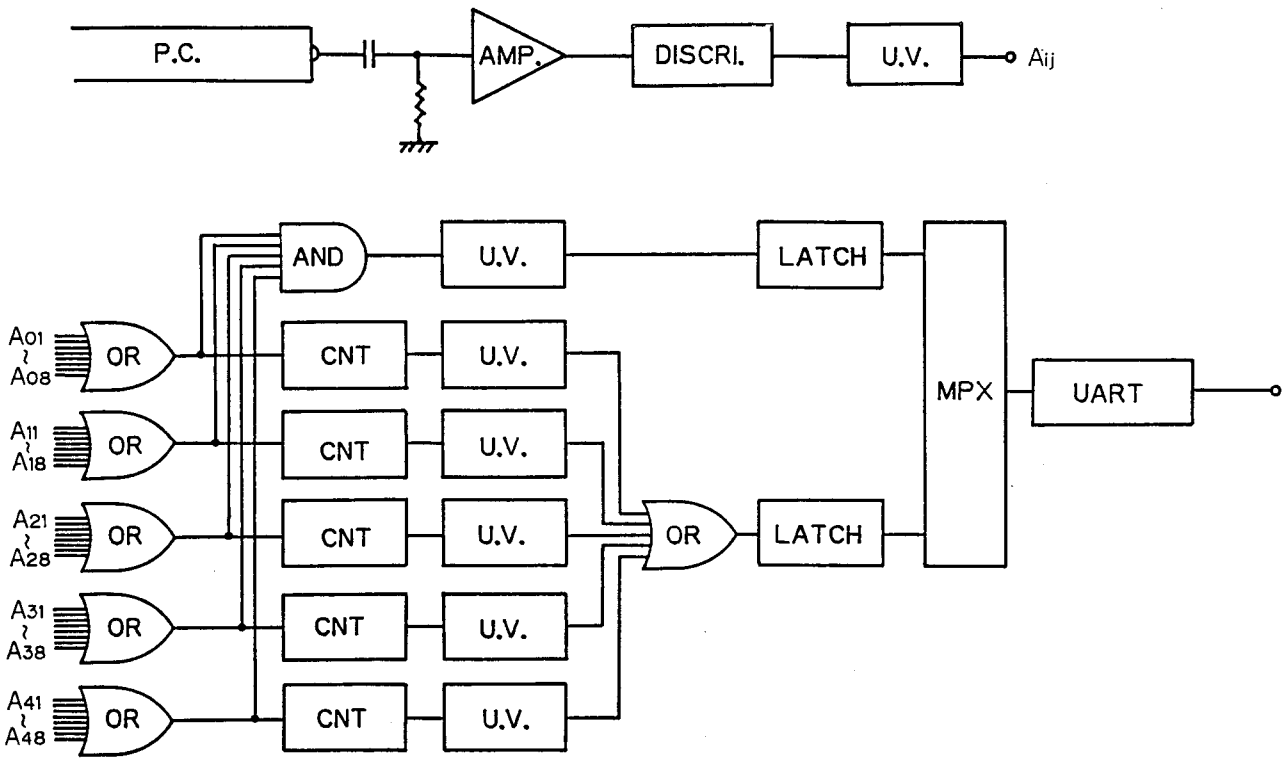
P.C.
AMP.
DISCRI.
U.V.
Aij
AND
U.V.
LATCH
A01 ~ A08
OR
CNT
U.V.
A11 ~ A18
A21 ~ A28
A31 ~ A38
A41 ~ A48
MPX
UART
OR
LATCH

Fig. 9

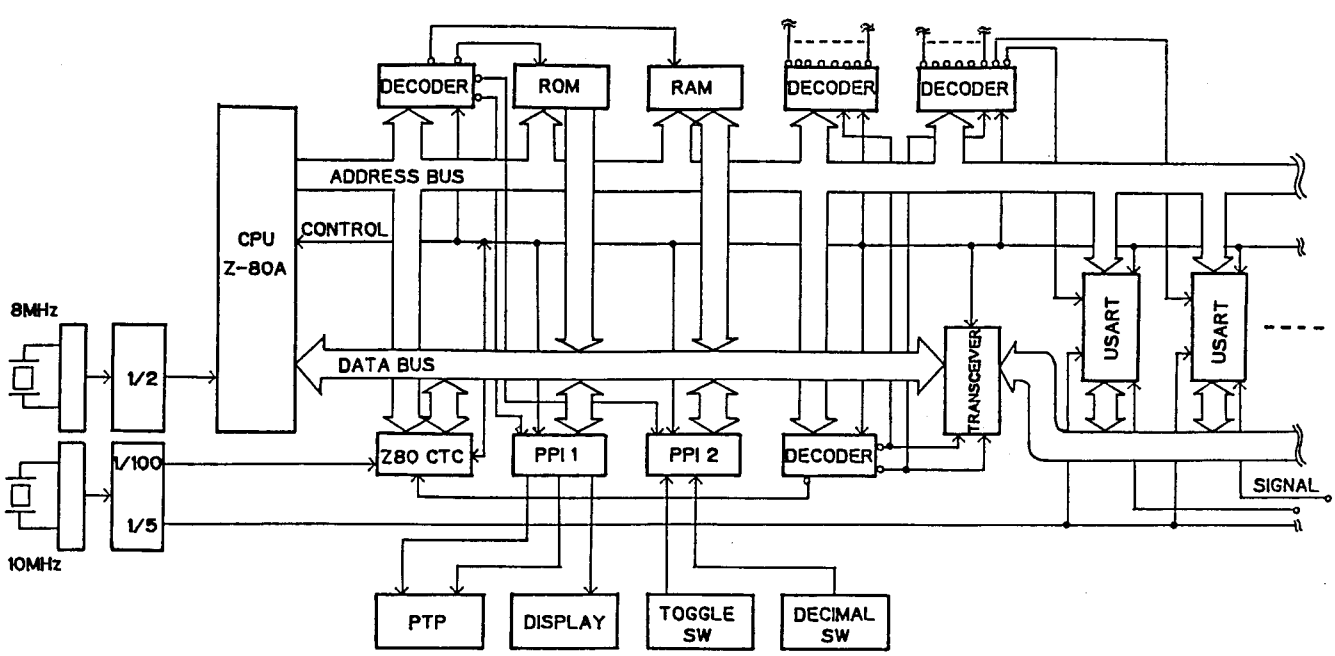
DECODER
ROM
RAM
DECODER
DECODER
ADDRESS BUS
CONTROL
CPU Z-80A
8MHz
1/2
DATA BUS
TRANSCEIVER
USART
USART
1/100
1/5
10MHz
Z80 CTC
PPI 1
PPI 2
DECODER
SIGNAL
PTP
DISPLAY
TOGGLE SW
DECIMAL SW

Fig. 10

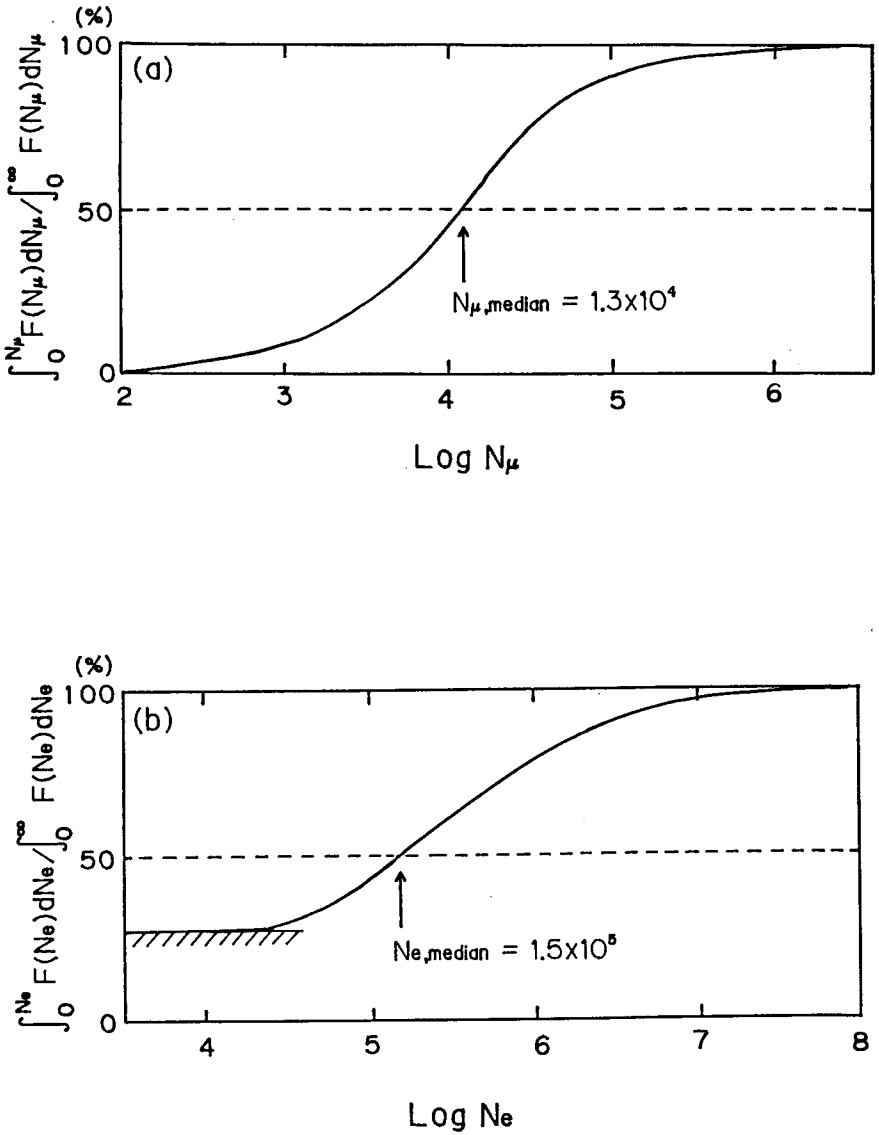
(%)
100
50
0
(a)
$\int_0^{N_\mu} F(N_\mu)dN_\mu / \int_0^{\infty} F(N_\mu)dN_\mu$
$N_{\mu,median} = 1.3\times10^4$
2
3
4
5
6
Log N_μ
(%)
100
50
0
(b)
$\int_0^{Ne} F(Ne)dNe / \int_0^{\infty} F(Ne)dNe$
$Ne_{,median} = 1.5\times10^5$
4
5
6
7
8
Log Ne

Fig. 11

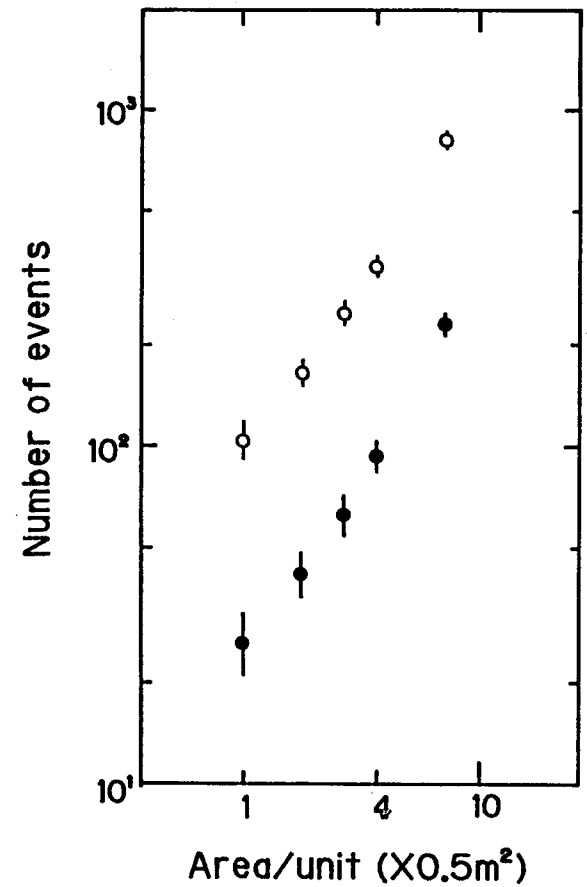
10^3
10^2
10^1
Number of events
1
4
10
Area/unit (X0.5m²)

Fig. 12

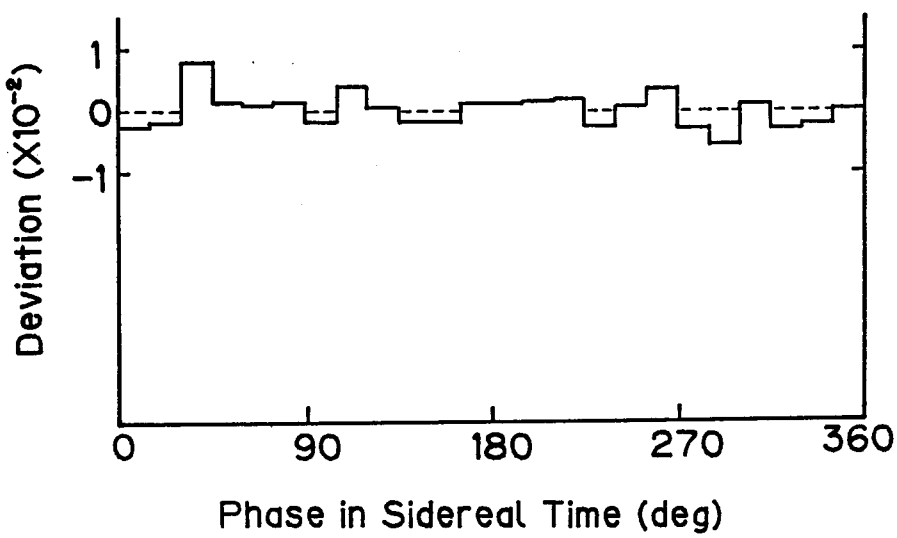
Deviation (X10⁻⁸)
1
0
-1
0
90
180
270
360
Phase in Sidereal Time (deg)

Fig. 13

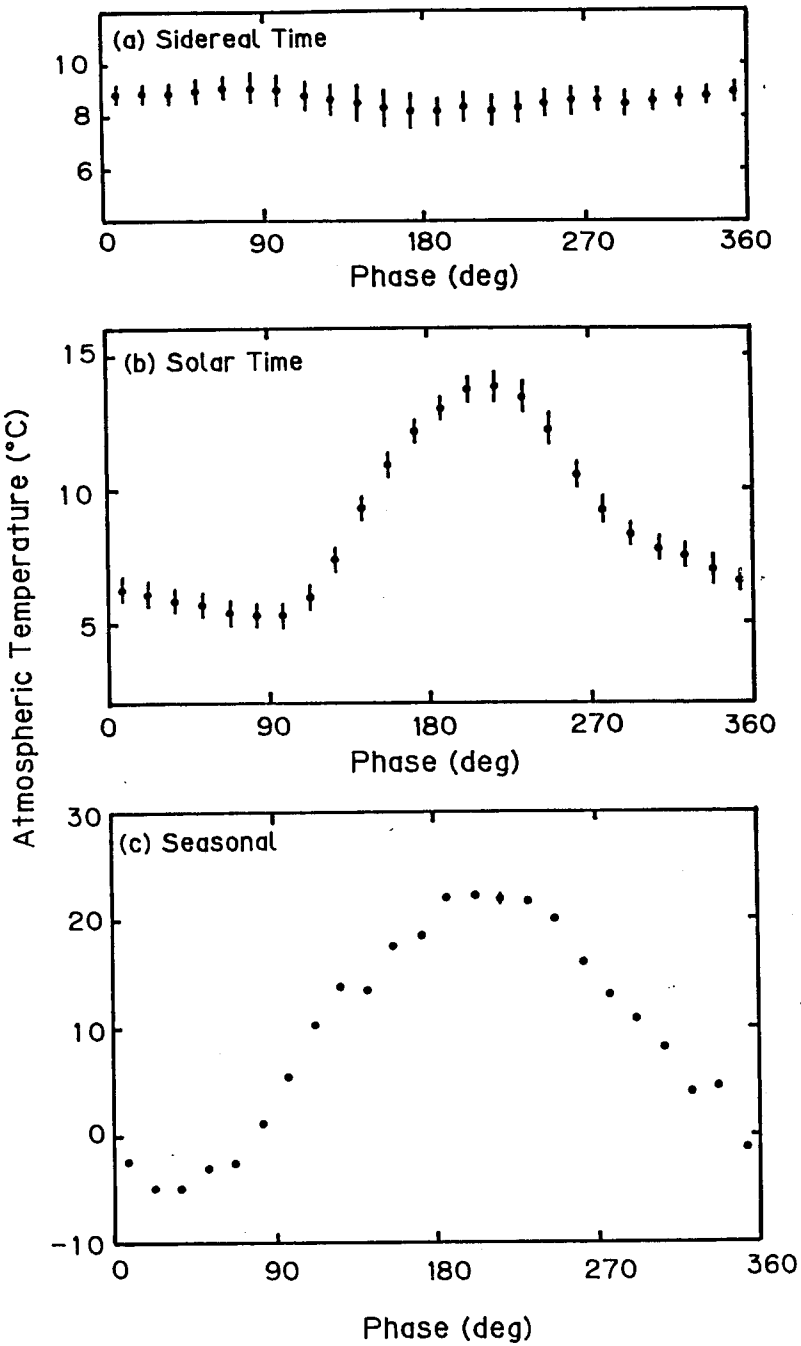
(a) Sidereal Time
10
8
6
0
90
180
270
360
Phase (deg)
(b) Solar Time
15
10
5
0
90
180
270
360
Phase (deg)
Atmospheric Temperature (°C)
(c) Seasonal
30
20
10
0
-10
0
90
180
270
360
Phase (deg)

Fig. 14

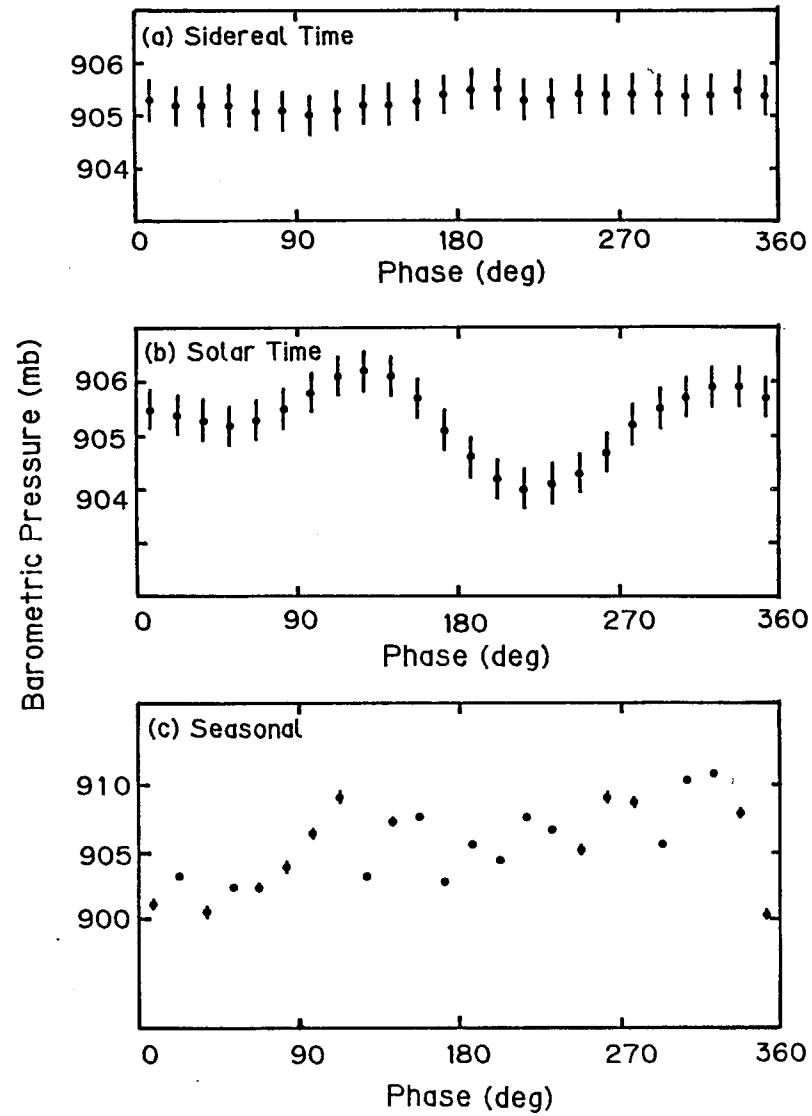
(a) Sidereal Time
906
905
904
0
90
180
270
360
Phase (deg)
(b) Solar Time
906
905
904
0
90
180
270
360
Phase (deg)
Barometric Pressure (mb)
(c) Seasonal
910
905
900
0
90
180
270
360
Phase (deg)

Fig. 15

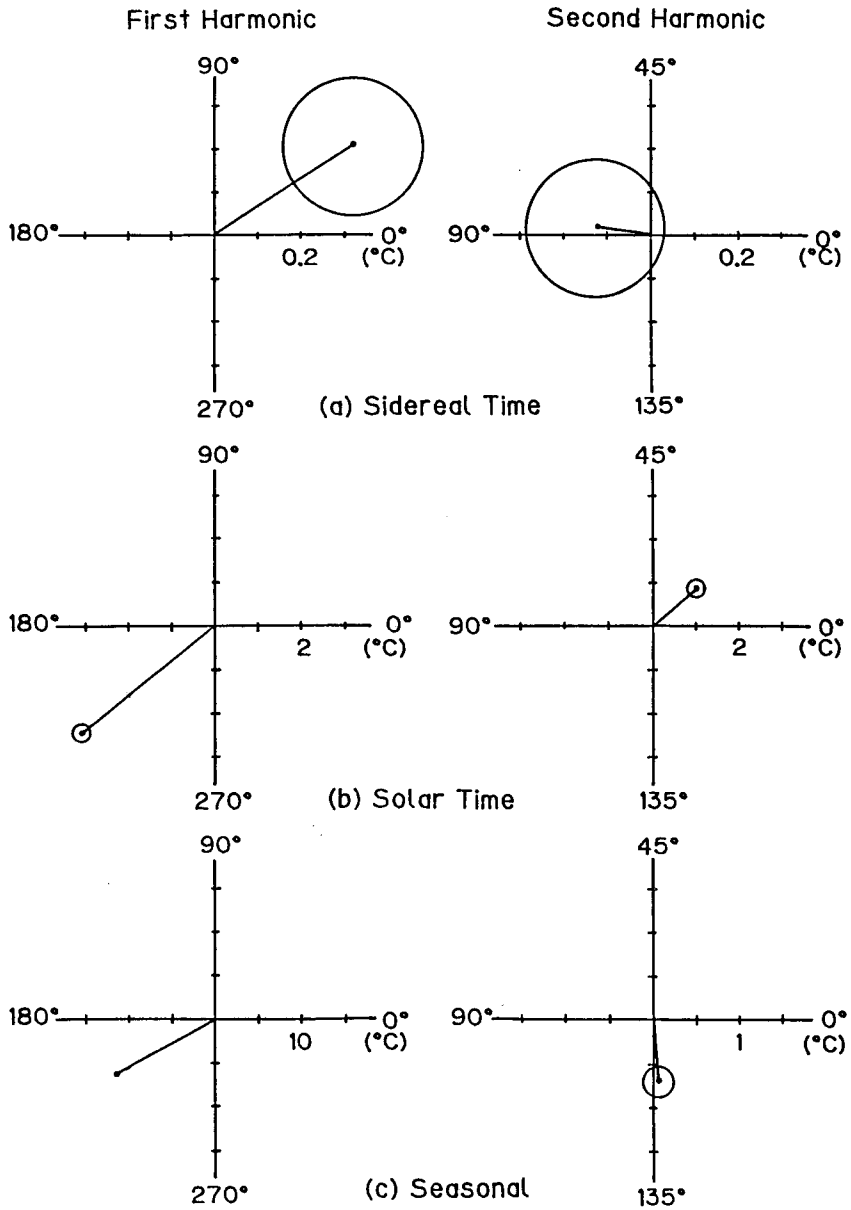
First Harmonic
Second Harmonic
90°
45°
180°
0°
0.2
(°C)
270°
135°
(a) Sidereal Time
2
(b) Solar Time
10
1
(c) Seasonal

Fig. 16

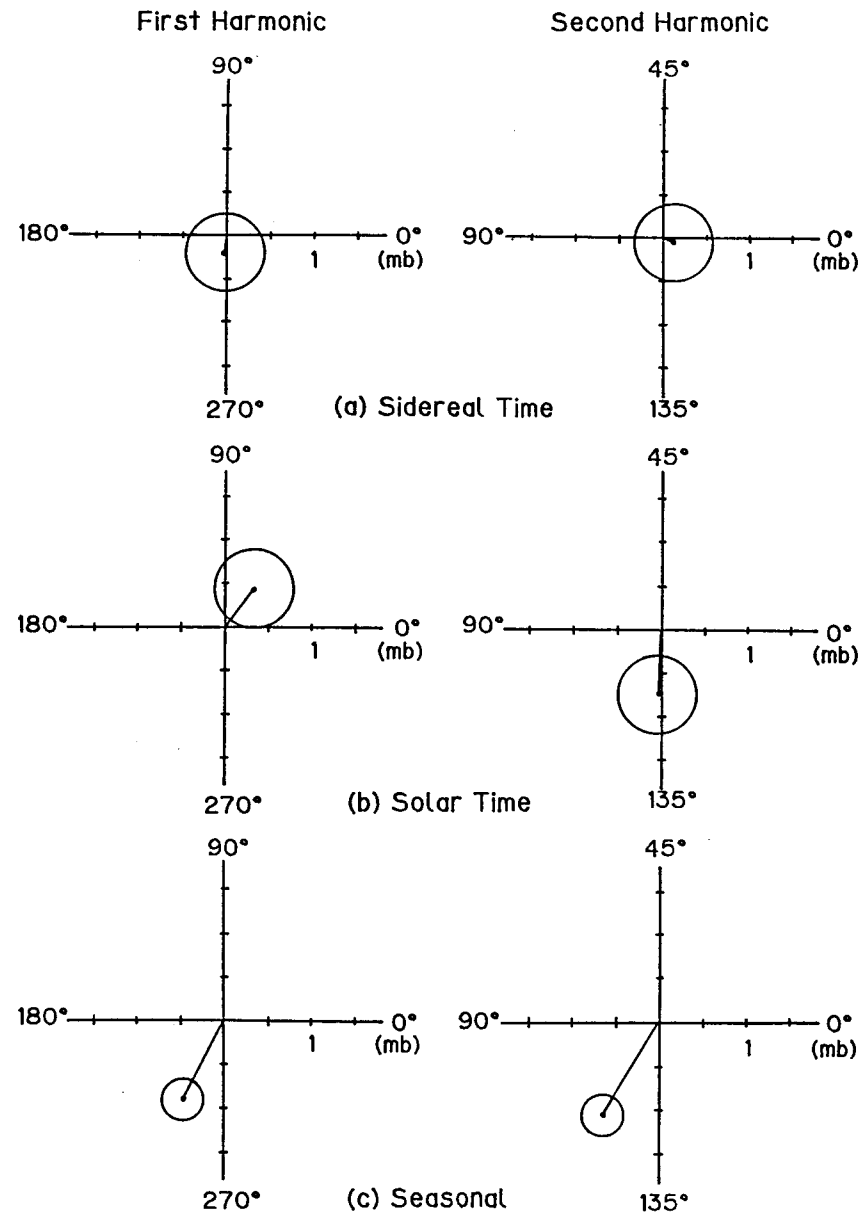
First Harmonic
Second Harmonic
90°
45°
180°
0°
1
(mb)
270°
135°
(a) Sidereal Time
(b) Solar Time
(c) Seasonal

Fig. 17

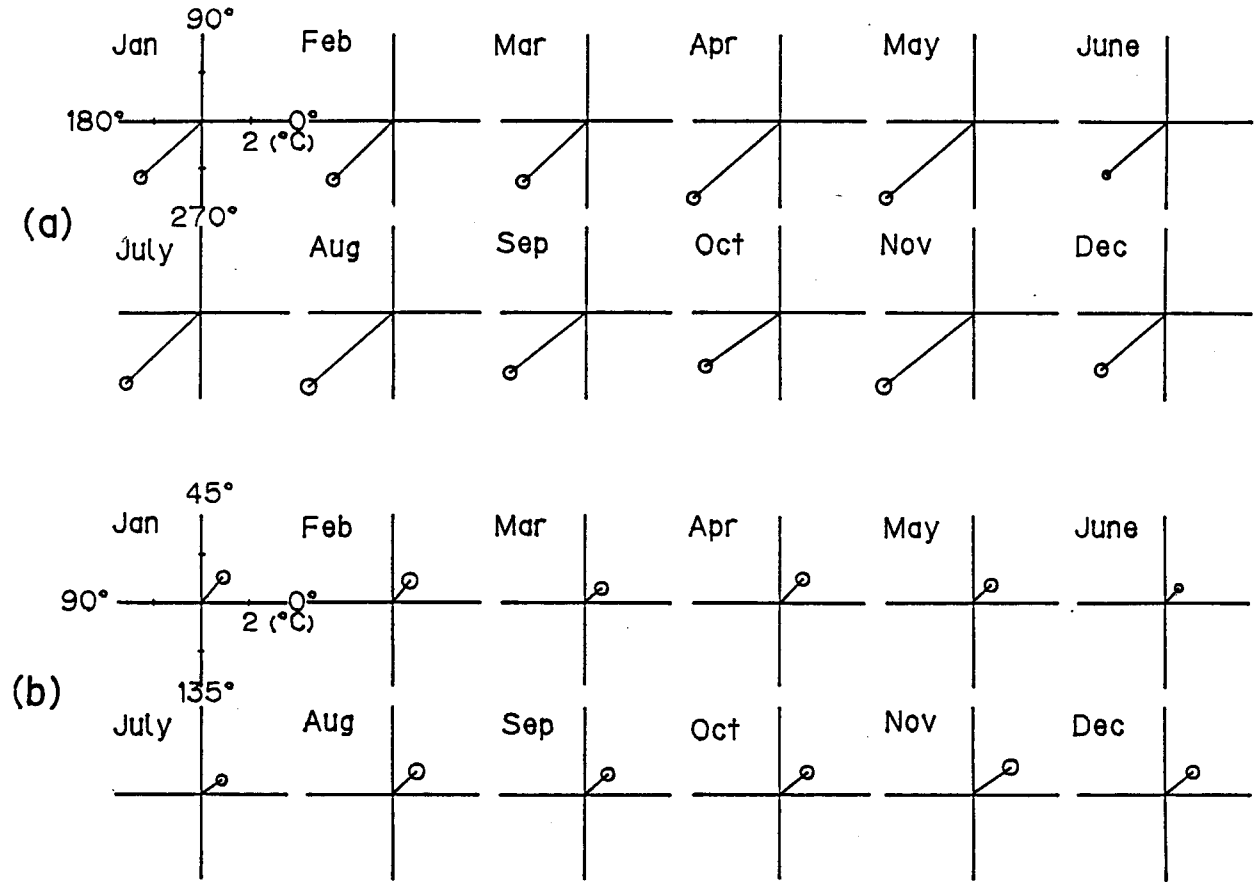
90°
Jan
Feb
Mar
Apr
May
June
180°
0°
2 (°C)
(a)
270°
July
Aug
Sep
Oct
Nov
Dec
45°
90°
135°
(b)

Fig. 18

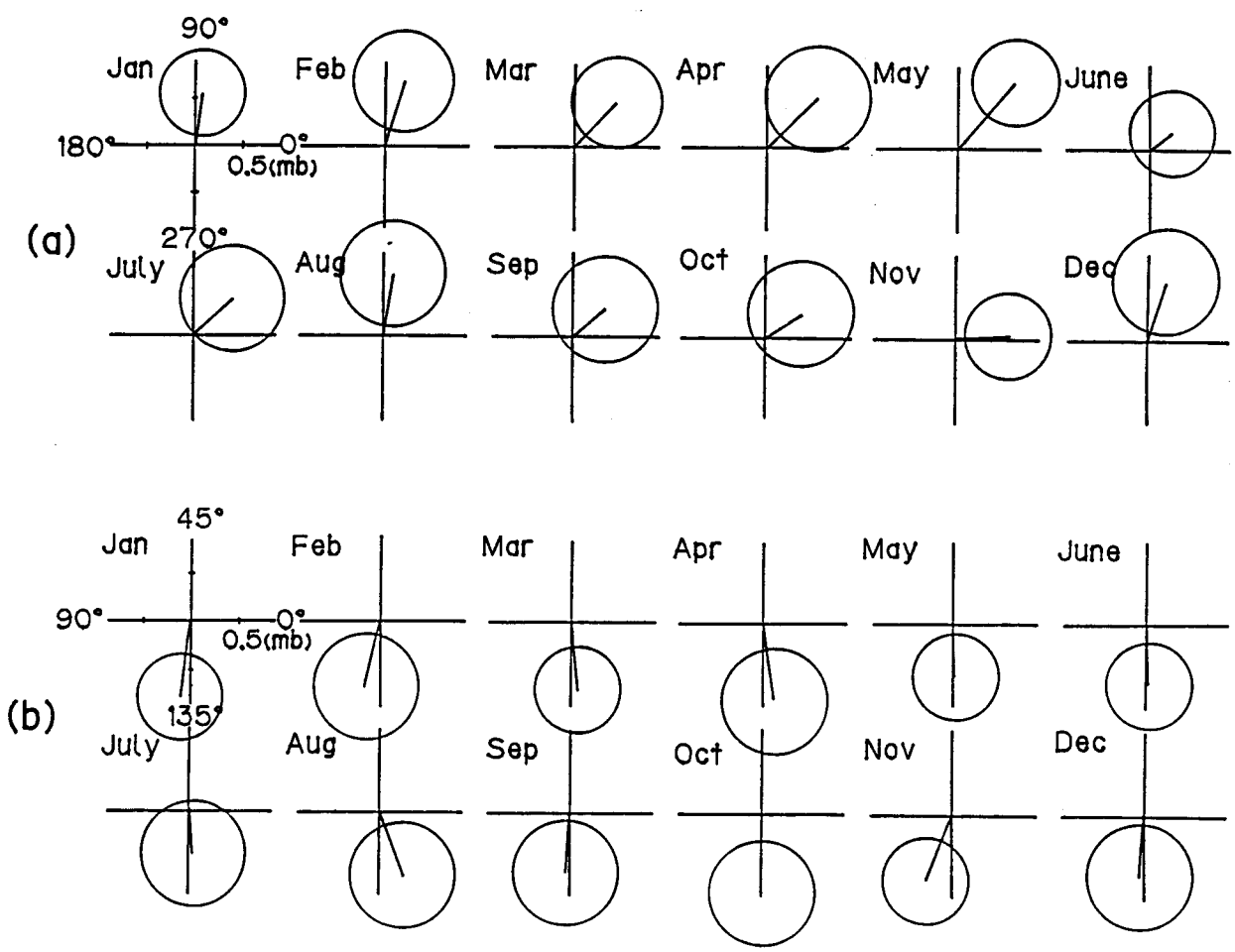
90°
Jan
Feb
Mar
Apr
May
June
180°
0°
0.5(mb)
(a)
270°
July
Aug
Sep
Oct
Nov
Dec
45°
90°
135°
(b)

Fig. 19

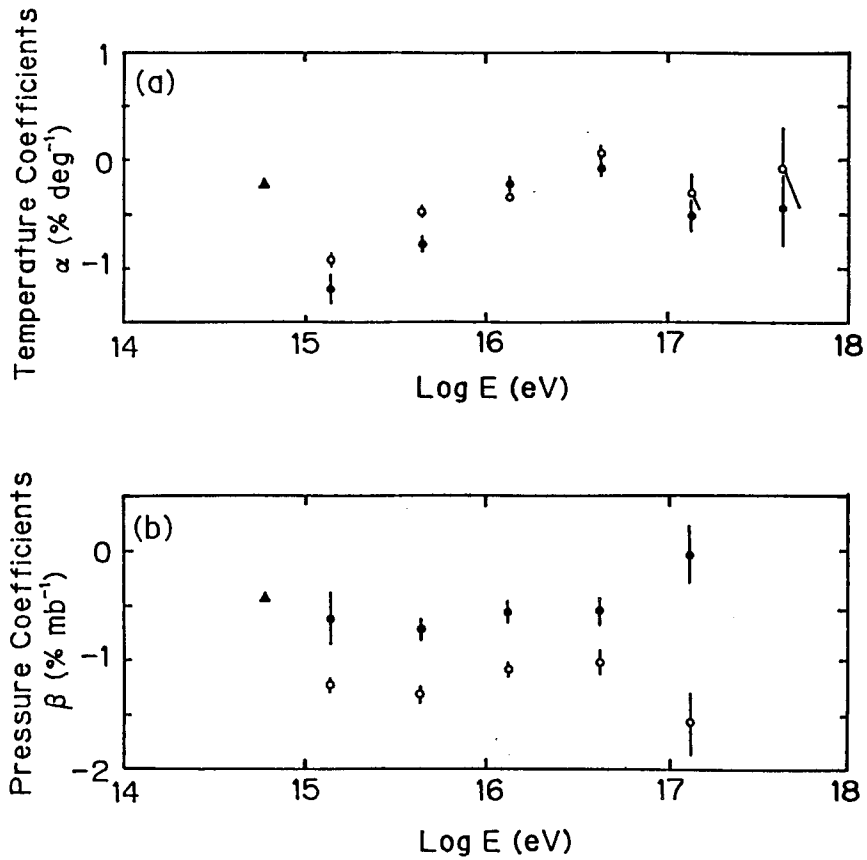
(a)
Temperature Coefficients
α (% deg⁻¹)
1
0
−1
14
15
16
17
18
Log E (eV)
(b)
Pressure Coefficients
β (% mb⁻¹)
0
−1
−2
14
15
16
17
18
Log E (eV)

Fig. 20

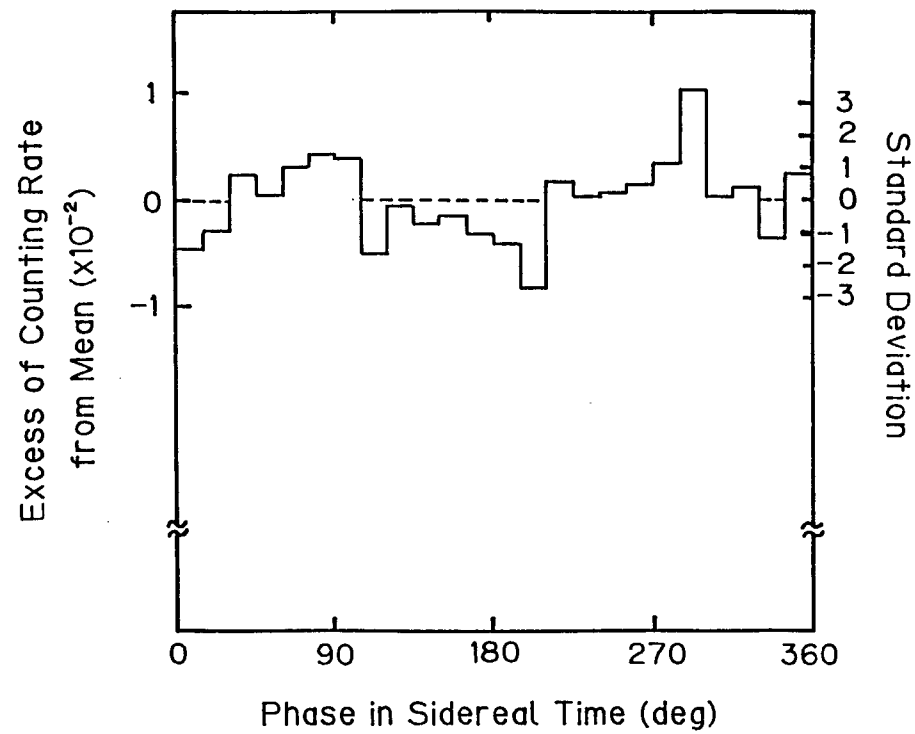
Excess of Counting Rate
from Mean (X10⁻²)
1
0
−1
Standard Deviation
3
2
1
0
−1
−2
−3
0
90
180
270
360
Phase in Sidereal Time (deg)

Fig. 21

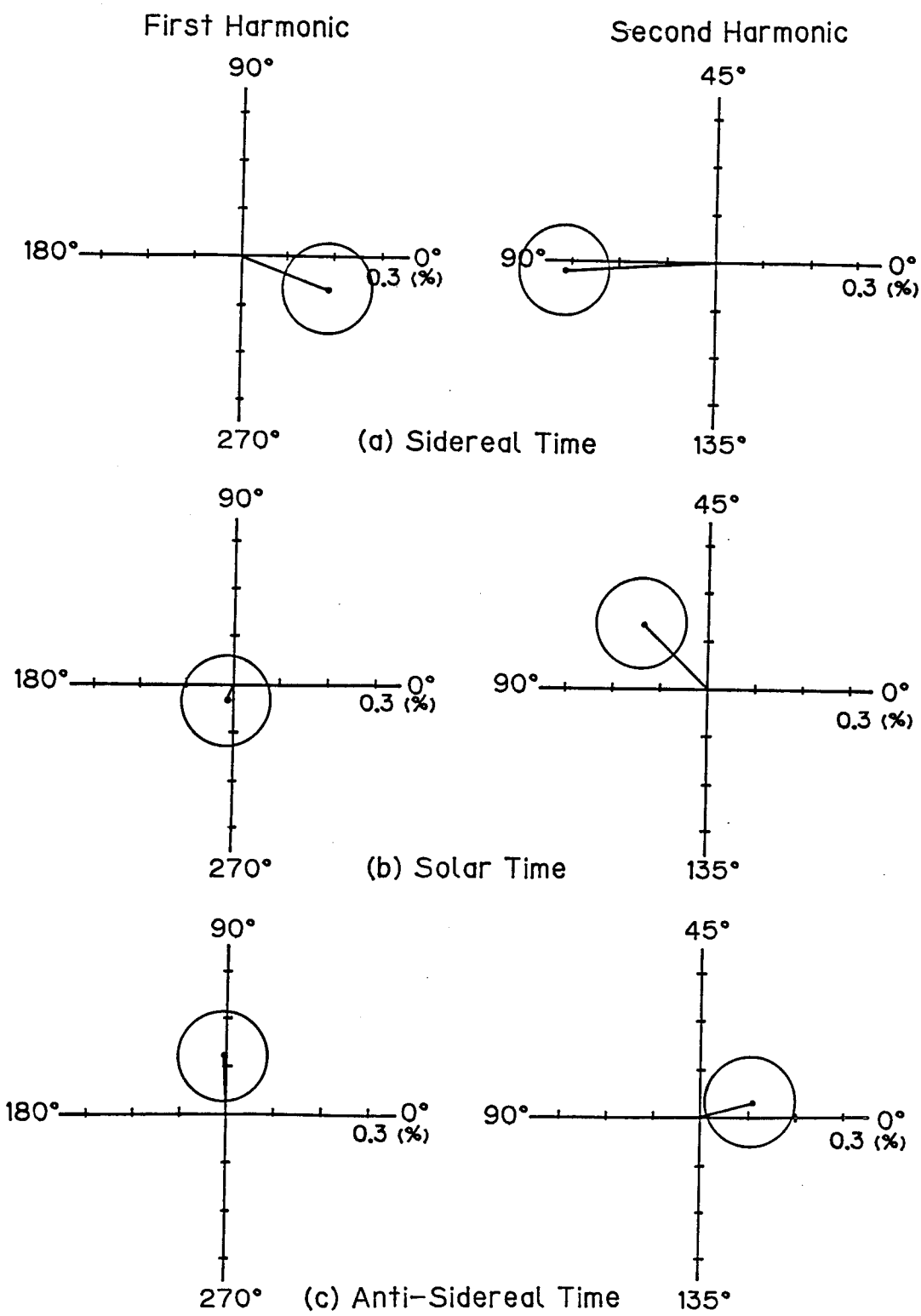
First Harmonic
Second Harmonic
90°
180°
0°
0.3 (%)
270°
45°
135°
(a) Sidereal Time
(b) Solar Time
(c) Anti-Sidereal Time

Fig. 22

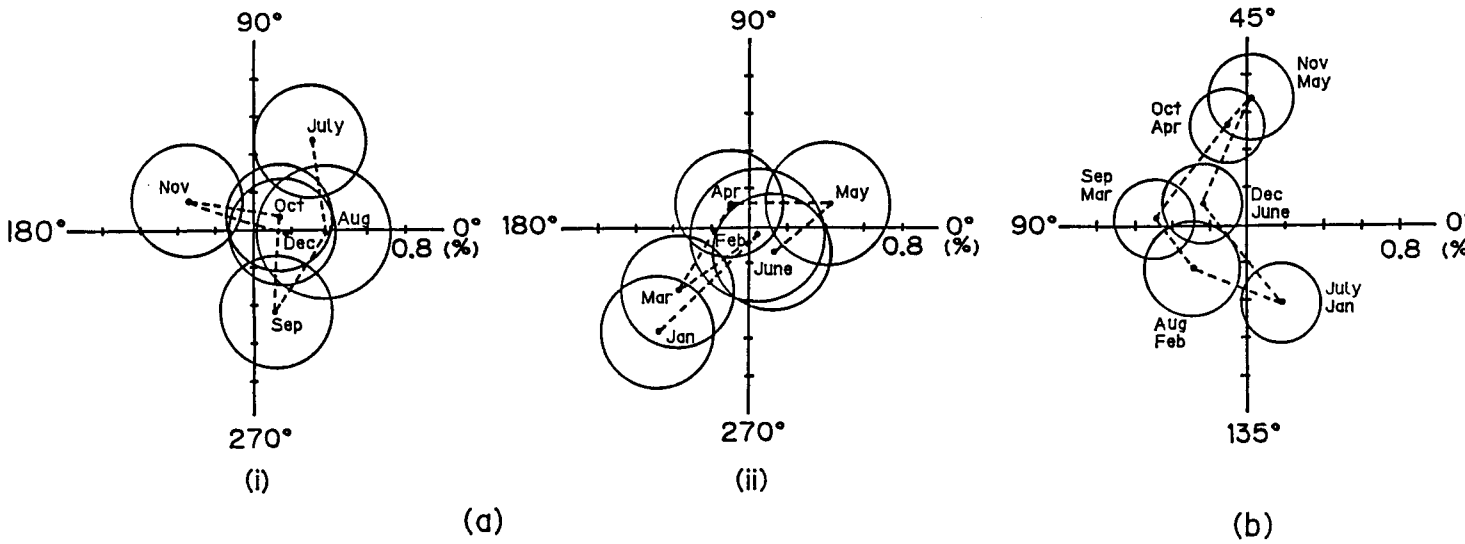
90°
July
Nov
Oct
Aug
180°
0°
0.8 (%)
Dec
Sep
270°
(i)
90°
Apr
May
180°
0°
0.8 (%)
Feb
June
Mar
Jan
270°
(ii)
(a)
45°
Nov
May
Oct
Apr
Sep
Mar
Dec
June
90°
0°
0.8 (%)
July
Jan
Aug
Feb
135°
(b)

Fig. 23

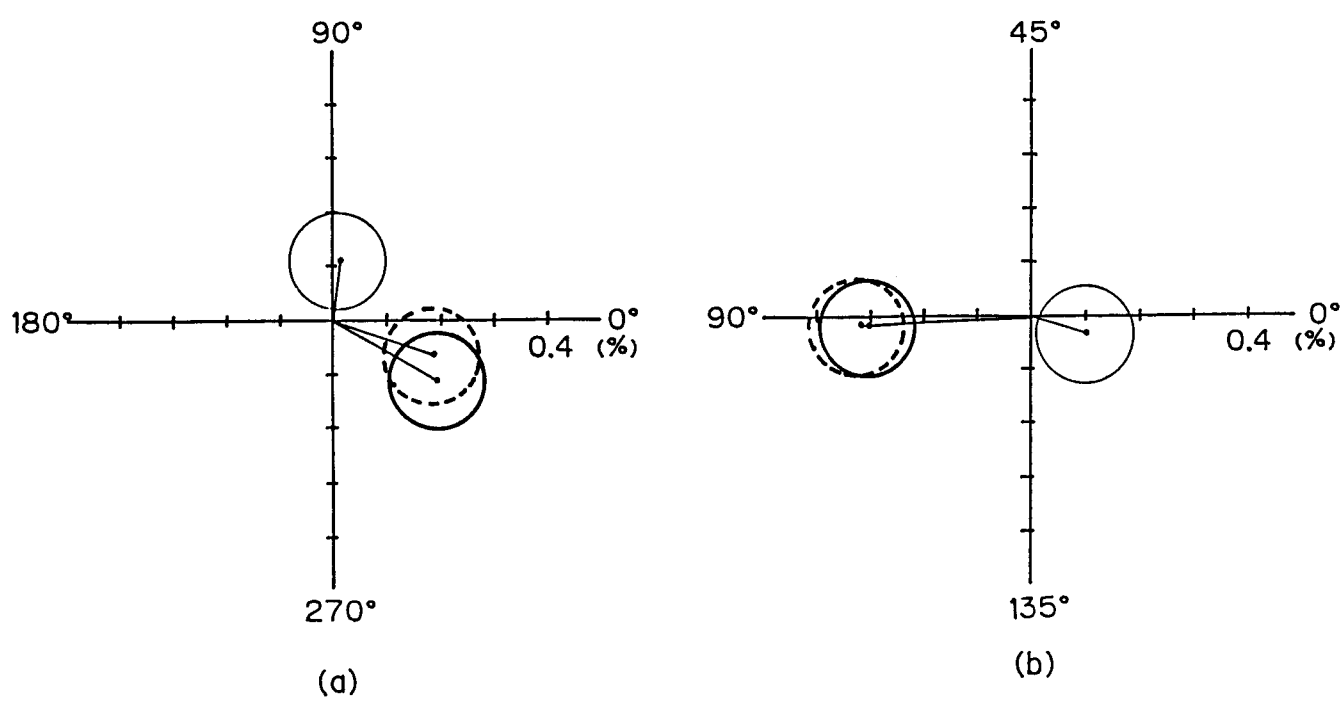
90°
180°
0°
0.4 (%)
270°
(a)
45°
90°
0°
0.4 (%)
135°
(b)

Fig. 24

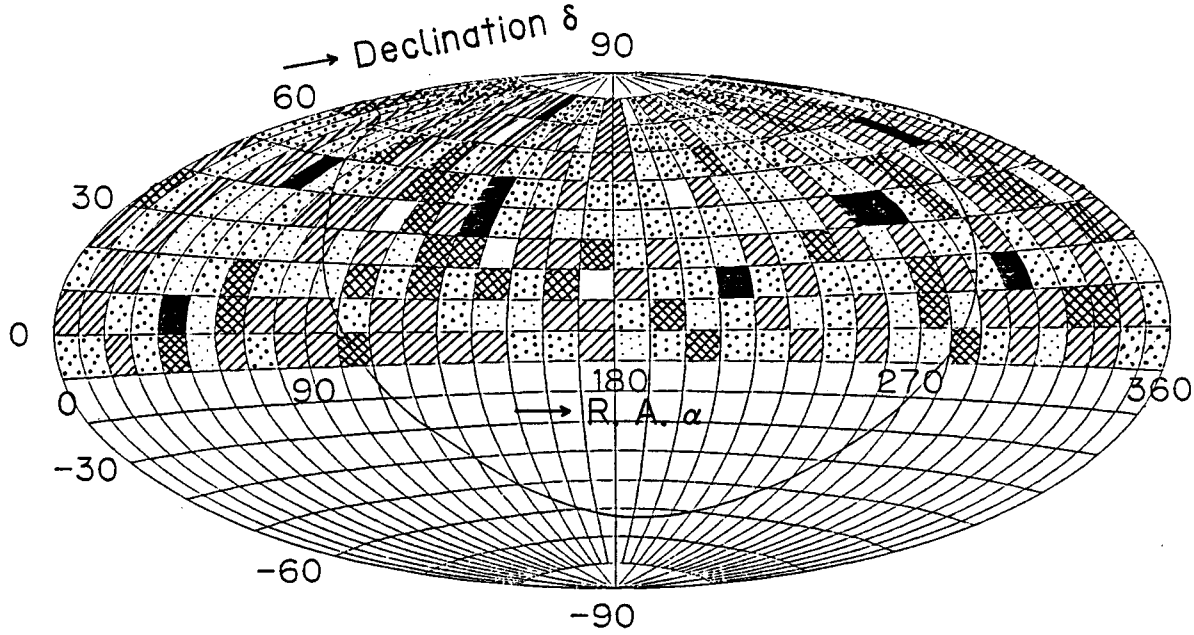
Declination δ
90
60
30
0
-30
-60
-90
0
90
180
270
360
R. A. α

(a)

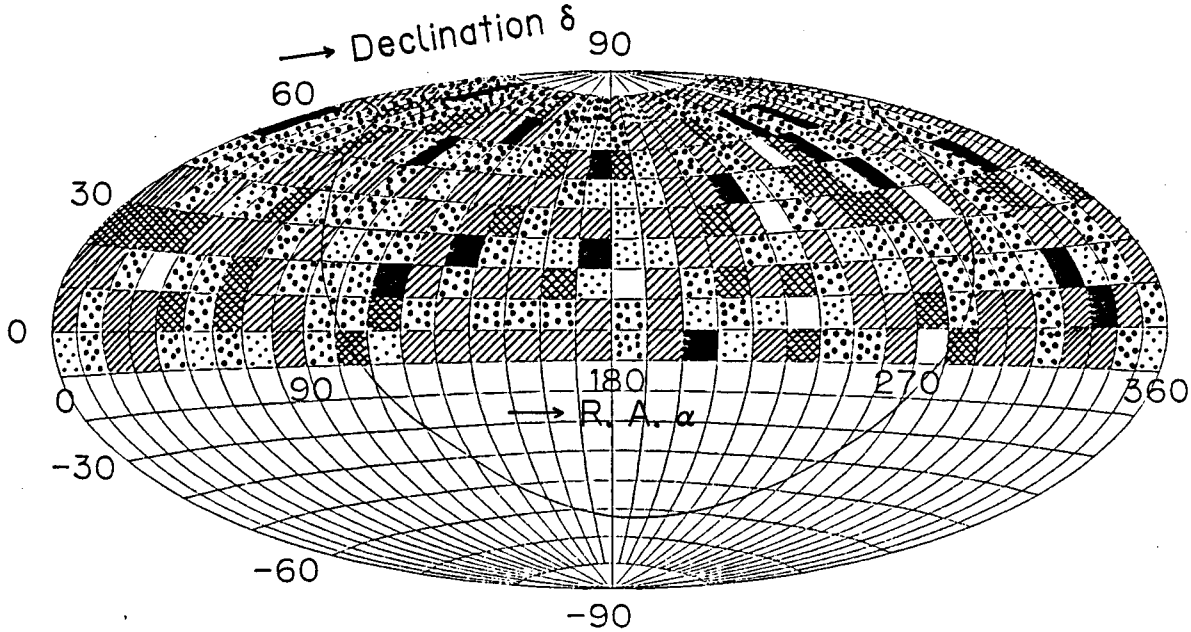
Declination δ
90
60
30
0
-30
-60
-90
0
90
180
270
360
R. A. α

(b)

Fig. 25

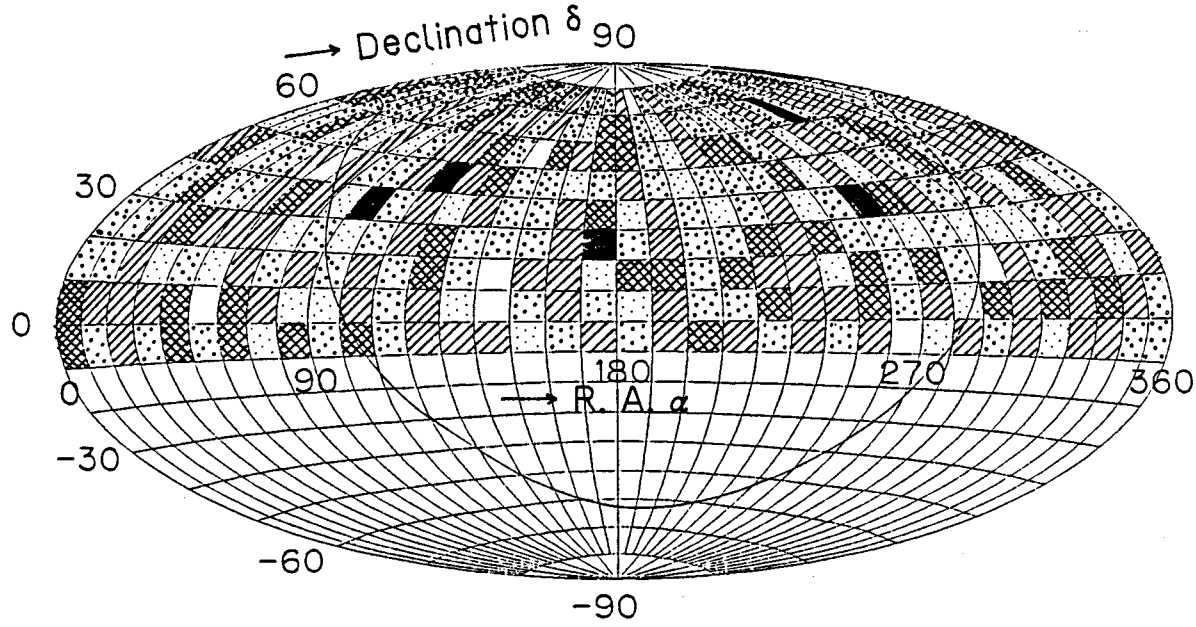
Declination δ
90
60
30
0
-30
-60
-90
0
90
180
270
360
R. A. α

(a)

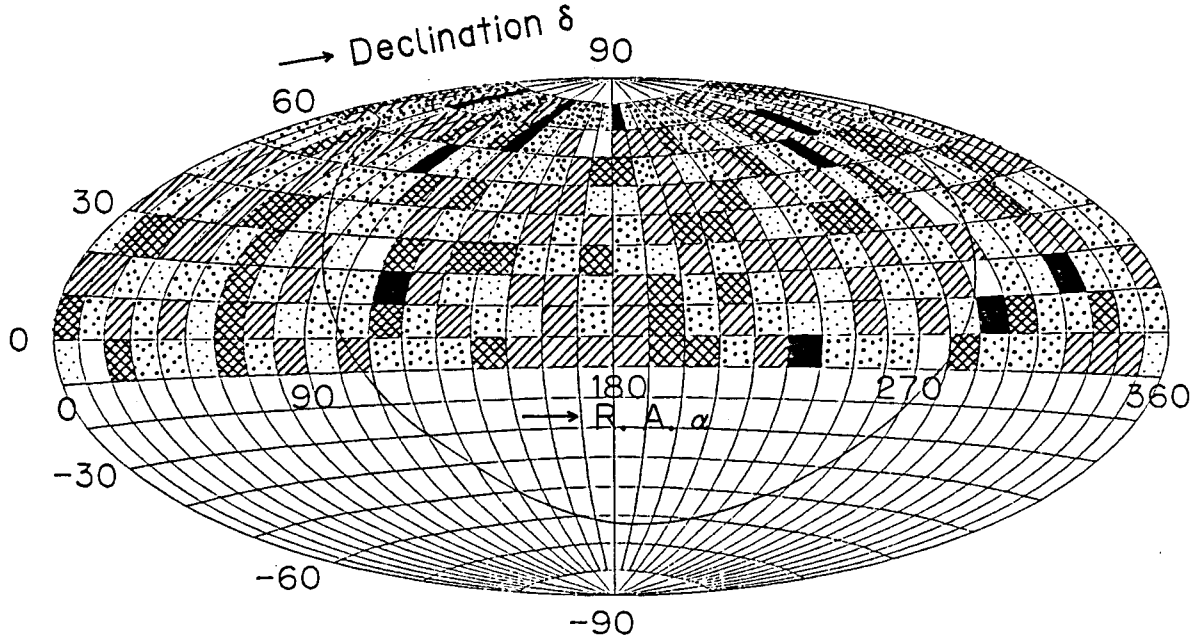
Declination δ
90
60
30
0
-30
-60
-90
0
90
180
270
360
R. A. α

(b)

Fig. 26

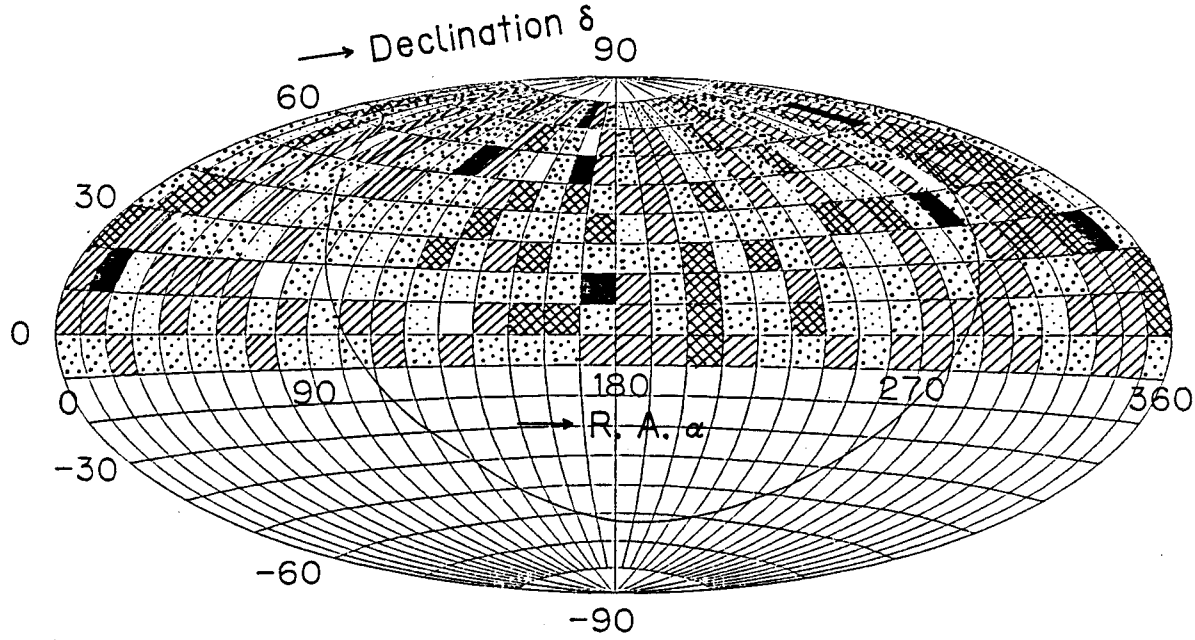

Fig. 27

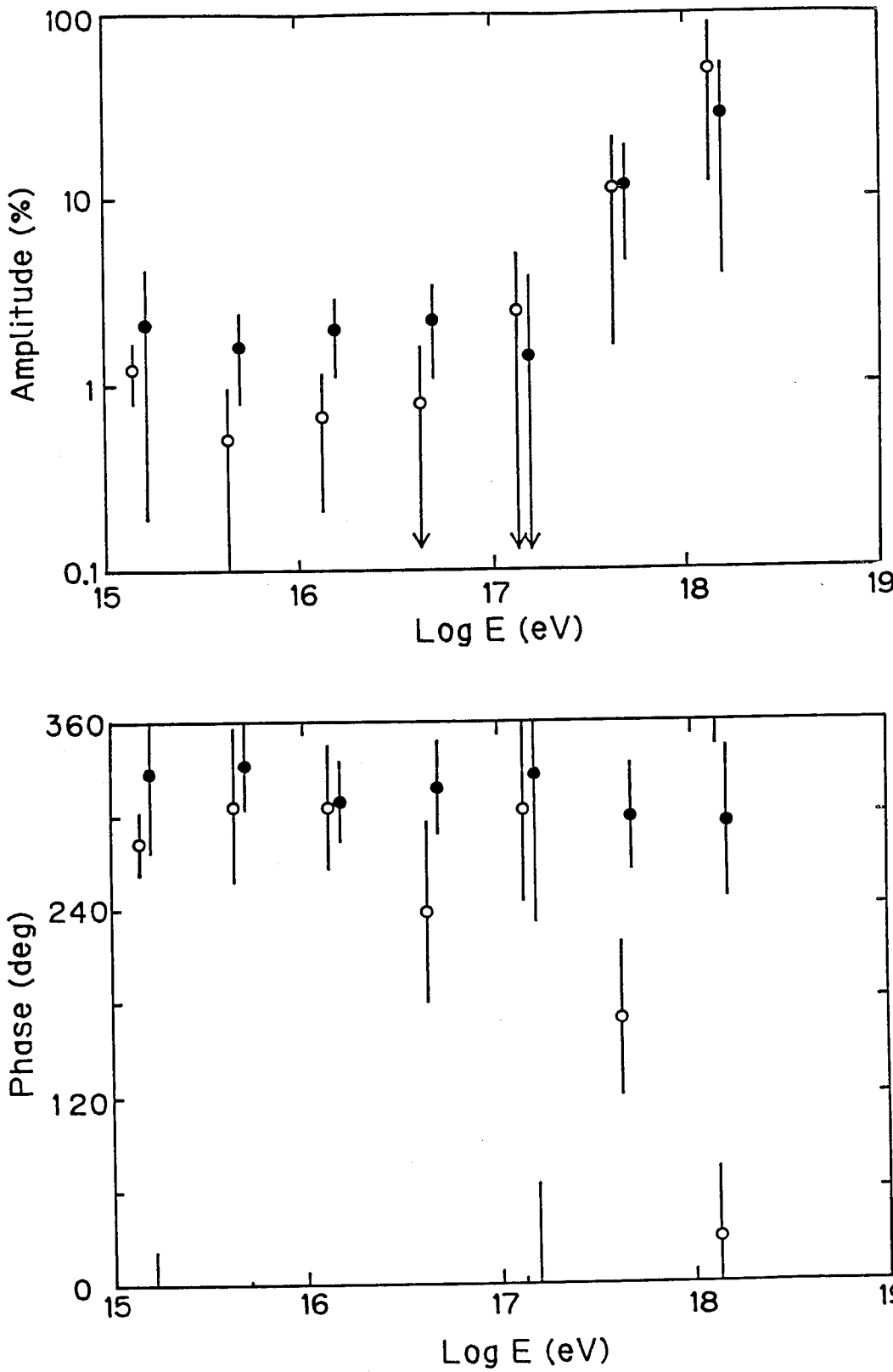
100
10
1
0.1
Amplitude (%)
15
16
17
18
19
Log E (eV)
360
240
120
0
Phase (deg)
15
16
17
18
19
Log E (eV)

Fig. 28(a)

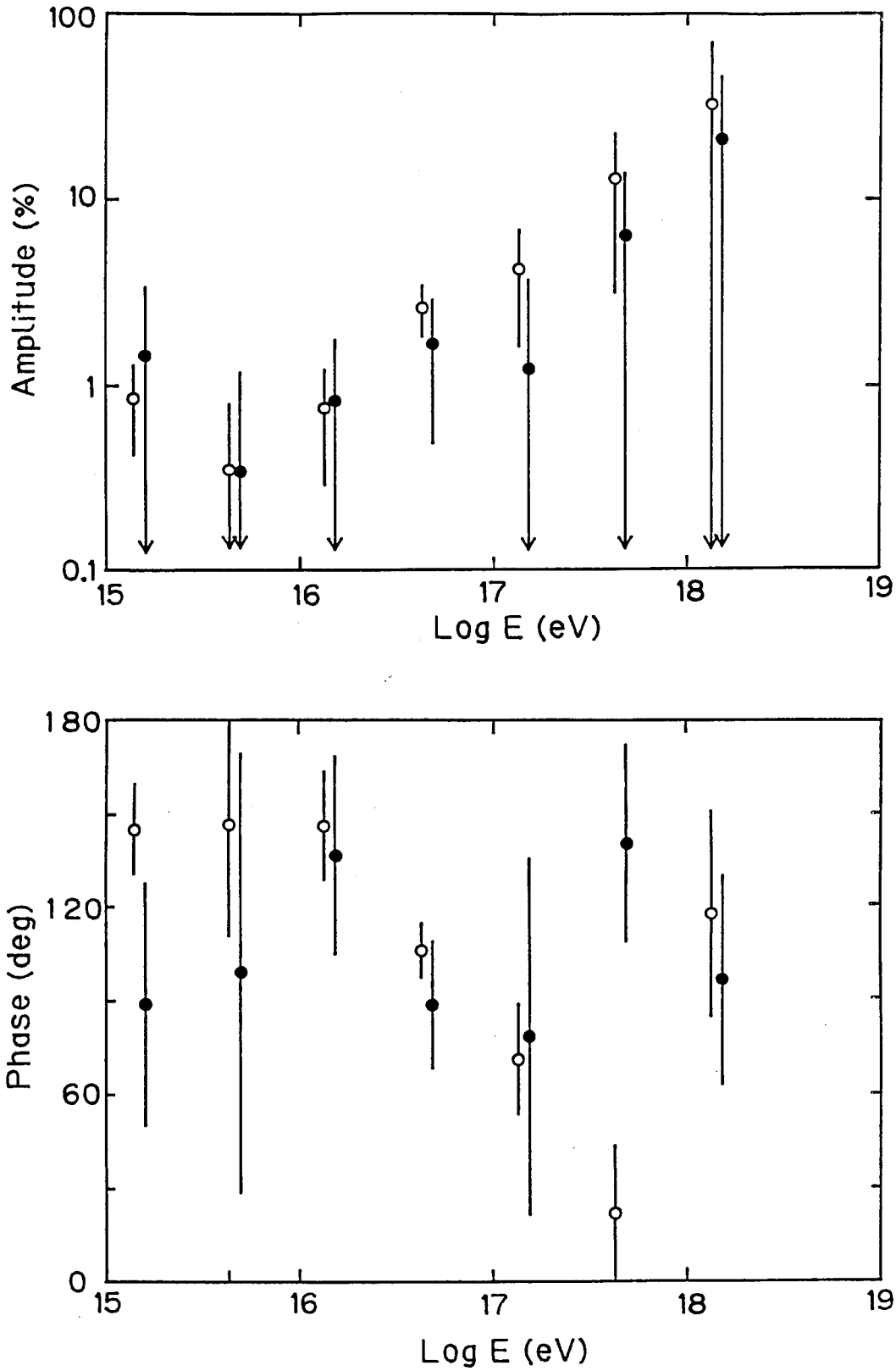
100
10
1
0.1
Amplitude (%)
15
16
17
18
19
Log E (eV)
180
120
60
0
Phase (deg)
15
16
17
18
19
Log E (eV)

Fig. 28(b)

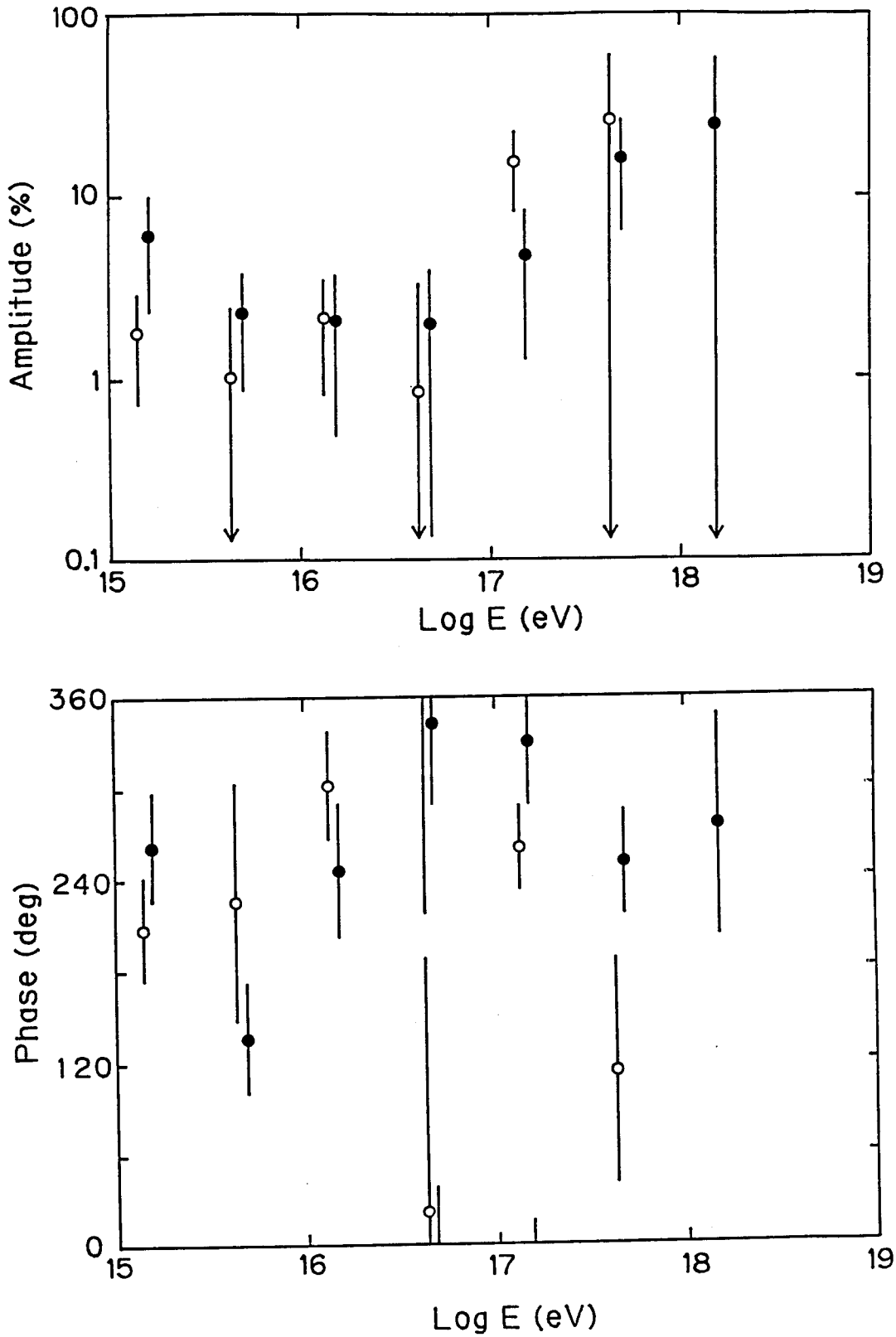
100
10
1
0.1
Amplitude (%)
15
16
17
18
19
Log E (eV)
360
240
120
0
Phase (deg)
15
16
17
18
19
Log E (eV)

Fig. 29(a)

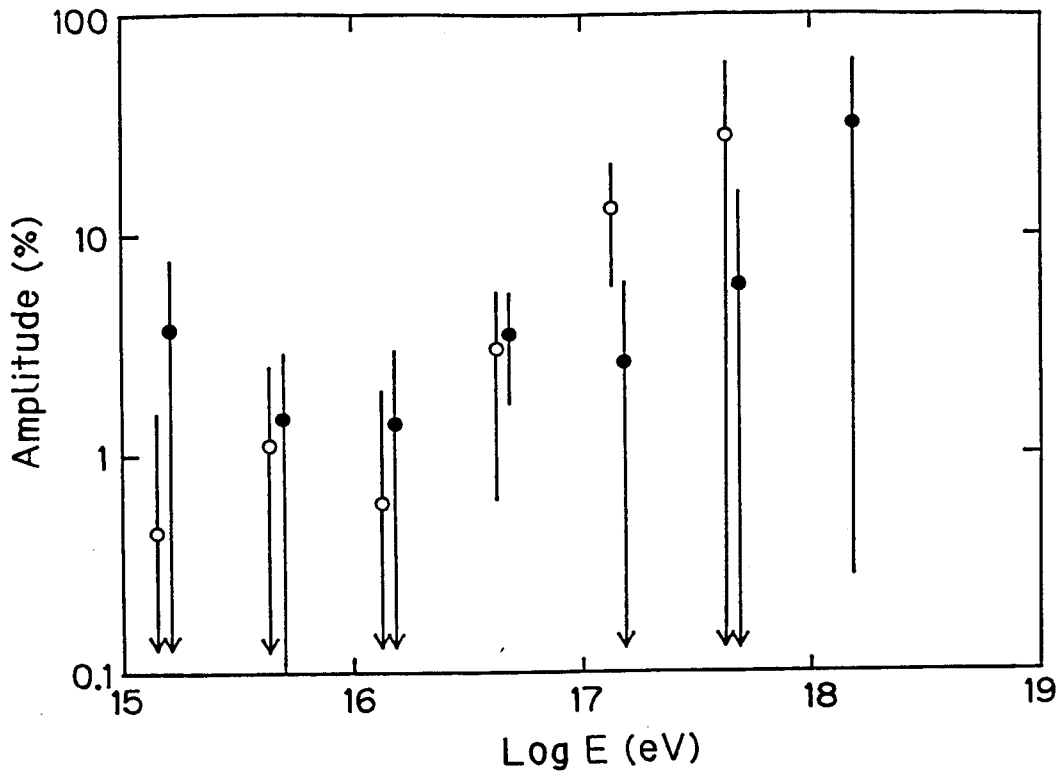
100
10
1
0.1
Amplitude (%)
15
16
17
18
19
Log E (eV)

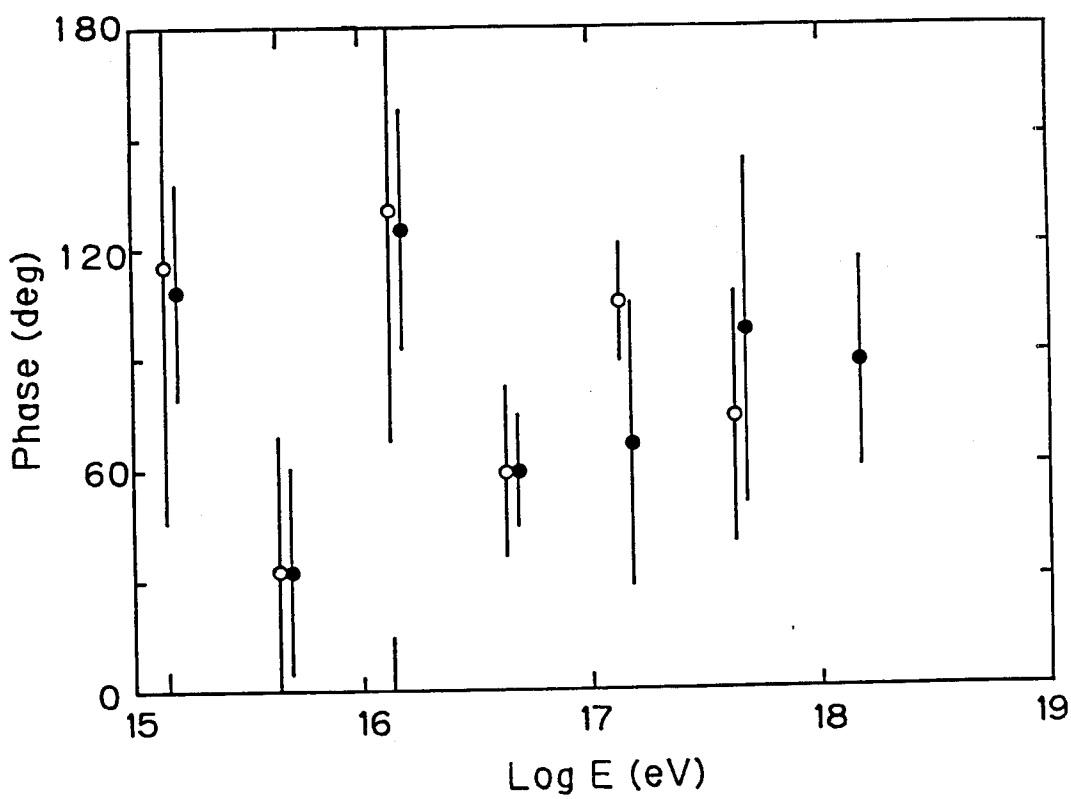
180
120
60
0
Phase (deg)
15
16
17
18
19
Log E (eV)

Fig. 29(b)

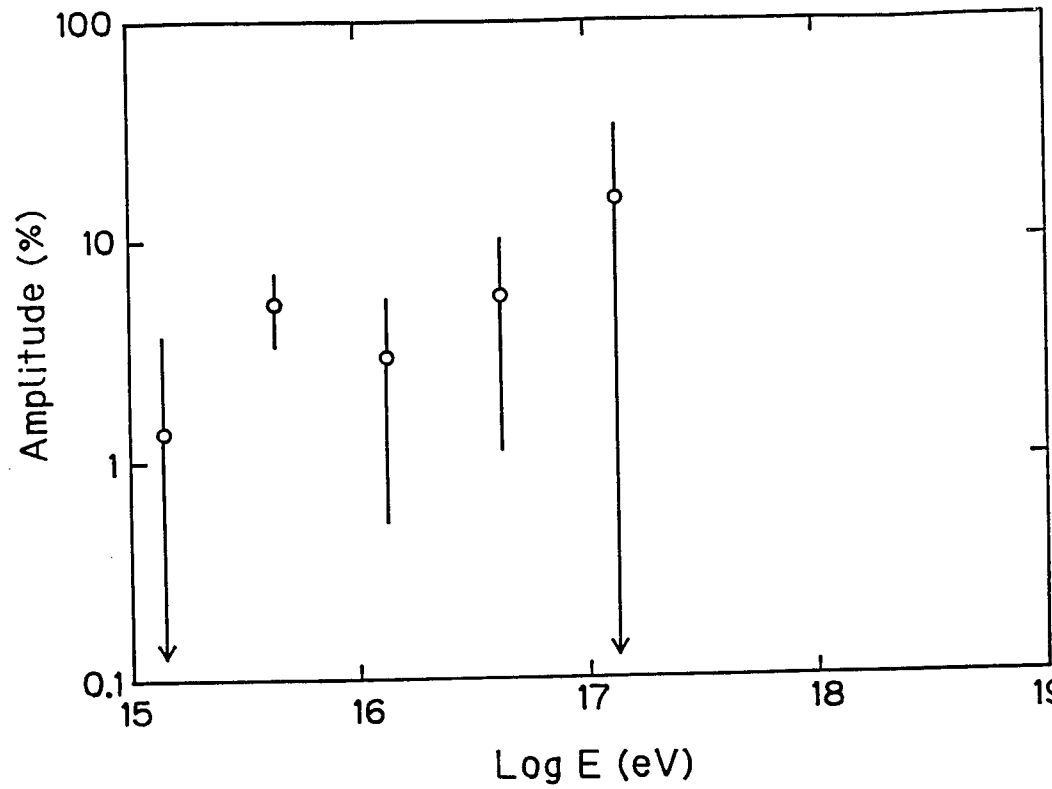
100
10
1
0.1
Amplitude (%)
15
16
17
18
19
Log E (eV)

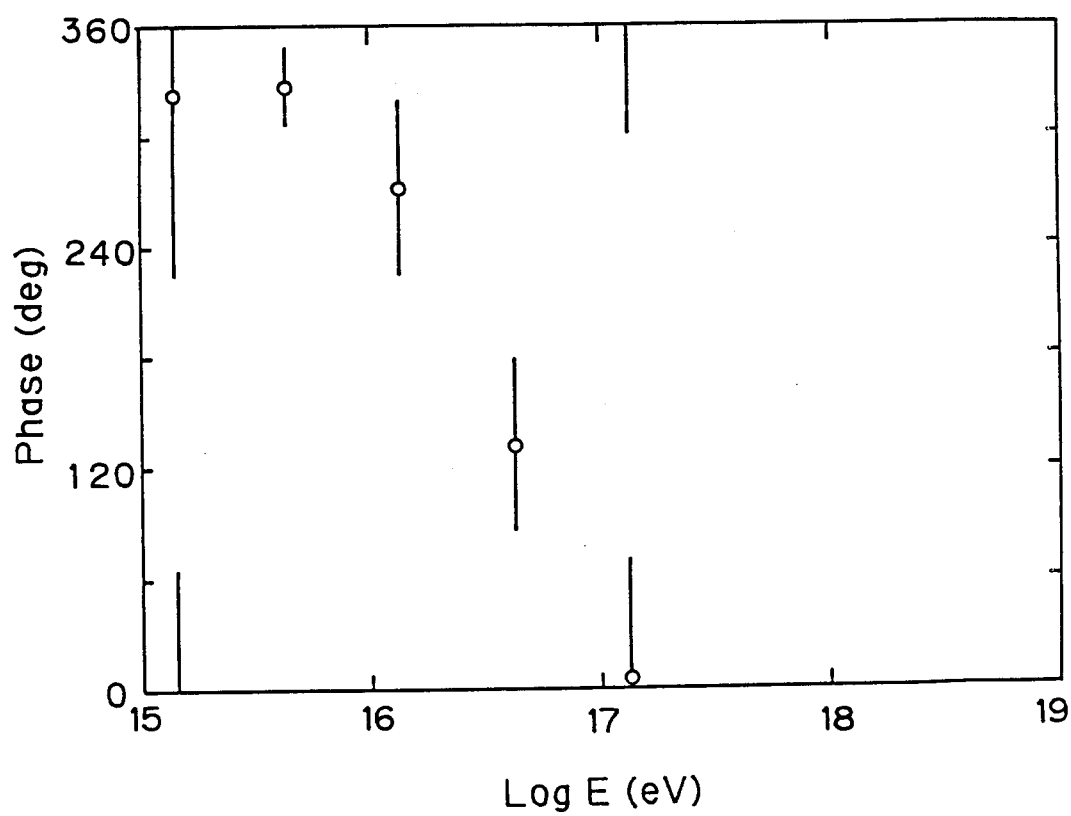
360
240
120
0
Phase (deg)
15
16
17
18
19
Log E (eV)

Fig. 30(a)

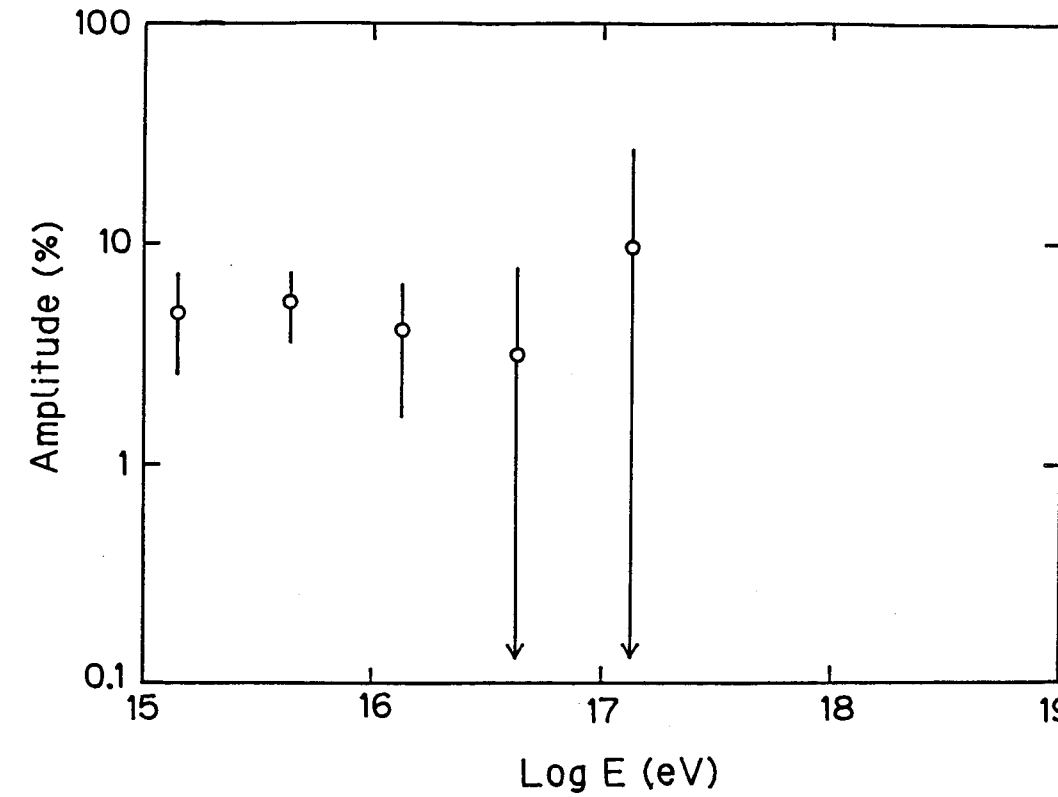
100
10
1
0.1
Amplitude (%)
15
16
17
18
19
Log E (eV)

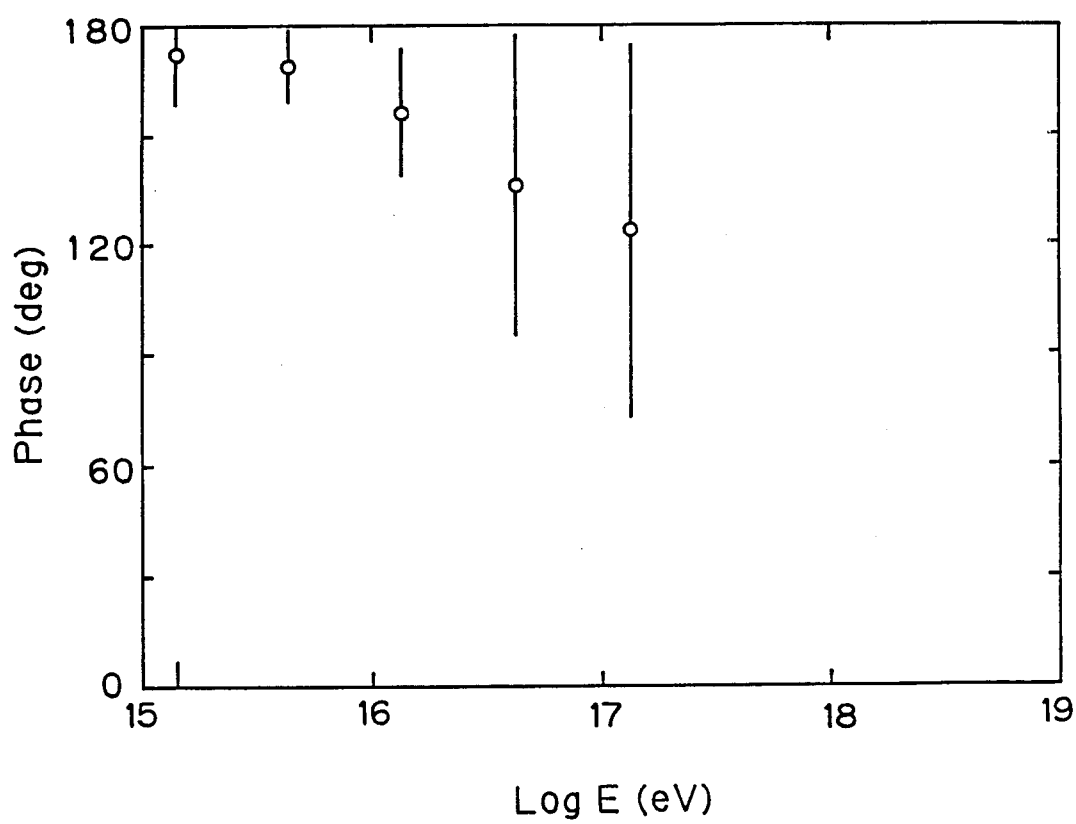
180
120
60
0
Phase (deg)
15
16
17
18
19
Log E (eV)

Fig. 30(b)

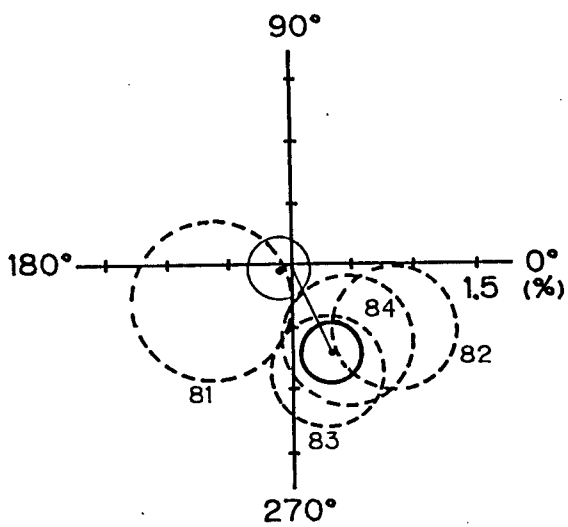

E = 1x10^{15}~3.2x10^{16}eV
1st harmonic
All showers (CE)

(a)

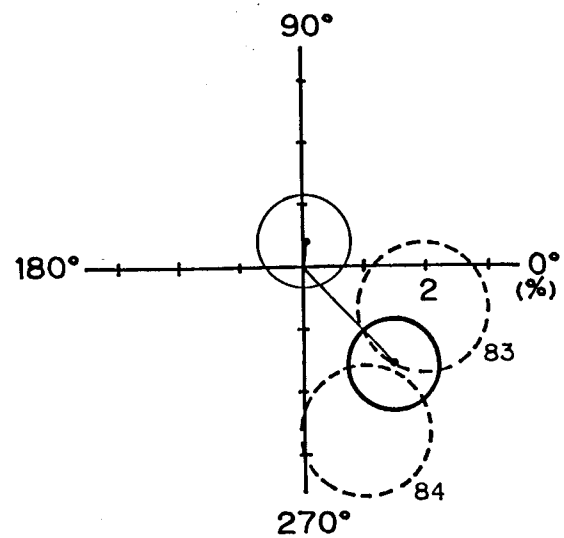

E = 1x10^{16}~1x10^{17}eV
1st harmonic
All showers (CM)

(b)

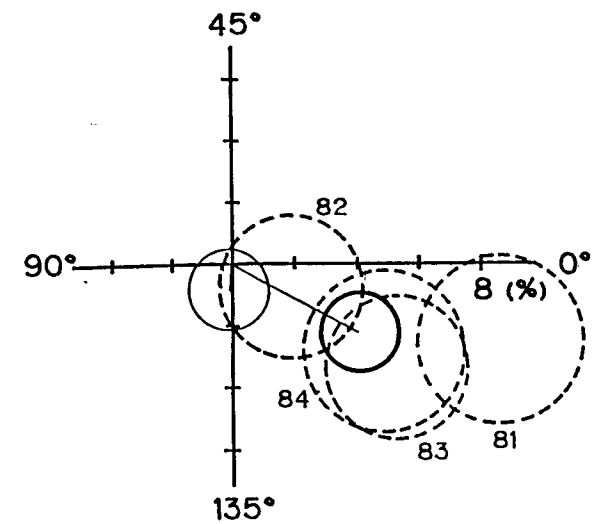

E = 1x10^{15}~1x10^{17}eV
2nd harmonic
muon-poor showers(CE)

(c)

Fig. 31

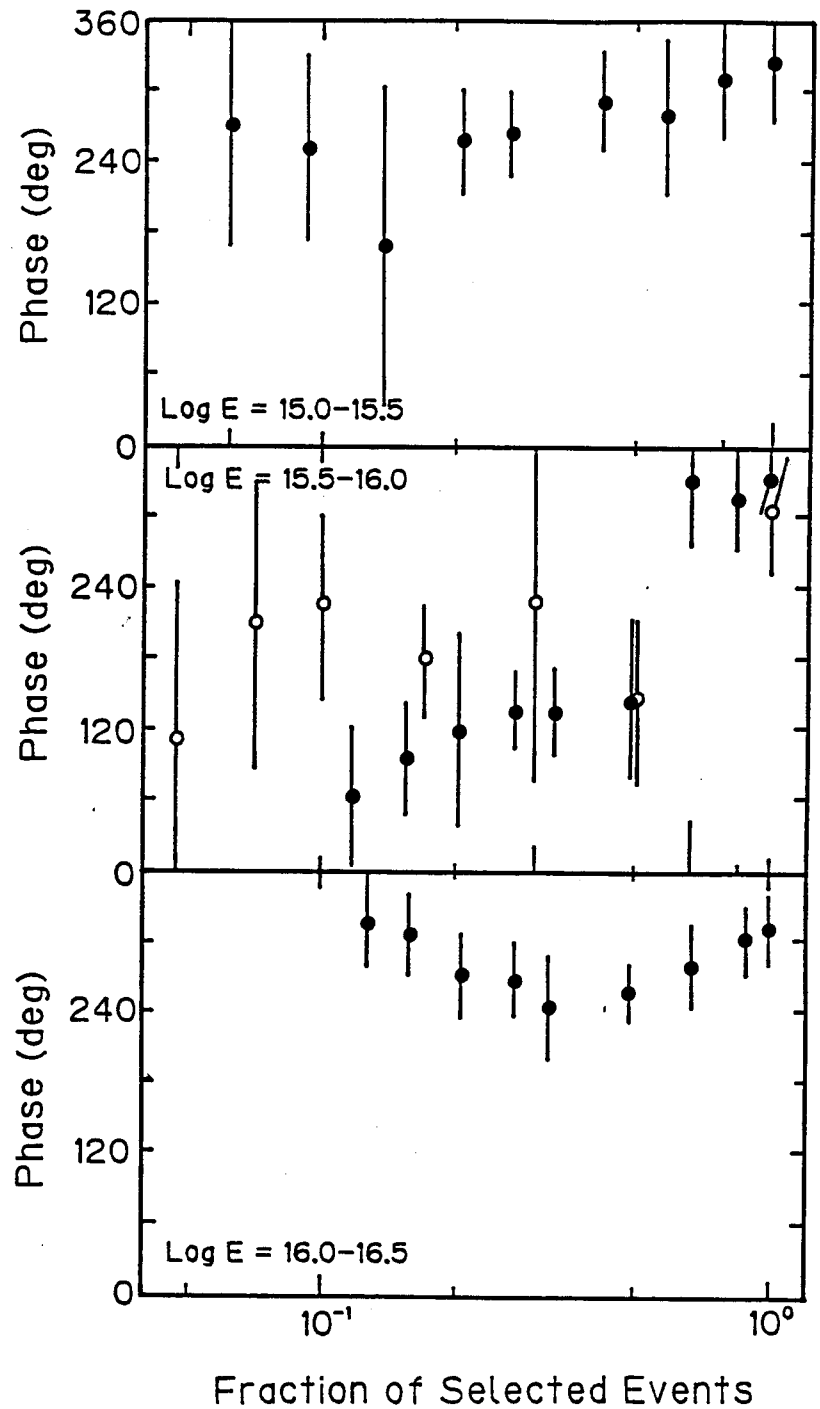
360
240
120
0
Phase (deg)
Log E = 15.0–15.5
Log E = 15.5–16.0
Log E = 16.0–16.5
10^{-1}
10^{0}
Fraction of Selected Events

Fig. 32

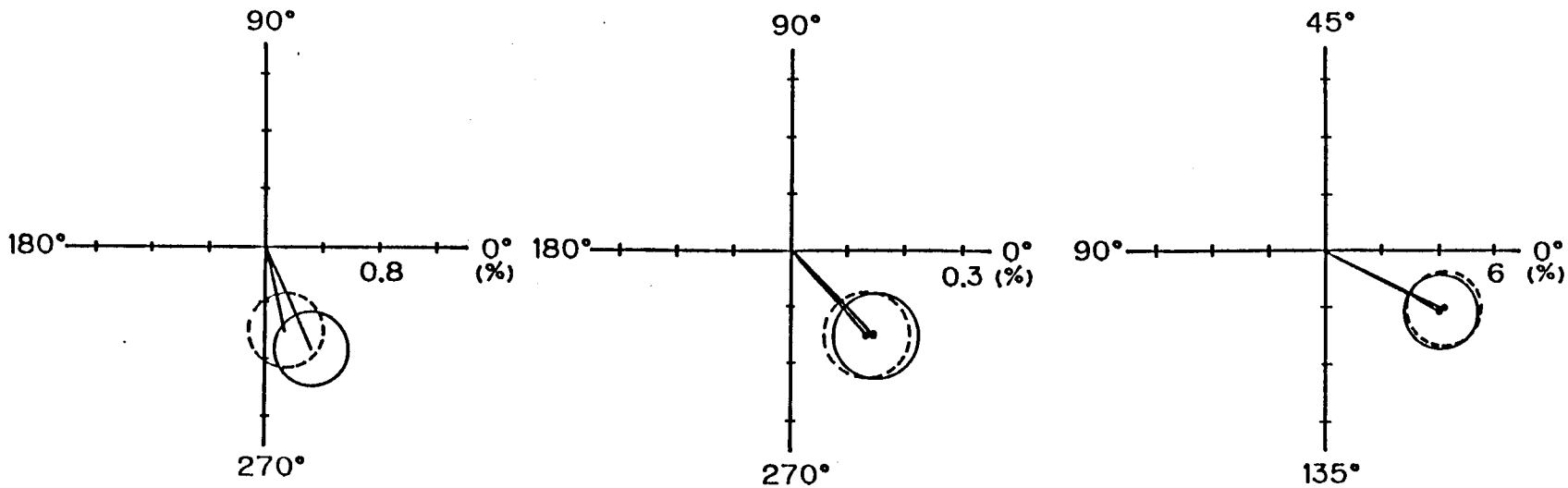
90°
180°
0°
0.8
(%)
270°
E = 1x10¹⁵~3.2x10¹⁶eV
1st harmonic
All showers (CE)
(a)
90°
180°
0°
0.3 (%)
270°
E = 1x10¹⁶~1x10¹⁷eV
1st harmonic
All showers (CM)
(b)
45°
90°
0°
6 (%)
135°
E = 1x10¹⁶~1x10¹⁷eV
2nd harmonic
muon-poor showers(CE)
(c)

Fig. 33

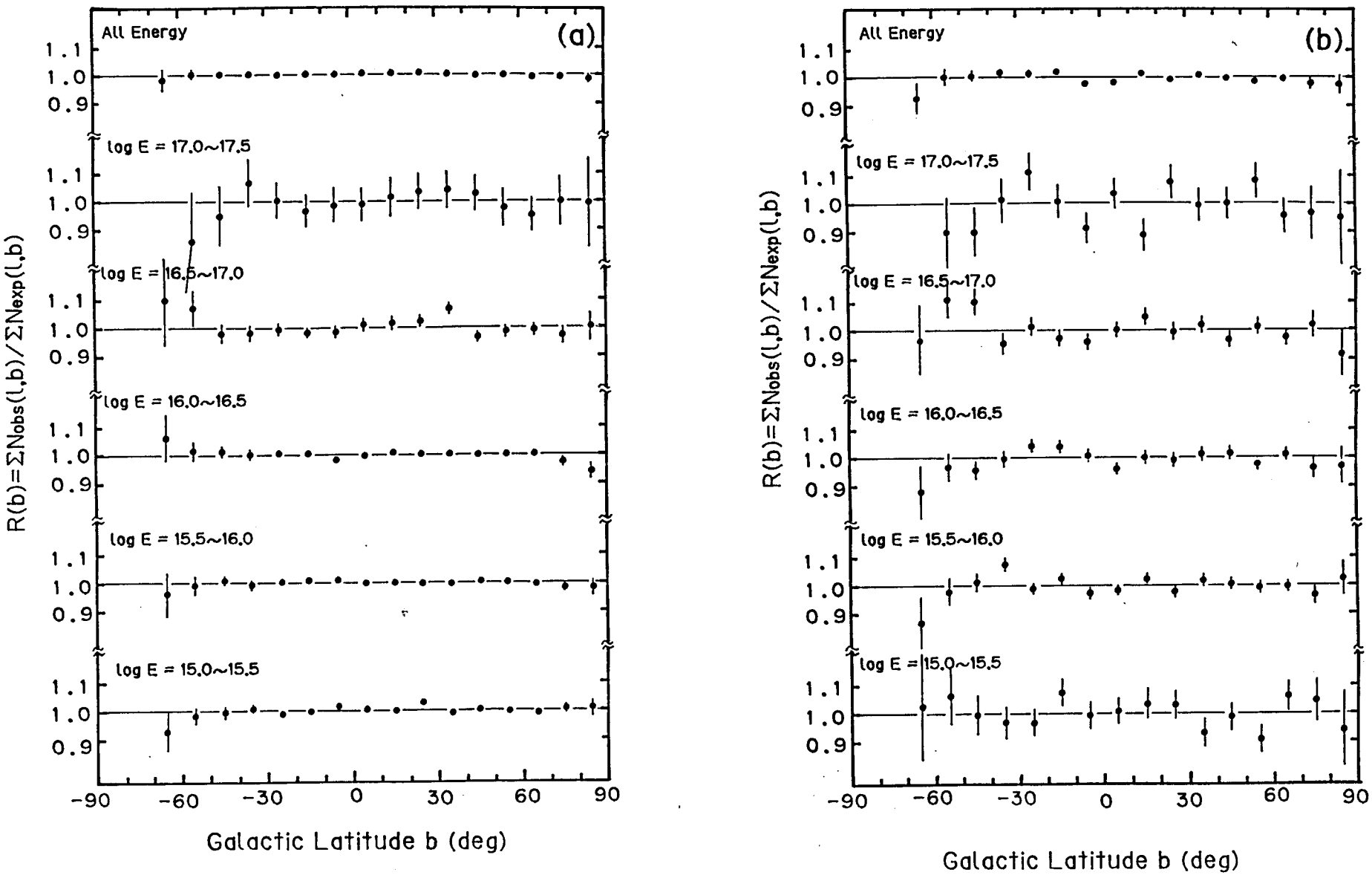
All Energy
(a)
log E = 17.0~17.5
log E = 16.5~17.0
log E = 16.0~16.5
log E = 15.5~16.0
log E = 15.0~15.5
1.1
1.0
0.9
-90
-60
-30
0
30
60
90
R(b)=ΣNobs(l,b)/ΣNexp(l,b)
Galactic Latitude b (deg)
All Energy
(b)
log E = 17.0~17.5
log E = 16.5~17.0
log E = 16.0~16.5
log E = 15.5~16.0
log E = 15.0~15.5
R(b)=ΣNobs(l,b)/ΣNexp(l,b)
Galactic Latitude b (deg)

Fig. 34

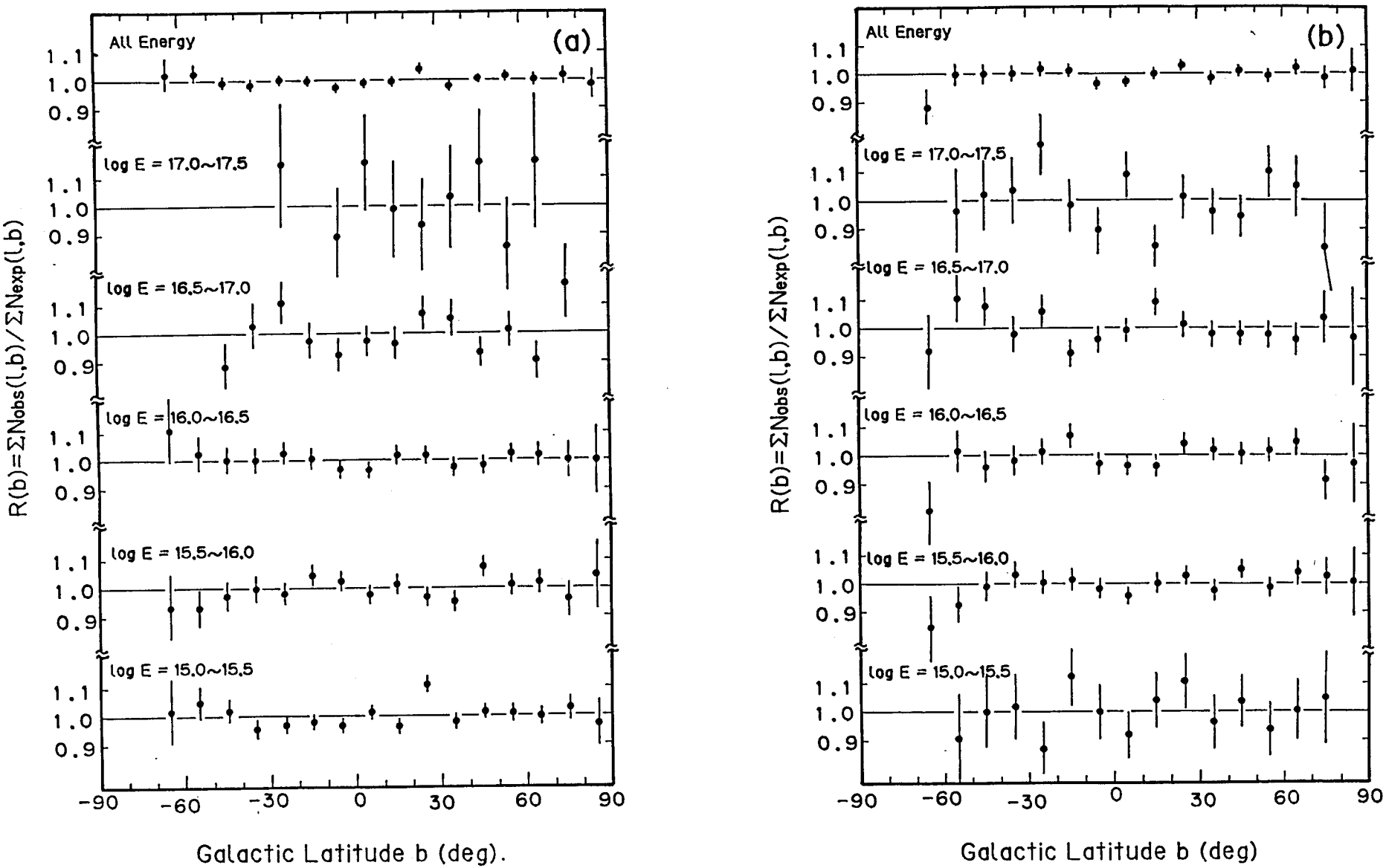
All Energy
(a)
log E = 17.0~17.5
log E = 16.5~17.0
log E = 16.0~16.5
log E = 15.5~16.0
log E = 15.0~15.5
1.1
1.0
0.9
-90
-60
-30
0
30
60
90
R(b)=ΣNobs(l,b)/ΣNexp(l,b)
Galactic Latitude b (deg).
All Energy
(b)
log E = 17.0~17.5
log E = 16.5~17.0
log E = 16.0~16.5
log E = 15.5~16.0
log E = 15.0~15.5
R(b)=ΣNobs(l,b)/ΣNexp(l,b)
Galactic Latitude b (deg)

Fig. 35

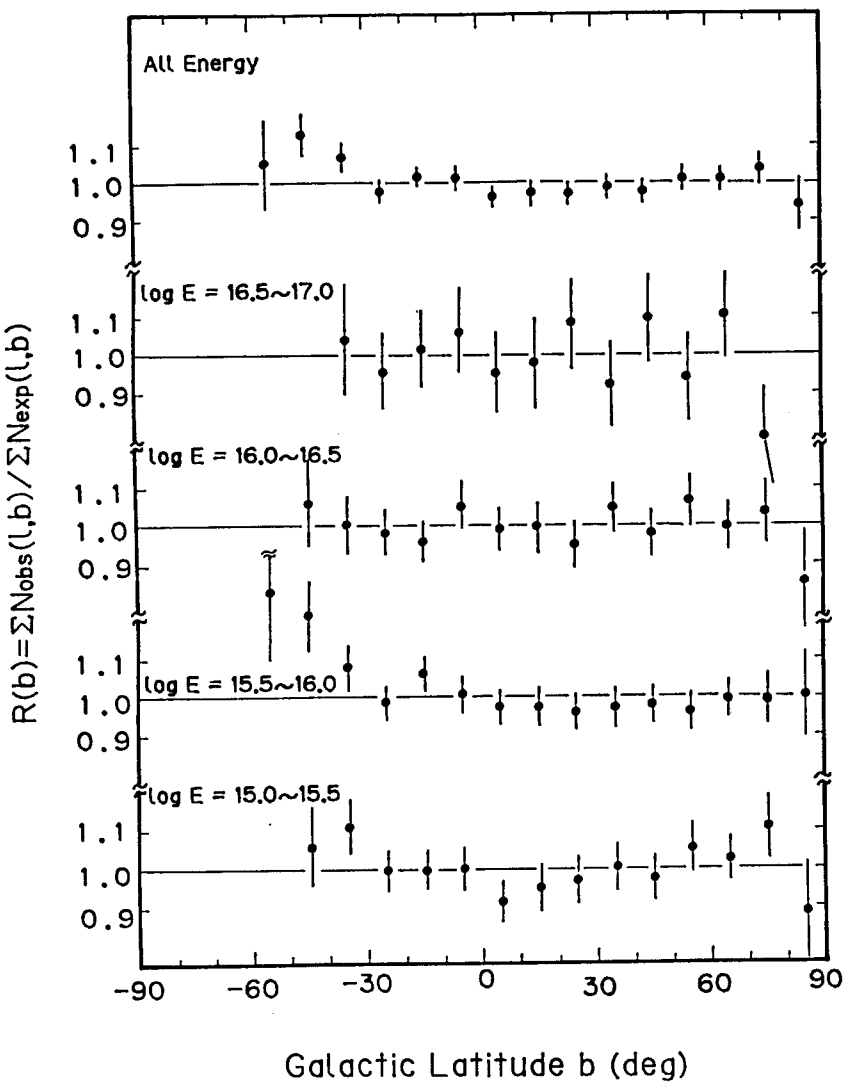
All Energy
log E = 16.5~17.0
log E = 16.0~16.5
log E = 15.5~16.0
log E = 15.0~15.5
1.1
1.0
0.9
-90
-60
-30
0
30
60
90
R(b)=ΣNobs(l,b)/ΣNexp(l,b)
Galactic Latitude b (deg)

Fig. 36

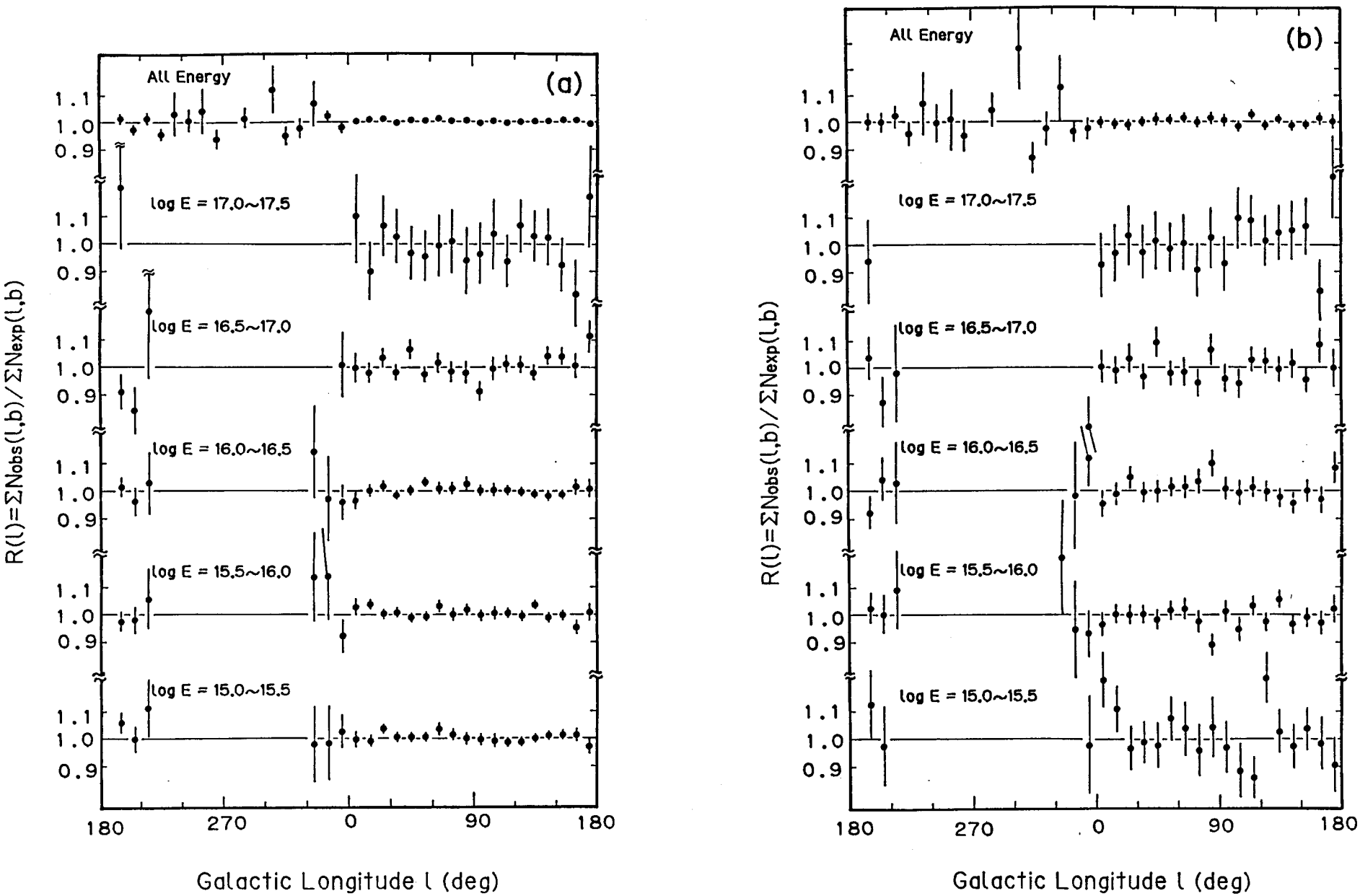
All Energy
(a)
log E = 17.0~17.5
log E = 16.5~17.0
log E = 16.0~16.5
log E = 15.5~16.0
log E = 15.0~15.5
1.1
1.0
0.9
180
270
0
90
180
Galactic Longitude l (deg)
R(l)=ΣNobs(l,b)/ΣNexp(l,b)
All Energy
(b)
log E = 17.0~17.5
log E = 16.5~17.0
log E = 16.0~16.5
log E = 15.5~16.0
log E = 15.0~15.5
Galactic Longitude l (deg)

Fig. 37

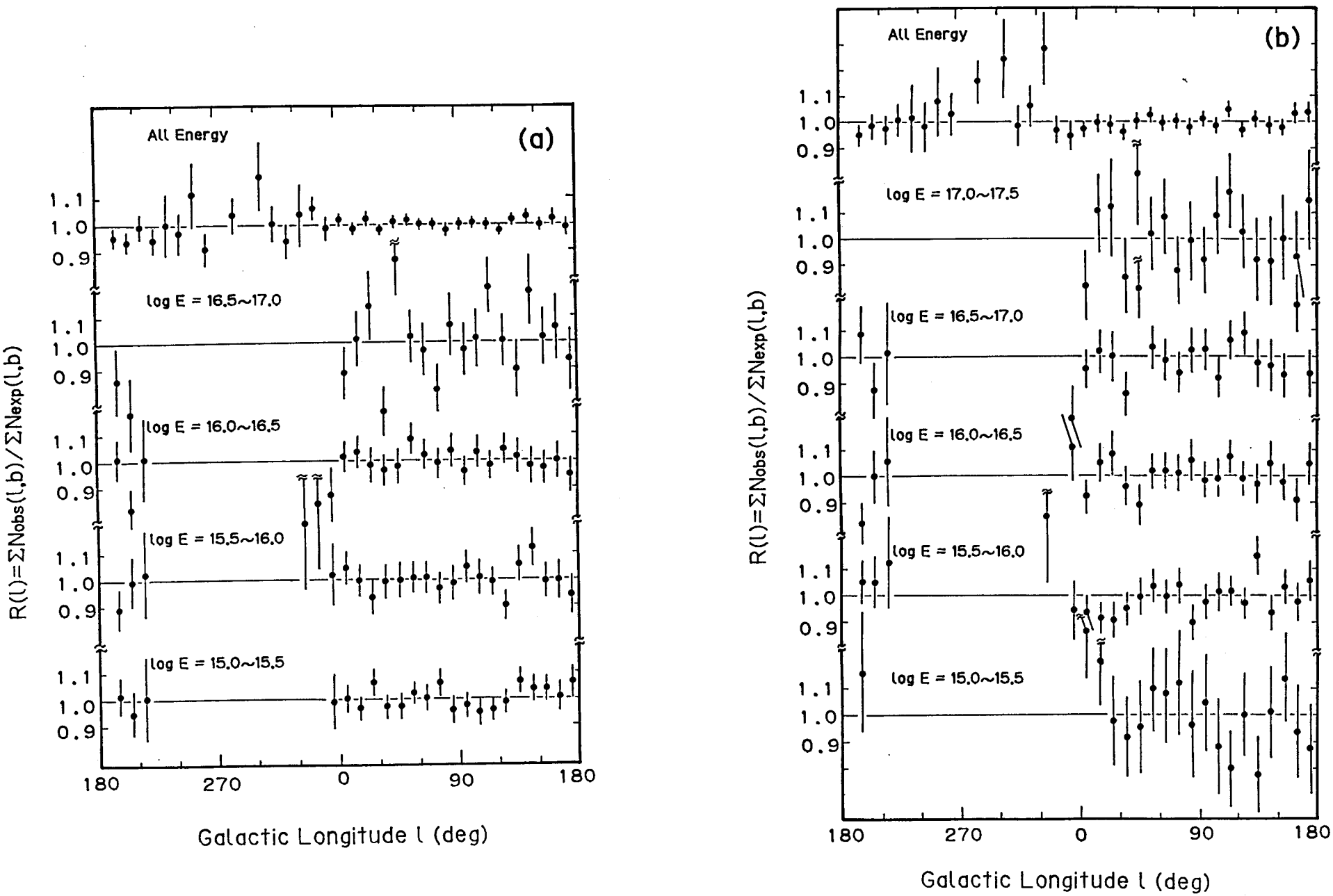
All Energy
(a)
log E = 16.5~17.0
log E = 16.0~16.5
log E = 15.5~16.0
log E = 15.0~15.5
1.1
1.0
0.9
180
270
0
90
180
Galactic Longitude l (deg)
R(l)=ΣNobs(l,b)/ΣNexp(l,b)
All Energy
(b)
log E = 17.0~17.5
log E = 16.5~17.0
log E = 16.0~16.5
log E = 15.5~16.0
log E = 15.0~15.5
Galactic Longitude l (deg)

Fig. 38

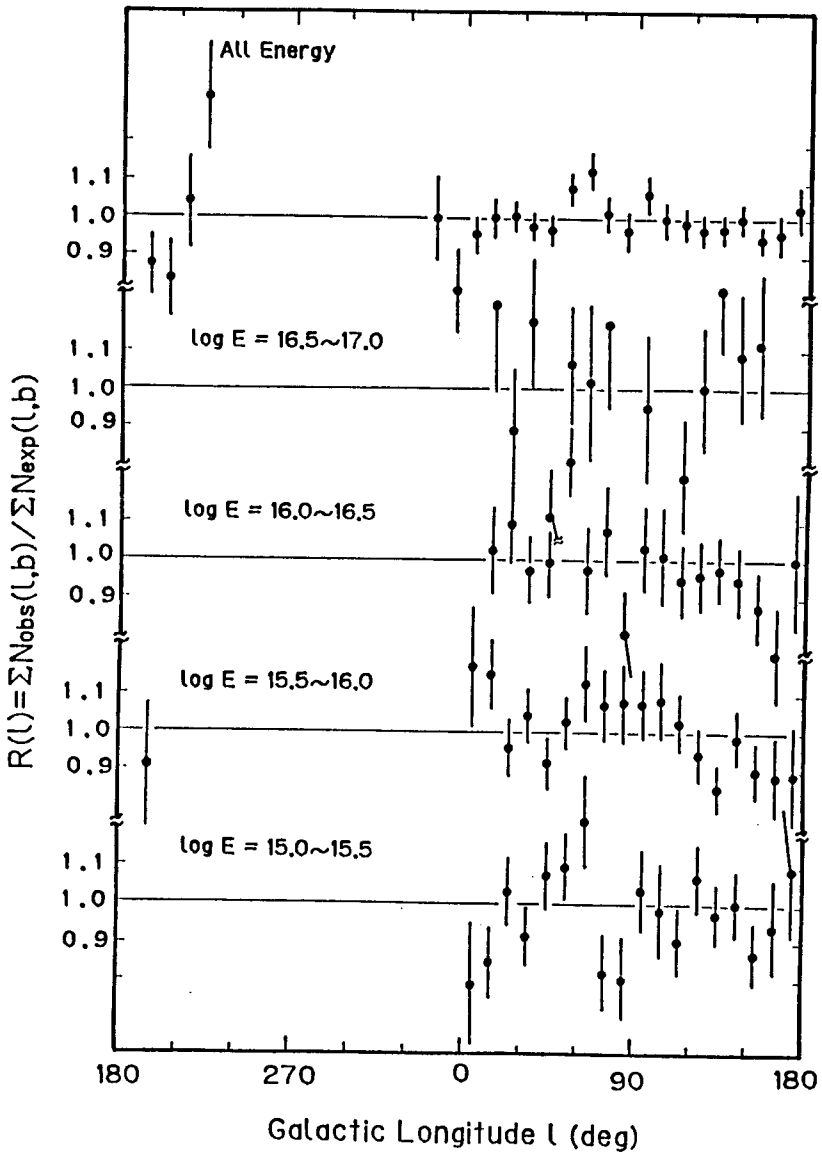
All Energy
log E = 16.5~17.0
log E = 16.0~16.5
log E = 15.5~16.0
log E = 15.0~15.5
1.1
1.0
0.9
R(l)=ΣNobs(l,b)/ΣNexp(l,b)
180
270
0
90
180
Galactic Longitude l (deg)

Fig. 39

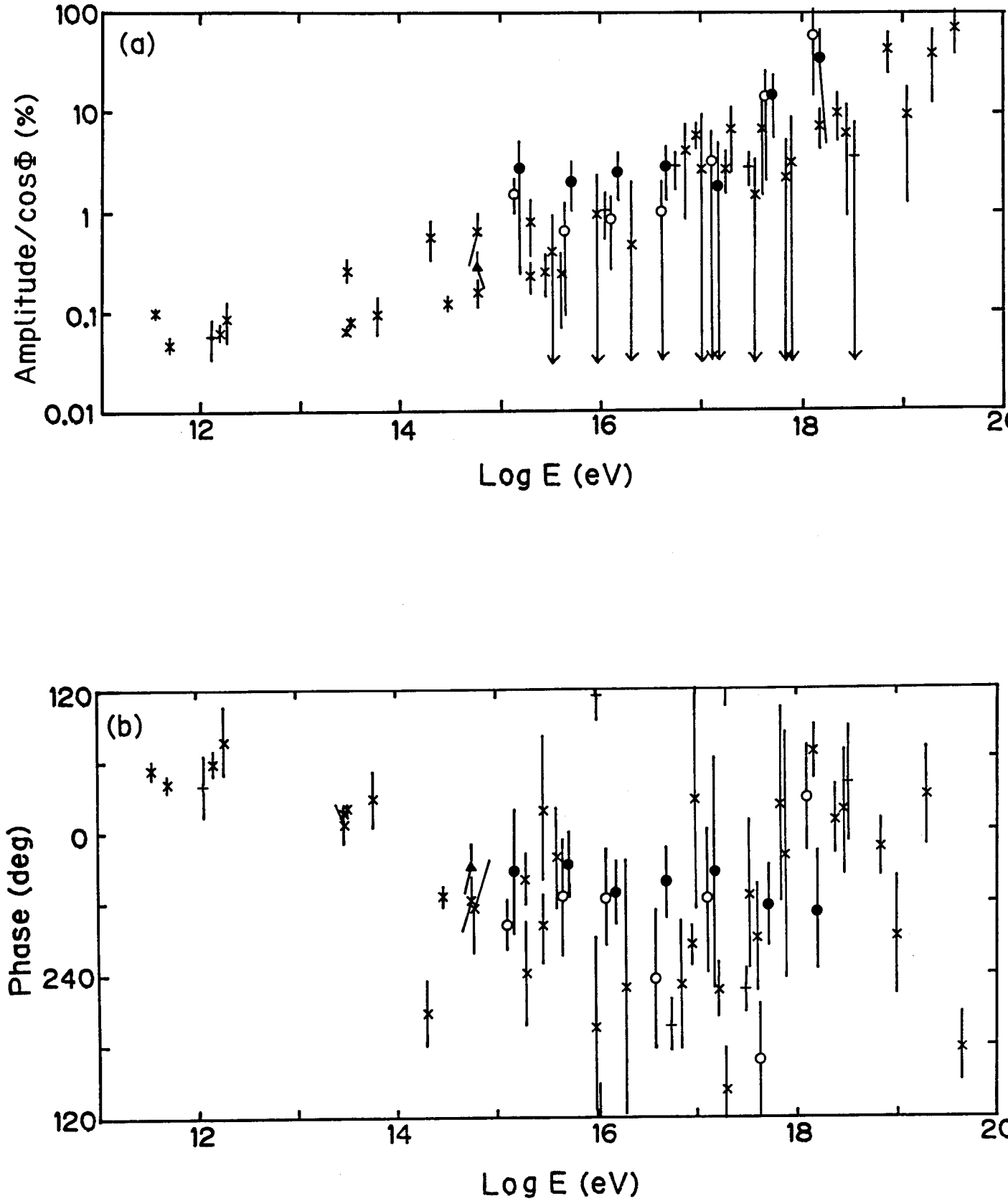
(a)
100
10
1
0.1
0.01
Amplitude/cosΦ (%)
12
14
16
18
20
Log E (eV)
(b)
120
0
240
120
Phase (deg)
12
14
16
18
20
Log E (eV)

Fig. 40

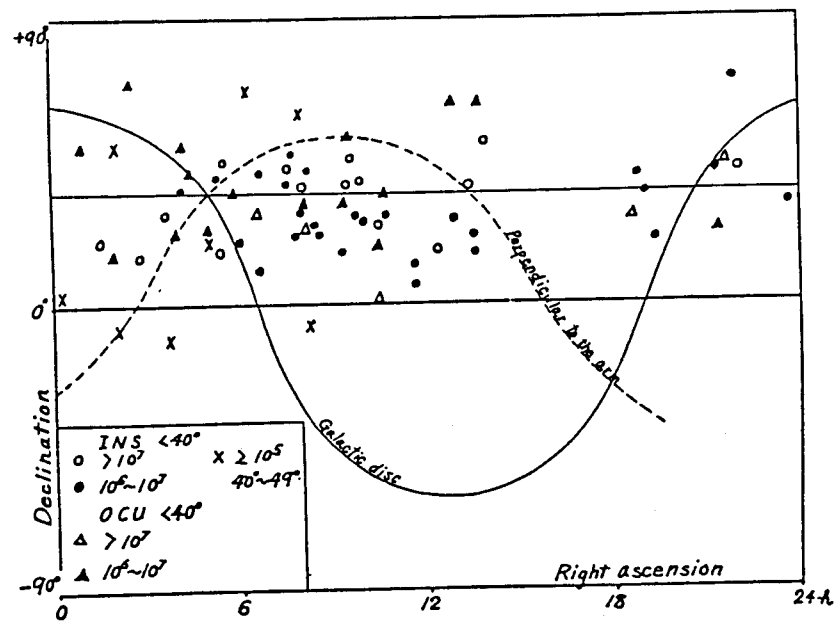
+90°
0°
-90°
Declination
INS
○ >10⁷
● 10⁶~10⁷
OCU <40°
△ >10⁷
▲ 10⁶~10⁷
× ≥10⁵ 40°~49°
Perpendicular to the earth
Galactic disc
Right ascension
0
6
12
18
24h

Fig. 42

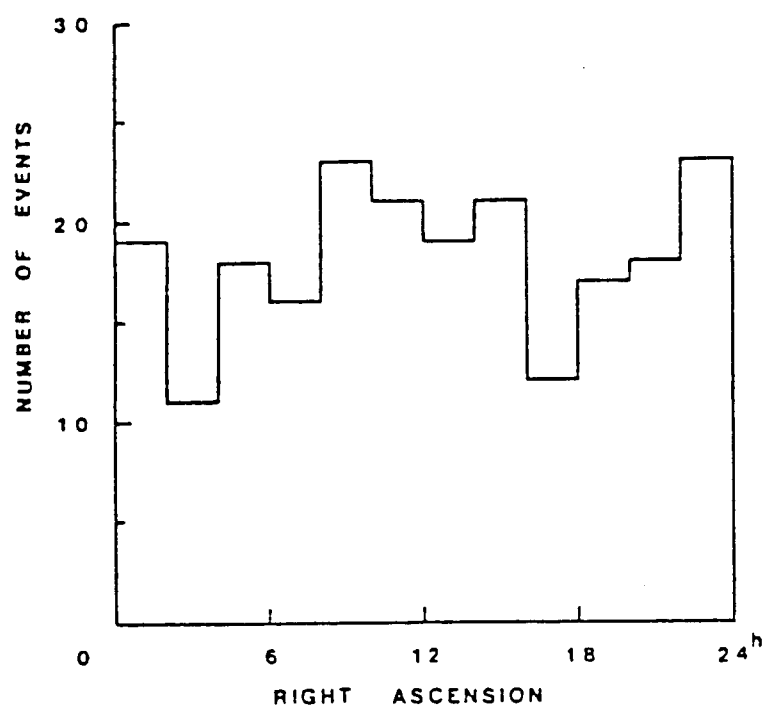
30
20
10
NUMBER OF EVENTS
0
6
12
18
24h
RIGHT ASCENSION

Fig. 43

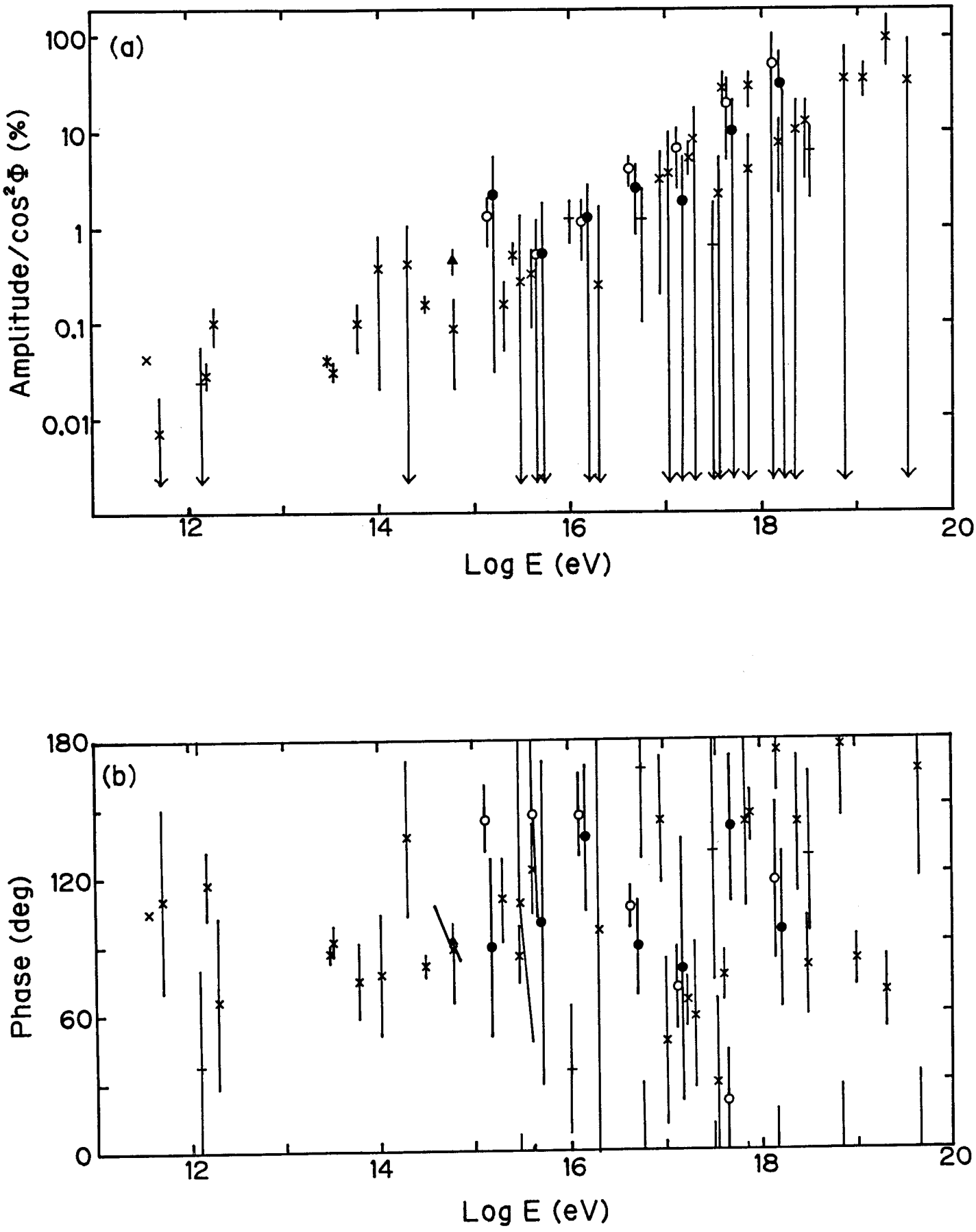
(a)
100
10
1
0.1
0.01
Amplitude/cos²Φ (%)
12
14
16
18
20
Log E (eV)
(b)
180
120
60
0
Phase (deg)
12
14
16
18
20
Log E (eV)

Fig. 41

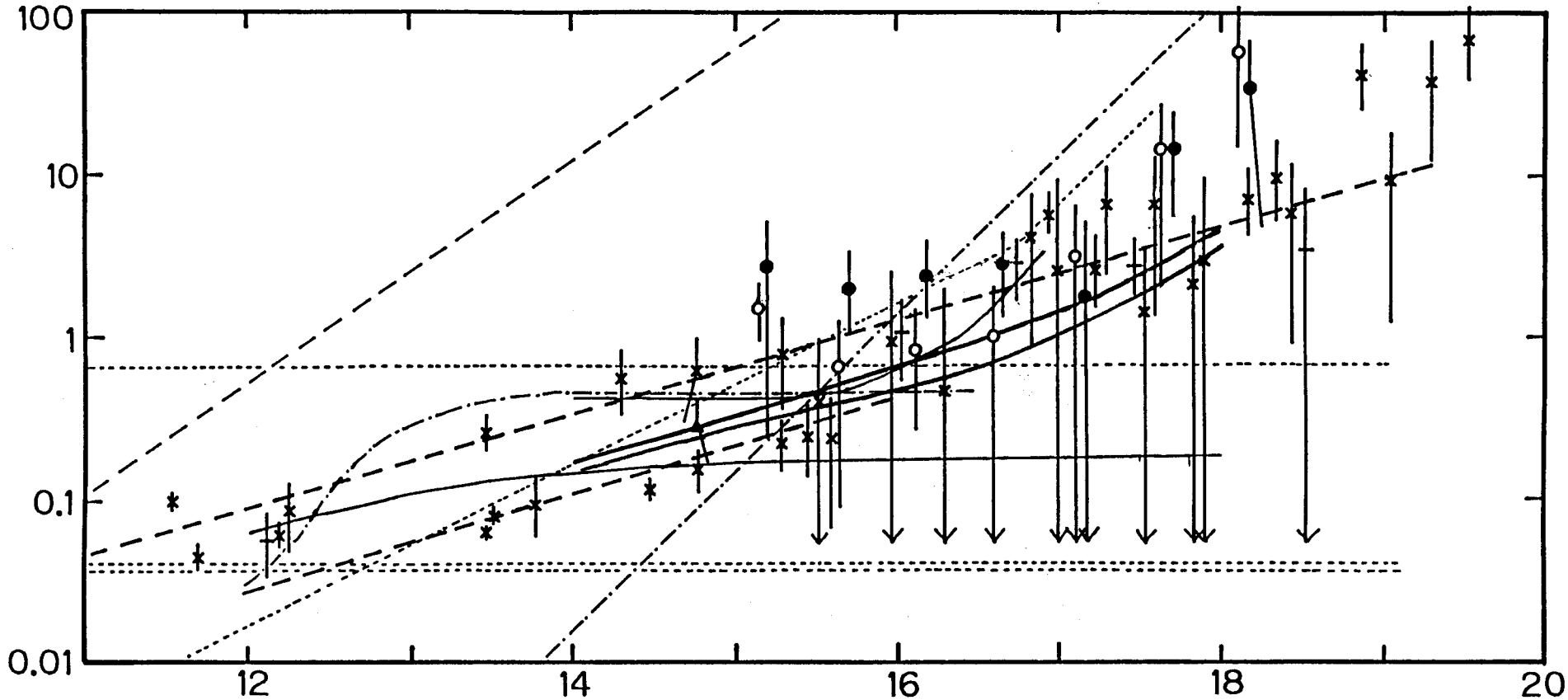

Fig. 44

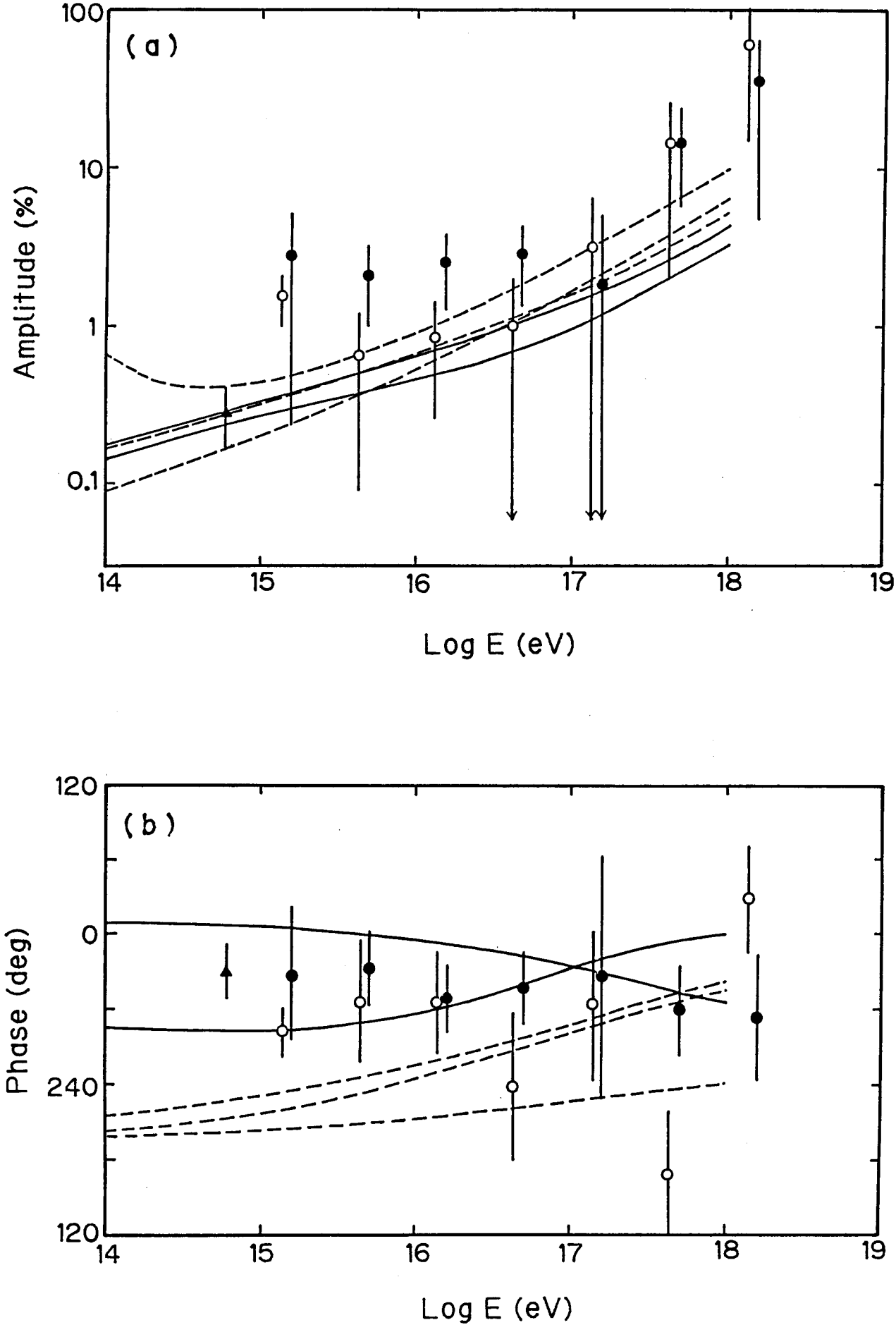
(a)
100
10
1
0.1
Amplitude (%)
14
15
16
17
18
19
Log E (eV)
(b)
120
0
240
120
Phase (deg)
14
15
16
17
18
19
Log E (eV)

Fig. 45

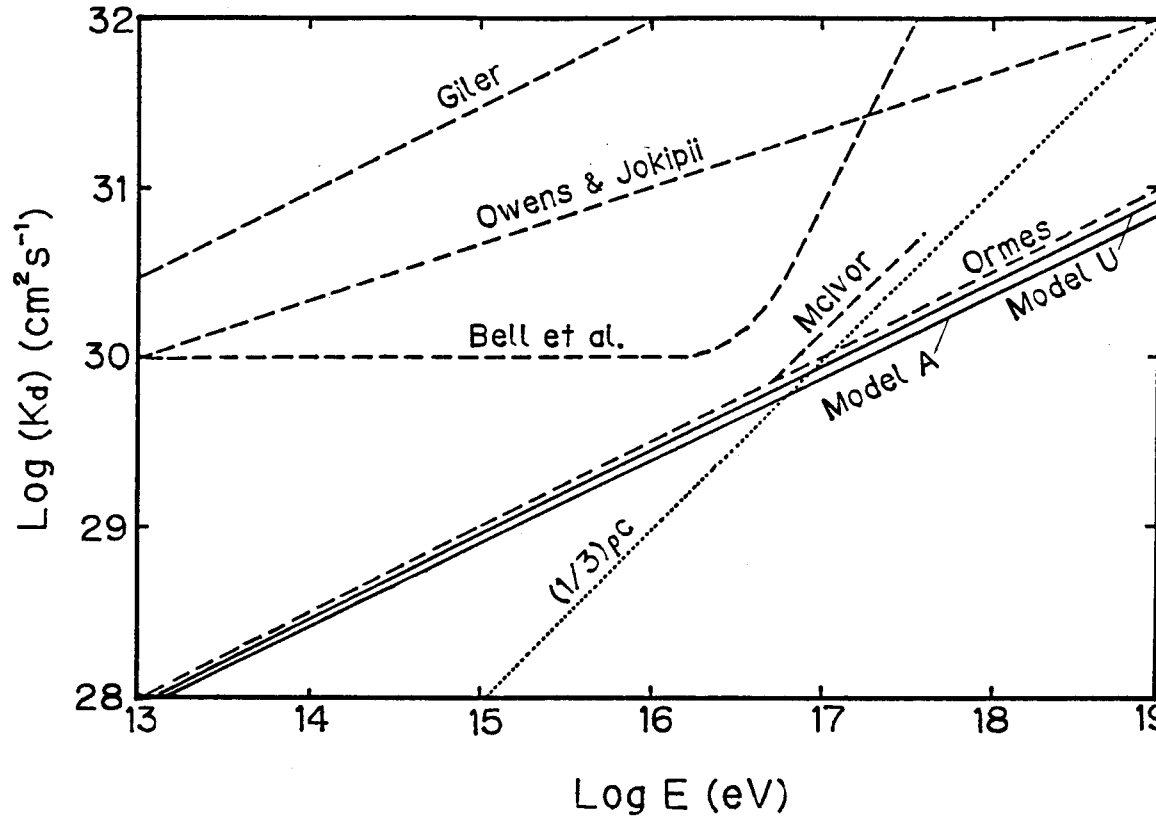
Giler
Owens & Jokipii
Bell et al.
McIvor
Ormes
Model U
Model A
(1/3)pc
Log (Kd) (cm²s⁻¹)
Log E (eV)
32
31
30
29
28
13
14
15
16
17
18
19

Fig. 46

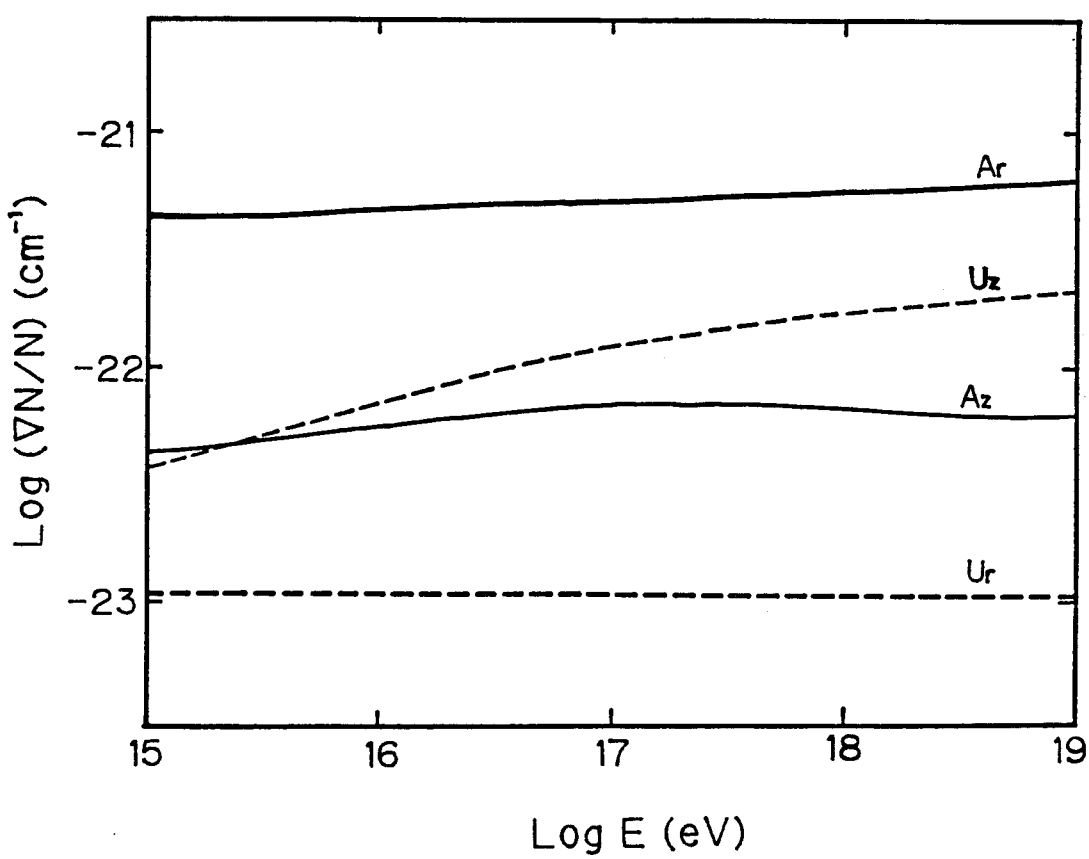
Ar
Uz
Az
Ur
Log (∇N/N) (cm⁻¹)
Log E (eV)
-21
-22
-23
15
16
17
18
19

Fig. 47

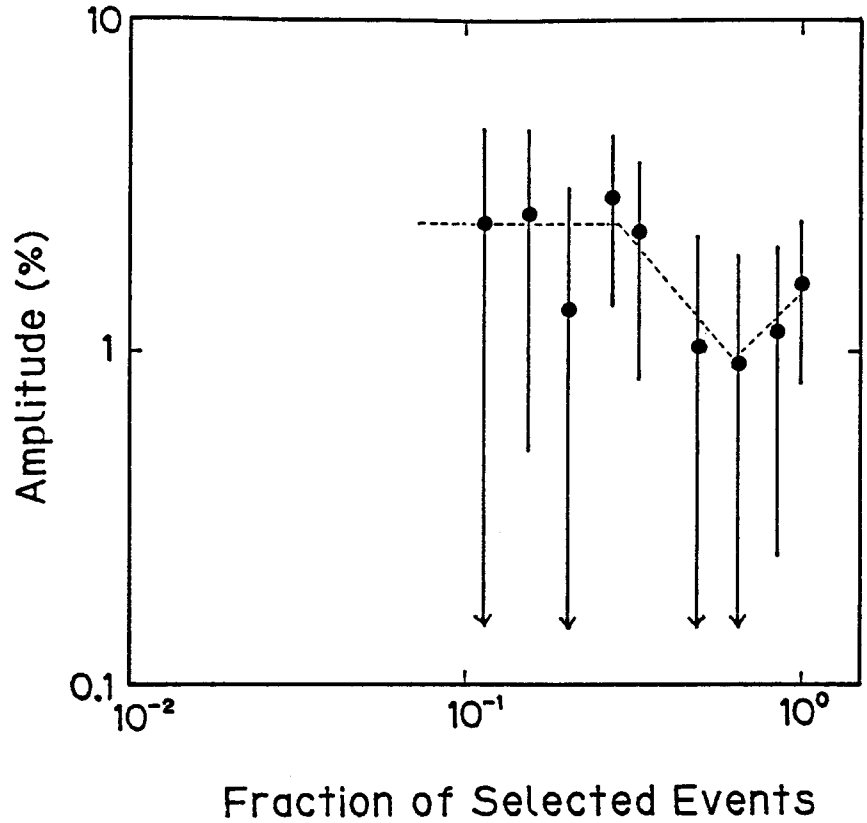
10
1
0.1
Amplitude (%)
10^{-2}
10^{-1}
10^{0}
Fraction of Selected Events

Fig. 48

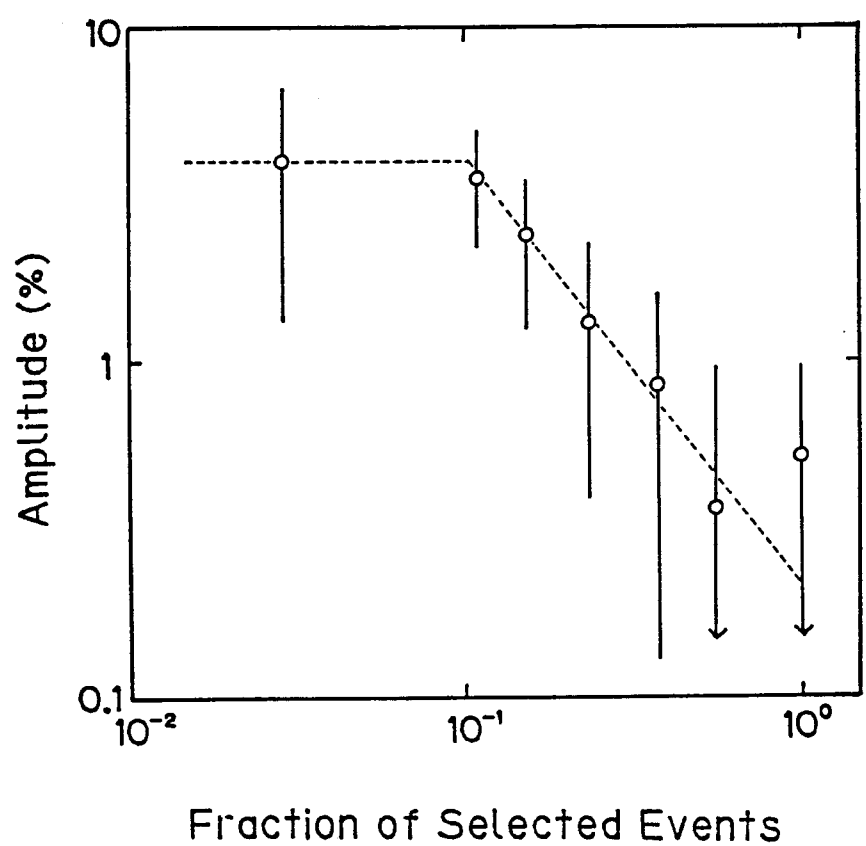
10
1
0.1
Amplitude (%)
10^{-2}
10^{-1}
10^{0}
Fraction of Selected Events

Fig. 49

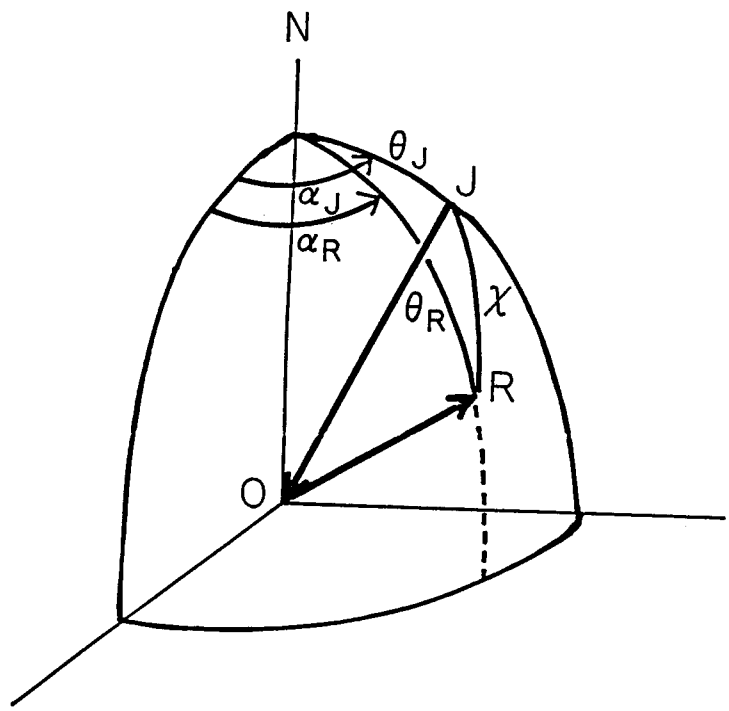

Fig. 50

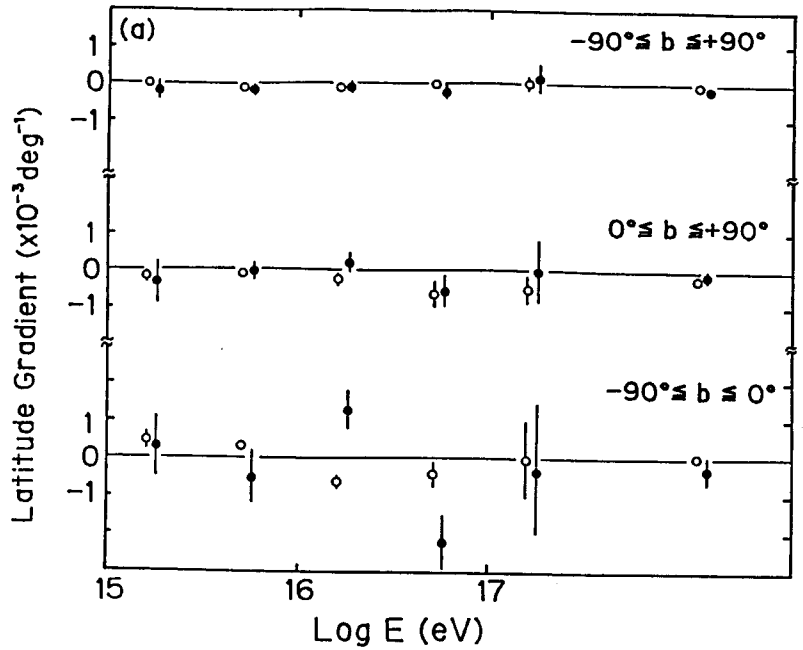
(a)
−90°≤ b ≤+90°
0°≤ b ≤+90°
−90°≤ b ≤ 0°
Latitude Gradient (x10⁻³deg⁻¹)
Log E (eV)

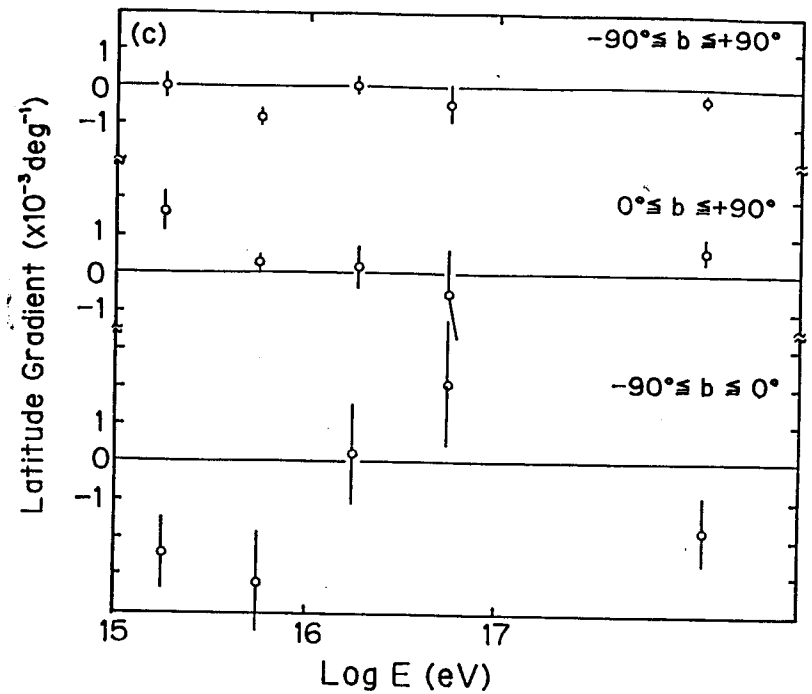
(c)
−90°≤ b ≤+90°
0°≤ b ≤+90°
−90°≤ b ≤ 0°
Latitude Gradient (x10⁻³deg⁻¹)
Log E (eV)

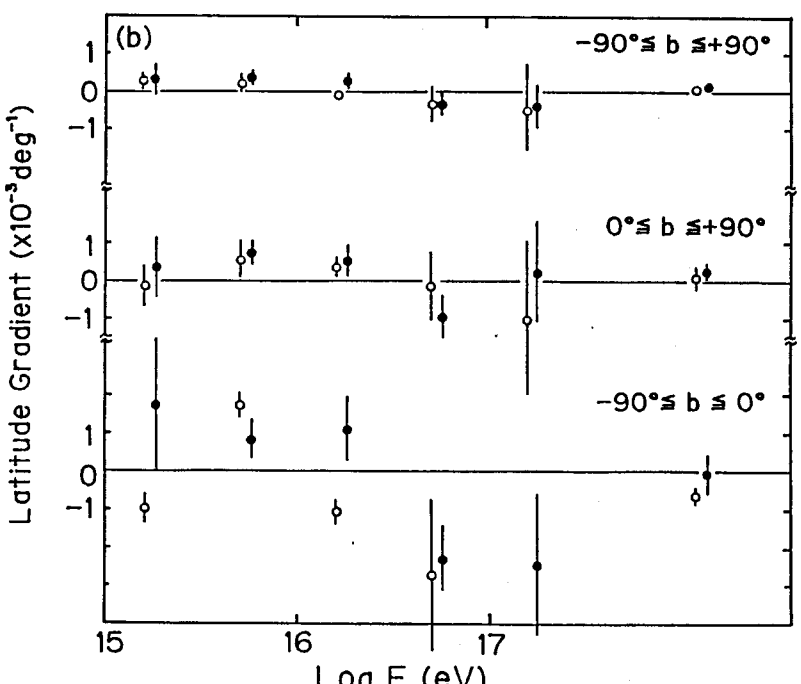
(b)
−90°≤ b ≤+90°
0°≤ b ≤+90°
−90°≤ b ≤ 0°
Latitude Gradient (x10⁻³deg⁻¹)
Log E (eV)

Fig. 51

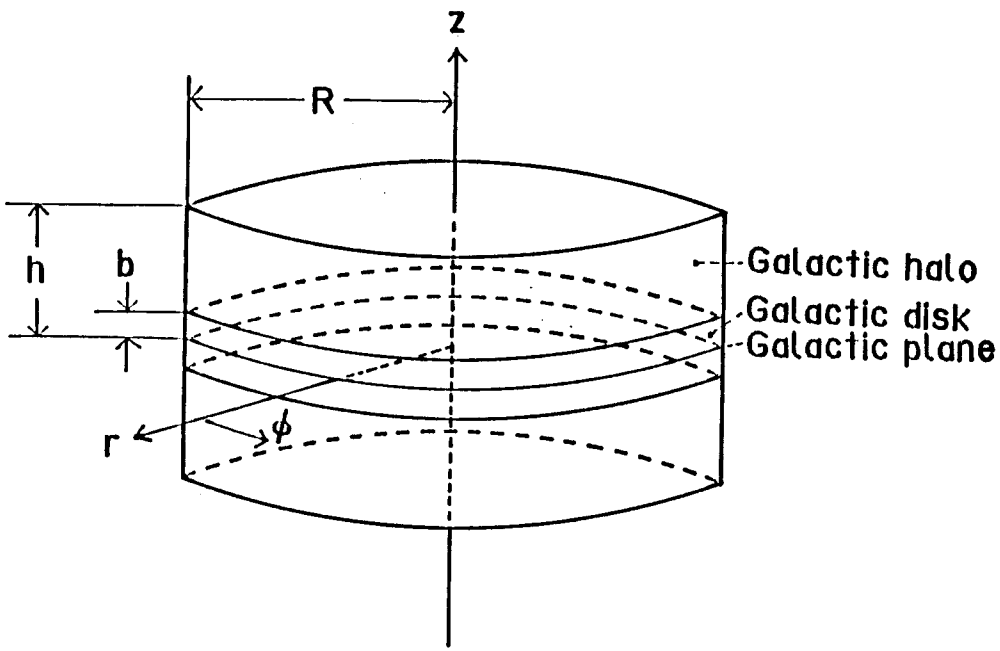
z
R
h
b
Galactic halo
Galactic disk
Galactic plane
r
ϕ

Fig. 52

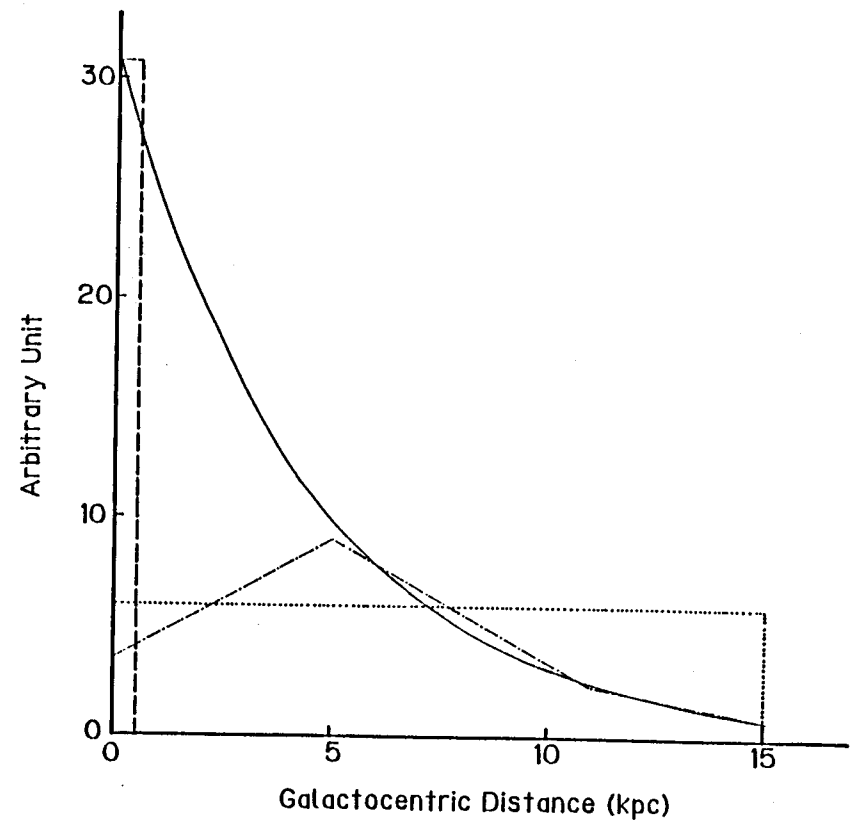
30
20
10
0
Arbitrary Unit
0
5
10
15
Galactocentric Distance (kpc)

Fig. 53